Dissertations, Theses, and Masters Projects   Theses, Dissertations, & Master Projects

Summer 2016

Rhythmogenic and Premotor Functions of Dbx1 Interneurons in the Pre-Bötzinger Complex and Reticular Formation: Modeling and Simulation Studies

Hanbing Song
College of William and Mary - Arts & Sciences, hsong03@email.wm.edu

Recommended Citation

Rhythmogenic and Premotor Functions of Dbx1 Interneurons in the pre-Bötzinger
Complex and Reticular Formation: Modeling and Simulation Studies

Hanbing Song

Tianjin, China

Master of Science, Florida State University, 2012
Bachelor or Science, Nankai University, 2010

A Dissertation presented to the Graduate Faculty
of the College of William and Mary in Candidacy for the Degree of
Doctor of Philosophy

Department of Applied Science

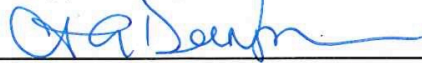The College of William and Mary
January 2017

APPROVAL PAGE

This Dissertation is submitted in partial fulfillment of
the requirements for the degree of

Doctor of Philosophy
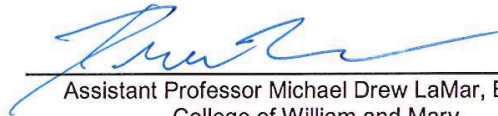
_____
Hanbing Song

Approved by the Committee, August, 2016
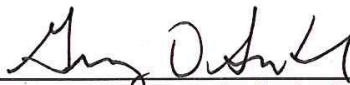
_____
Committee Chair
Professor Christopher A. Del Negro, Applied Science
College of William and Mary

_____
Assistant Professor Michael Drew LaMar, Biology
College of William and Mary

_____
Professor Gregory D. Smith, Applied Science
College of William and Mary

_____
Associate Professor Leah B. Shaw, Applied Science
College of William and Mary

_____
Assistant Professor Kaiwen Kam, Cell Biology and Anatomy
Chicago Medical School, Rosalind Franklin University

ABSTRACT

Breathing in mammals depends on rhythms that originate from the preBötzinger complex (preBötC) of the ventral medulla and a network of brainstem and spinal premotor neurons. The rhythm-generating core of the preBötC, as well as some premotor circuits, consists of interneurons derived from Dbx1-expressing precursors but the structure and function of these networks remain incompletely understood. We previously developed a cell-specific detection and laser ablation system to interrogate respiratory network structure and function in a slice model of breathing that retains the preBötC, premotor circuits, and the respiratory related hypoglossal (XII) motor nucleus such that in spontaneously rhythmic slices, cumulative ablation of Dbx1 preBötC neurons decreased XII motor output by half after only a few cell deletions, and then decelerated and terminated rhythmic function altogether as the tally increased. In contrast, cumulatively deleting Dbx1 premotor neurons decreased XII motor output monotonically, but did not affect frequency nor stop functionality regardless of the ablation tally. This dissertation presents several network modeling and cellular modeling studies that would further our understanding of how respiratory rhythm is generated and transmitted to the XII motor nucleus. First, we propose that cumulative deletions of Dbx1 preBötC neurons preclude rhythm by diminishing the amount of excitatory inward current or disturbing the process of recurrent excitation rather than structurally breaking down the topological network. Second, we establish a feasible configuration for neural circuits including an Erdős-Rényi preBötC network and a small-world reticular premotor network with interconnections following an anti-preferential attachment rule, which is the only configuration that produces consistent outcomes with previous experimental benchmarks. Last but not least, since the performance of neuronal network simulations is, to some extent, affected by the nature of the cellular model, we aim to develop a more realistic cellular model based on the one we adopted in previous network studies, which would account for recent experimental findings on rhythmogenic preBötC neurons.

TABLE OF CONTENTS

ACKNOWLEDGEMENTS

This Ph.D. thesis is dedicated to my family who helped me countless times along the way, and Mr. Jinkai AN, my middle school math teacher who taught me that a rigorous attitude in math is a more valuable quality than talent…

CHAPTER 1. Mechanisms leading to rhythm cessation in the respiratory preBötzinger complex due to piecewise cumulative neuronal deletions

1.1 INTRODUCTION

Inspiratory breathing movements originate within the preBötzinger complex (preBötC) of the lower medulla (Smith et al., 1991; Feldman and Del Negro, 2006; Feldman et al., 2013; Moore et al., 2013). The underlying mechanisms that generate inspiratory rhythm and their susceptibility to failure in conditions of deterioration or disease remain incompletely understood. Here we address these interrelated issues using modeling and simulation.

Interneurons whose progenitors express the homeodomain transcription factor Dbx1 (i.e., Dbx1 neurons) are glutamatergic and form local and commissural excitatory synaptic connections. These neurons may comprise the excitatory rhythmogenic core of the preBötC according to the Dbx1 core hypothesis (Bouvier et al., 2010; Gray et al., 2010; Picardo et al., 2013), which predicts that cumulative destruction of Dbx1 neurons in the preBötC should irreversibly impair and then prohibit respiratory rhythm by degrading the core oscillator. This prediction was experimentally tested by photonically destroying Dbx1 preBötC neurons in rhythmically active slices that retain the preBötC, while monitoring breathing-related motor output from the hypoglossal (XII) cranial nerve. Inspiratory motor output decreased in amplitude and frequency until the spontaneous rhythm irreversibly terminated after ~15% of the Dbx1 preBötC population was destroyed (Wang et al., 2014).

These data support the Dbx1 core hypothesis but cannot explain the cessation of network rhythm, which could have structural or dynamical explanations. First, loss of rhythm could coincide with a precipitous drop in network connectivity (i.e., structure), which impairs neuronal communication and thus precludes coordinated activity. Second, removing constituent neurons could decrease excitability or lower baseline membrane potential of the neurons that remain and thus impede burst generation. It is also possible that cumulative cellular ablations cause structural and dynamical changes whose combined effects halt rhythmic activity.

Inspiratory neural bursts in the preBötC depend on excitatory synaptic transmission (Greer et al., 1991; Funk et al., 1993; Ge and Feldman, 1998; Rekling et al., 2000; Wallén-Mackenzie et al., 2006). According to the logic of a canonical network oscillator (Grillner, 2006) recurrent excitation spreads from active presynaptic neurons to quiescent postsynaptic partners, which causes temporal summation and recruitment to the active burst phase (Rubin et al., 2009). Cumulatively ablating ~39 neurons in the model preBötC (330 neurons in total) stops spontaneous rhythmic function. Here we show that this loss of function is not linked solely to deterioration of network structure as determined by a subset of formal network measures, but by the combined effect of loss of network structure and neuronal dynamics. Selectively targeting neurons that have a large number of incoming synapses decreases the ablation tally considerably, emphasizing the importance of these synaptic properties for spontaneous rhythmic function. We conclude that rhythm cessation is attributable

to the loss of constituent neurons with large numbers of incoming synapses or high excitability (or both), which impedes recurrent excitation by diminishing the rate at which synaptic transmission among network constituents recruits more neurons to join the active phase. Failing to reach a threshold rate of 1 neuron/ms, recurrent excitation cannot spread quickly enough to recruit the entire network; subsequent spontaneous bursts no longer occur. This study is important for understanding basic mechanisms of rhythm generation and potentially for restoring functionality to arrhythmic networks in pathological conditions and disease.

1.2 MATERIALS AND METHODS

1.2.1 Rubin-Hayes preBötC interneuron model

Each node (i.e., neuron) is populated with a Rubin-Hayes preBötC model (Rubin et al., 2009; Dunmyre et al., 2011), which features Hodgkin-Huxley-like spiking currents and four additional currents: calcium-activated non-specific cation current (I_{CAN}) (Crowder et al., 2007; Pace et al., 2007a; Mironov, 2008, 2013; Pace and Del Negro, 2008; Mironov and Skorova, 2011), persistent sodium current (I_{NaP}) (Del Negro et al., 2002a; Ptak et al., 2005; Koizumi and Smith, 2008), excitatory synaptic current mediated predominantly by AMPA receptors (I_{syn}) (Funk et al., 1993; Ge and Feldman, 1998; Wallén-Mackenzie et al., 2006), and electrogenic Na/K ATPase pump current (I_{pump}) (Del Negro et al., 2009; Krey et al., 2010). The model features material balance equations for intracellular calcium and sodium concentrations. The Rubin-Hayes model is in the public domain (http://senselab.med.yale.edu/modeldb/ShowModel.asp?model=125649).

The current-balance equation takes the form:

$$C\frac{dV}{dt} = -I_{\text{leak}}(V) - I_{\text{Na}}(V,m,h) - I_{\text{k}}(V,n) - I_{\text{CAN}}(V,Ca) - I_{\text{Na-P}}(V,h_{\text{Na-P}})$$

$$- I_{\text{syn}}(V,s_1 \ldots s_N) - I_{\text{pump}}(Na)$$

where

$$\frac{dx}{dt} = (x_\infty(V) - x)/T_x(V)$$

$$\frac{ds}{dt} = ((1-s)s_\infty(V) - k_s s)/T_s$$

$$\frac{dCa}{dt} = \varepsilon\left(\sum_{i=1}^{N} s_i \cdot k_{\text{synCa}} - k_{\text{Ca}}(Ca - Ca_\infty)\right)$$

$$\frac{dNa}{dt} = \alpha(-I_{\text{CAN}}(V,Ca) - I_{\text{pump}}(Na))$$

describe the evolution of the state variables, for each $x \in \{m,h,n,h_{\text{Na-P}}\}$.

Membrane currents are described with chord-conductance equations, in some cases modified for Ca2+ or Na+ gating (I_{CAN} and I_{pump}) (Li et al., 1996):

$$I_{\text{leak}}(V) = g_{\text{leak}}(V - E_L)$$

$$I_{\text{Na}}(V,m,h) = g_{\text{Na}}m^3 h(V - E_{\text{Na}})$$

$$I_{\text{Na-P}}(V,h_{\text{Na-P}}) = g_{\text{Na-P}}m_{\text{Na-P}_\infty}h_{\text{Na-P}}(V - E_{\text{Na}})$$

$$I_K(V,n) = g_K n^4 (V - E_K)$$

$$I_{\text{CAN}}(V,Ca) = g_{\text{CAN}}(V - E_{\text{CAN}})/(1 + \exp((Ca - k_{\text{CAN}})/\sigma_{\text{CAN}}))$$

$$I_{\text{syn}}(V,s_1 \ldots s_N) = g_{\text{syn}}\sum_{i=1}^{N} s_i(V - E_{\text{syn}})$$

where N is the number of presynaptic neurons and $\{s_1 \ldots s_N\}$ is the set of presynaptic gating variables s, and $I_{\text{pump}}(Na) = r_{\text{pump}}(\phi(Na) - \phi(Na_\infty))$.

The remaining functions in the model, including those representing the voltage-dependence of channel kinetics, are:

$$x_\infty(V) = 1 \Big/ \left(1 + \exp\left(\frac{V - \theta_x}{\sigma_x}\right)\right)$$

$$T_x(V) = T_{x\max} \Big/ \cosh\left(\frac{V - \theta_x}{2\sigma_x}\right)$$

$$\phi(Na) = Na^3 / (Na^3 + k_{Na}^3)$$

Model parameters are set to the following values, unless otherwise specified:

$C = 45\ pF, g_{leak} = 3 \pm 0.78\ nS, E_L = -61.46\ mV, g_{Na} = 150\ nS, E_{Na} = 65\ mV,$

$g_{Na-P} = 1\ nS, g_K = 30\ nS,\ E_K = -75\ mV, g_{CAN} = 4 \pm 0.75\ nS, E_{CAN} = 0\ mV,$

$\theta_m = -36\ mV, \sigma_m = -8.5\ mV, T_{m_{max}} = 1\ ms, \theta_h = -30\ mV, \sigma_h = 5\ mV,$

$\theta_n = -30\ mV, \sigma_n = -5\ mV, T_{n_{max}} = 30\ ms, \theta_s = 15\ mV, \sigma_s = -3\ mV, T_s = 15\ ms,$

$\theta_{m_{Na-P}} = -40\ mV, \sigma_{m_{Na-P}} = -6\ mV, \theta_{h_{Na-P}} = -48\ mV, \sigma_{h_{Na-P}} = 6\ mV,$

$T_{Na-P} = 1000\ ms, k_{Ca} = 22.5\ ms^{-1}, \theta_{CAN} = 0.9\ \mu M, \sigma_{CAN} = -0.05\ \mu M, k_s = 1,$

$k_{synCa} = 1200\ \mu M \cdot ms^{-1}, r_{pump} = 200\ pA, k_{Na} = 10\ mM, Ca_\infty = 0.05\ \mu M,$

$\varepsilon = 0.0007, \alpha = 6.6{\times}10^{-5}\ mM \cdot pA^{-1} \cdot ms^{-1}, g_{syn} = 3.25\ nS, E_{syn} = 0\ mV,$

$T_{h_{max}} = 15\ ms, Na_\infty = 5\ mM.$

Synaptic inputs and Calcium dynamics

Synaptically triggered increases in cytosolic Ca^{2+} directly activate I_{CAN}. We coupled the synaptic variable s to the Ca^{2+} equation. The synaptic variable s represents both ionotropic and metabotropic glutamatergic receptor (mGluR) activation. Cytosolic Ca^{2+} changes are attributable to influx through voltage-gated Ca^{2+} channels evoked by AMPA receptor-mediated depolarization as well as group I mGluRs that evoke intracellular Ca^{2+} release from stores in the

endoplasmic reticulum (Pace et al., 2007a; Pace and Del Negro, 2008). Rather than explicitly model the biophysics and intracellular signaling that elevate intracellular Ca^{2+}, we abstracted the process such that when a presynaptic neuron discharges an action potential, its corresponding synaptic gating variable *s* increments, which then raises intracellular Ca^{2+} in all the postsynaptic neurons to which it projects. The parameter kIP_3 governs how much Ca^{2+} increases per unit increment in synaptic gating variable *s*. Variable *s* also appears in the chord-conductance equation for I_{syn}, where it controls AMPA receptor gating.

Parameters

The model maintains rhythmic function over substantial variation in g_{CAN}, g_{Na-P}, k_{IP3}, g_{syn}, r_{pump}, and k_{Ca} from nominal baseline values when I_{pump} is present. Initial values for the membrane potential and gating variables were set constant. The parameters g_{CAN} and g_{leak} were randomly assigned from Gaussian distributions given the average and standard deviation listed above. Then, g_{syn} was normalized by the in-degree of each neuron so that the maximum synaptic conductance was equal in all constituent neurons.

1.2.2 Network simulations

We modeled the preBötC as a directed network because excitatory chemical synapses, rather than gap junctions, are central to its rhythmic function (Greer et al., 1991; Funk et al., 1993; Rekling et al., 2000; Wallén-Mackenzie et al., 2006). Having no empirical information about network topology, we applied a directed Erdős-Rényi random graph (Newman et al., 2001) as the underlying model of preBötC network structure.

Erdős-Rényi random networks were generated via two parameters, the network size n and connection probability p. We denote the underlying graphs as G(n,p) (Gilbert, 1959). Population size was fixed at n = 330 Dbx1 neurons (Hayes et al., 2012; Wang et al., 2014). Excitatory chemical synapses were reported in 13% of paired whole-cell patch-clamp recordings from putatively rhythm-generating preBötC neurons in mouse slices (Rekling et al., 2000), and thus we used p = 0.125.

We simulated the network models on a computer cluster that features 193 nodes with a total of 943 CPU (central processing unit) cores, 5.9 terabytes of physical memory, 220 terabytes of disk capacity, and peak performance of 21.2 teraflops. We used a Runge-Kutta fourth-order numerical integration routine with fixed time step of 0.25 ms. Network models were subjected to 100 random deletions because a tally of less than 100 Dbx1 neuron laser ablations was experimentally demonstrated to silence spontaneous respiratory rhythm in an experimental slice model of breathing (Wang et al., 2014). For simulations, one neuron was deleted every 25 sec (simulated time). Neuron deletions were achieved by setting the synaptic state variable and its corresponding differential equation to zero, thereby disconnecting the cell from the remaining network.

A running time spike histogram provided a convenient measure of ensemble network activity, akin to the experimental recording of respiratory-related hypoglossal nerve (XII) root discharge in vitro (Smith et al., 1991; Funk and Greer, 2013). The histogram counted the number of spikes per 10-ms bin, where

bins were contiguous for the duration of the simulation. Neurons no longer contributed to the running time spike histogram after ablation.

Transient glutamatergic stimulation of constituent model neurons mimicked a holographic glutamate un-caging protocol applied to preBötC neurons (Kam et al., 2013a). Focal stimulation was achieved by setting the synaptic state variable to 0.6 for 200 ms, without modifying the differential equation, leading to an exponential relaxation of glutamatergic excitation.

1.2.3 Static network (topological) analysis

The connectivity of a network is reported by the entries in its adjacency matrix A, where $A_{ij} = 1$ if and only if there is a directed link (synaptic connection) from neuron i to neuron j; otherwise, $A_{ij} = 0$. In discrete simulations that examine only the topological structure of the underlying graph G(n,p), without considering the dynamics of nodes and links (i.e., neurons and synapses), ablations were modeled by removing nodes from the network along with their links. We computed three global metrics (K-core, number of strongly connected components, as well as the average in/out degree) at the initial state of the network and for its corresponding state after each one of a sequence of 100 random deletions were performed. Also, for each deleted node, we computed four local metrics (local cluster coefficient, closeness centrality, betweenness centrality, and communicability centrality) to indicate the importance of the node that was (in each case) removed from the network.

Local cluster coefficient

Local cluster coefficients measure how close the neighbors of the node are to being a complete directed graph, i.e., a graph where each node is connected to every other node. For a node v_i with k_i links, the local cluster coefficient is defined as

$$C_i = \frac{\left|\{A_{jk} : v_j, v_k \in N_i, A_{jk} = 1\}\right|}{k_i(k_i - 1)}$$

where N_i is the neighborhood of v_i, (the sub-graph formed by all the nodes v_i connects to, that is, all the out-neighbors of v_i) (Watts and Strogatz, 1998). The numerator is the number of actual connections within N_i while the denominator is the number of connections if N_i is a complete directed graph.

Closeness centrality

The farness of node v_i is defined as the sum of the lengths of shortest paths from v_i to every other node reachable by v_i along directed paths in the network. Closeness of v_i is the reciprocal of the farness and closeness centrality is simply the product of closeness and the total number of nodes n (Sabidussi, 1966).

Betweenness centrality

It measures the frequency that a node acts as a bridge in the shortest path between two other nodes, according to the following formula:

$$C_B(v) = \sum_{s \neq v \neq t} \frac{\sigma_{st}(v)}{\sigma_{st}}$$

where s, v, and t are three different nodes in the graph G(n,p) such that s and t are connected, $\sigma_{st}(v)$ is the number of shortest paths between s and t through v, while σ_{st} is the total number of shortest paths between s and t (Newman, 2005).

Betweenness centrality is usually normalized by dividing by the number of total possible node pairs $(n-1)(n-2)$ (excluding v).

Strongly connected components (SCC)

The strongly connected components of a directed graph $G(n,p)$ are sub-graphs in which there is a path – in both directions – from each node to every other node (Diestel, 2010). Therefore the number of SCC can exceed unity or be zero. When SCC = 1 the existing network is said to be fully connected, i.e., there are no isolated islands and every node can connect to every other node via a finite number of directed links.

K-core

It refers to the maximum sub-graph whose constituent nodes have at least k links (connections), where an incoming synaptic connection and an outgoing synaptic projection are equivalent in terms of counting links. Here we use the size of the K-core as a network metric.

Average in and out degree

Network connectivity of a directed graph $G(n,p)$ is represented by the entries in its adjacency matrix $A(n \times n)$. The sum of the ith row $d_i^{out} = \sum_{j=1}^{n} A_{ij}$ is the out-degree of the ith node while the sum of the ith column $d_i^{in} = \sum_{j=1}^{n} A_{ji}$ is the in-degree for the ith node. Thus, the average in- and out-degree are given by $\frac{1}{n}\sum_{i=1}^{n} d_i^{in}$ and $\frac{1}{n}\sum_{i=1}^{n} d_i^{out}$, respectively.

1.2.4 Active sub-network analysis

In order to explore the interaction between network structure and neuronal

dynamics, we examine network topology at various time points during

simulations by taking a snap shot of the network and analyzing the states of the

neurons and synaptic interconnections (directed links). If a structural connection

from neuron i to j (i.e., A_{ij} = 1) exists but the excitability of presynaptic neuron is

below some activity threshold then ostensibly the connection is nullified because

it has no postsynaptic impact. We define the sub-network that considers only

active synapses to be the functionally *active sub-network,* thereby modifying the

actual network structure according to physiological dynamics.

Synaptic excitation evokes the inward current I_{CAN}, which influences burst

generation in the Rubin-Hayes model. The model also includes inward currents

I_{NaP} and I_{syn}. We examined active sub-networks based on I_{CAN}, I_{NaP}, I_{syn}, and s

(which gates I_{syn} and, indirectly, I_{CAN}).

Each simulation consists of N bursts before rhythm cessation, with peak times (t_x)

of the inspiratory-like bursts (t_1, t_2, … , t_N) and the periods (T_x) between them (T_1,

T_2, … , T_{N-1}). We define an analytic window equal to $\min (T_{x-1}, T_x)$, where

$x \in [2, N-1]$, centered at t_x. The last time window equals T_{N-1}, centered at t_N.

For each neuron at each time step we compute the average I_{CAN} (in units of pA)

over the corresponding analytic window for each burst cycle. Although peak I_{CAN}

transiently reaches 9-15 nA, the average I_{CAN} over the duration of the analytic

window is much smaller, ranging from 0-10 pA. Then, we identify subsets of

neurons whose I_{CAN} exceeds a series of arbitrary equidistant thresholds (-2 pA, -

2.25 pA, … , -5.5 pA) within that time window, which we define as the active sub-

network. At any given level set for I_{CAN} thresholds, we sorted neurons according to their appearance (or absence) in the active sub-network. By varying the thresholds systematically, we rank-ordered the neurons according to the frequency of their appearance in the active sub-network. Then, we selectively ablated neurons in the sequence of their active sub-network rank order.

1.3 RESULTS

We simulated the preBötC using networks of Rubin-Hayes model neurons whose underlying connectivity was described by Erdős-Rényi random graphs G(n,p) with network size n = 330 and synaptic connection probability p = 0.125. We determined these values after searching (n,p) parameter space for rhythmic networks whose behavior matched the respiratory rhythm in slice preparations (Rekling et al., 2000; Hayes et al., 2012; Wang et al., 2014). E_L and g_{NaP} were fixed at -61.46 mV and 1 nS, respectively, because these parameters are physiologically realistic and within the operating range of the original Rubin-Hayes model (Rubin et al., 2009) as well as the modified version that includes I_{NaP} (Dunmyre et al., 2011). At the start of each simulation (given n, p, E_L, and g_{NaP} as described above) the networks were spontaneously rhythmic but sequentially deleting random constituent neurons slowed and then irreversibly stopped the rhythm. The cumulative tally to stop the rhythm was 39.1 ± 13.2 (mean ± SD), which represents 11.8% of the network (n=15 simulations). The above tally underestimates the experimental tally by about half, 85 ± 20. Although we proposed that premotor neurons in the preBötC, which the model lacks, could explain – at least in part – this model-experiment disparity (Wang et

al., 2014), we did not previously investigate whether the excitability parameter E_L or the conductance g_{NaP} influenced the ablation tally. To do so here, we first tested how E_L and g_{NaP} influence network behavior. Using the same network realization, i.e., the same underlying G(n,p) structure, we simulated networks with E_L spanning from -60.6 mV to -62.5 mV (E_L outside this range is not physiologically realistic) and g_{NaP} spanning from 1 nS to 1.5 nS (g_{NaP} < 1 nS is not physiologically realistic). Simulations ran for 30 s absent neuron deletions to quantify network rhythmicity (Figure 1.1, blocks are color-coded for cycle period). Lowering either E_L or g_{NaP} slows down the rhythm, such that for some (E_L, g_{NaP}) pairs the rhythm stops (black squares in Figure 1.1) whereas elevating E_L or g_{NaP} has the opposite effect (it speeds up the rhythm) such that for some (E_L, g_{NaP}) pairs the cycle period is ~1 s (red squares in Figure 1.1). Networks along the orange diagonal reflect (E_L, g_{NaP}) sets whose networks produce experimentally reasonable cycle periods of 3.5-5 sec. The ablation tally did not vary systematically along this diagonal (30.9 ± 6.3, mean ± standard deviation, n=10) when the network was subjected to the same neuron deletion sequence. However, cumulative ablation experiments performed on networks to the right of this diagonal resulted in much faster cycle periods (~1 s) and notably higher ablation tallies (red squares with ablation tallies in Figure 1.1).

These results indicate that the ablation tally depends on the initial cycle period such that the initial period could be treated as a proxy for the network robustness. Furthermore, these results indicate that (E_L, g_{NaP}) combinations that yield networks with cycle period in the range 3.5-5 sec are equally sensitive to

cumulative cellular ablation. Therefore, we used E_L = -61.46 mV and g_{NaP} = 1 nS

for the remainder of the study.
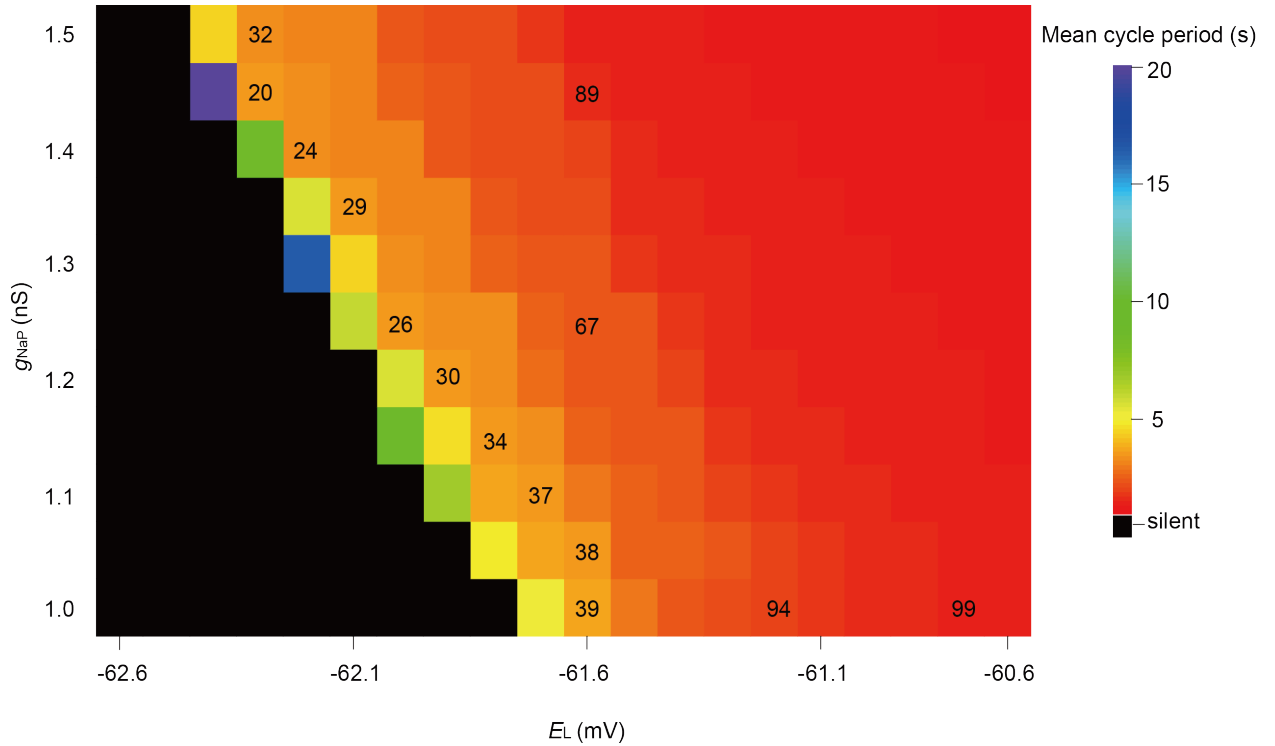
Figure 1.1. Networks of Dbx1 preBötC neurons with various E_L and g_{NaP}. Blocks show

the mean cycle period according to the colorimetric scale (right) for one 30-sec

simulation on the same network realization without any neuron deletions of each (E_L,

g_{NaP}) pair. Ablation tallies on representative parameter sets are indicated on

corresponding blocks.

1.3.1 Network connectivity analysis

Previously, we reported canonical local and global measures of topology for the

underlying graph G(n,p) at the start of a simulation and after piecewise cellular

deletions stopped the rhythm (see Supplementary file 2 in Wang *et al*., 2014).

Here, we provide more detail by tracking the state of network topology as a

function of cumulative percent of total ablations (Figure 1.2). During progressive

ablation sequences, there were no major changes in measures of local

connectivity, i.e., local metrics, such as local cluster coefficient (LCC), closeness

centrality (CC), and betweenness centrality (BC). A network is strongly

connected if a directed path exists between any two constituent nodes, which

can be quantified by the number of strongly connected components (SCC).
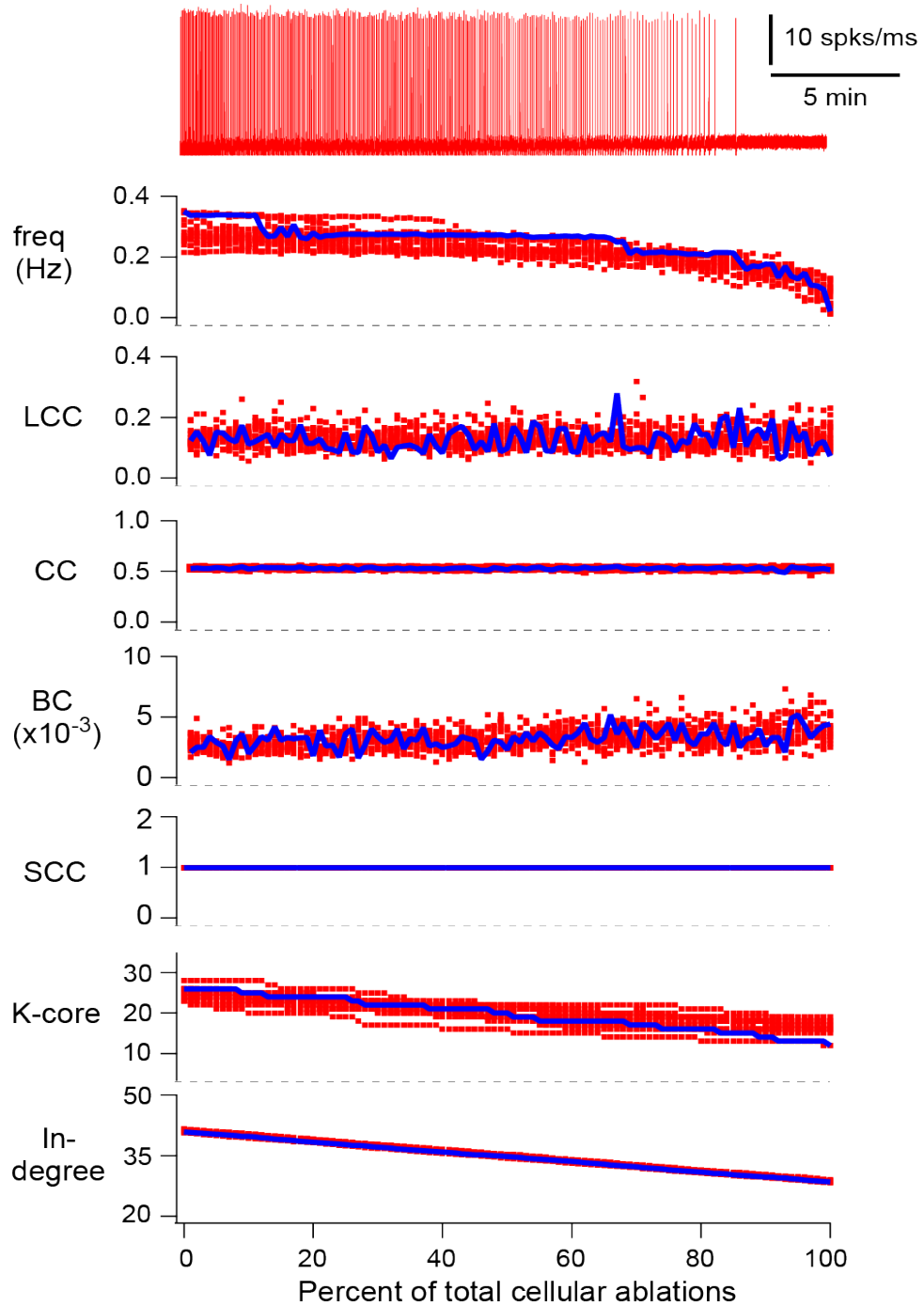
Figure 1.2. Cumulative cellular ablations in the model preBötC network. Running

time spike histogram (top, red) and plots of rhythmic burst frequency and six

discrete network metrics (global and local). The simulated experiment where a total

of 100 neurons were deleted (one per 25 simulated sec) in sequence was repeated

15 times. The running time spike histogram is shown for one representative

simulation. The top trace shows inspiratory-like burst frequency (Hz) for all 15

simulations. The abscissa (percent of total cellular ablations) is the same for

frequency and all discrete network metrics. Local cluster coefficient (LCC),

closeness centrality (CC), and betweenness centrality (BC) are plotted for each

neuron in the deletion sequence. The number of strongly connected components

(SCC), K-core and in-degree are plotted for neurons in the remaining network

during the ablation sequence. Blue symbols show the average metric (for 15

simulations) during the deletion sequence; these quantities were no longer

computed after the 100th ablation. Red symbols show the scattered data points for

all individual 15 simulations.

Cumulative deletion sequences at no point caused SCC to depart from unity (a

fully connected graph). Other global connectivity metrics such as the K-core and

the average in-degree showed linear declines. Whereas network burst frequency

declined to zero in each simulation, K-core remained above 12 and the average

in-degree remained above 28. These data indicate that the model networks

remain fully connected for the entire duration of cumulative cellular ablation

simulations that invariably stop rhythmic function. The linear drop in average in-

degree and K-core are logical effects due to cumulative neuron deletions from

the network. However, we are unable to fully identify their dynamical effects

unless we consider the loss of network structure in tandem with the neuronal

dynamics.

1.3.2 Active sub-network analysis

Next we addressed how cumulative ablations affect network excitability, which encompasses a range of cellular and synaptic factors. Network burst output, which was quantified by the running time spike histogram (Figure 1.3, red traces), did not decline during the ablation sequence. Figure 1.3 shows three individual bursts, including the final one, with faster sweep speed to emphasize their similarity. Likewise, there was not systematic drop in baseline membrane potential, as quantified by the average voltage trace for all constituent neurons in the remaining network, and shown for three representative cells (Figure 1.3, black traces).

Because the topology of the underlying graph G(n,p) remained strongly connected (Figure 1.2) and network burst output did not decline (Figure 1.3), we sought a more fine-grained analysis to identify how cumulative cellular ablations changed the system such that it stopped its autonomous rhythmic function. To begin we exploited an obvious property of the nervous system: neurons may share a synaptic connection, but unless the presynaptic partner is spiking and excitatory postsynaptic potentials (EPSPs) are registered in the postsynaptic partner, then their connection is not active. Conversely, an active synaptic connection features a presynaptic neuron whose spikes trigger EPSPs in the postsynaptic partner. Thus we analyzed *active sub-networks* consisting of synaptically engaged partners as defined above.
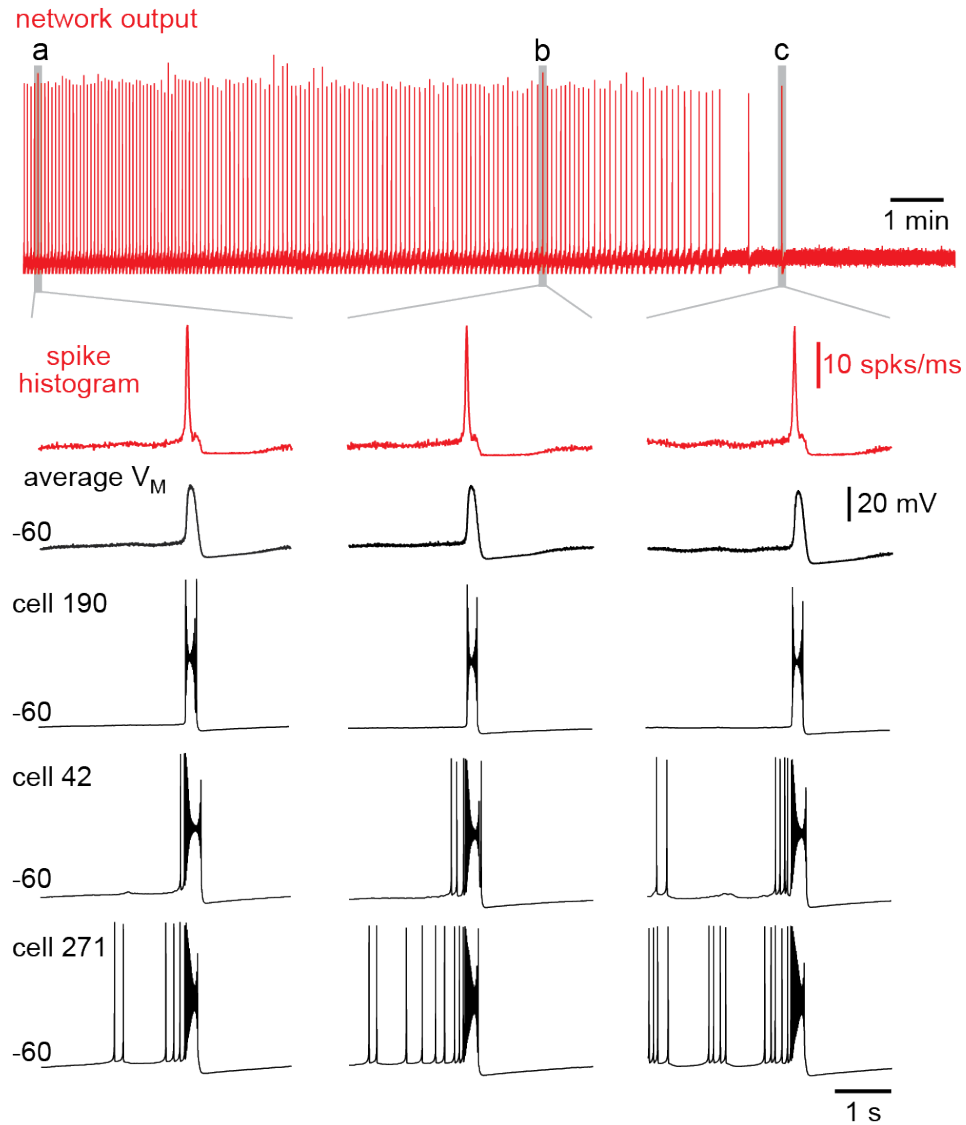
Figure 1.3. Model network bursts do not diminish during ablations sequences. Running time spike histogram (top, red) for one experiment. Time calibration (1 min) is displayed. **a**, The fifth network-wide burst. **b**, A network-wide burst after 21 deletions. **c**, The last network-wide burst after 31 deletions. The running time spike histogram (vertical calibration 10 spikes/ms) and average membrane potential (V_M, vertical calibration 20 mV) for all remaining neurons in the network for network-wide bursts (**a**, **b**, and **c**) are shown at higher sweep speed. Cells 190, 42 and 271 from the model system are shown individually. Baseline membrane potential (–60 mV) and time calibration (1 sec) apply to all traces.

18

For this analysis, spike generation indicated presynaptic activity, with corresponding postsynaptic activity was gauged by four different metrics related to I_{CAN}, I_{NaP}, I_{syn}, and state variable s.

I_{CAN} was formulated as a synaptically triggered inward current based on experimental evidence (Crowder et al., 2007; Pace et al., 2007a; Mironov, 2008, 2013; Pace and Del Negro, 2008; Rubin et al., 2009; Mironov and Skorova, 2011). Its activation depends proximally on cytosolic Ca^{2+}, which rises due to synaptic drive from presynaptic partners. Once activated, I_{CAN} generates postsynaptic bursts. Therefore I_{CAN} is a cellular parameter whose magnitude depends both on the number of presynaptic partners and their activity (topology and dynamics). Taking the average value of I_{CAN} for each neuron over an analytic time window centered at the peak of each inspiratory burst (see Methods for full definition), we generated a time series of active sub-network snapshots spanning the simulation. All the constituent neurons whose average I_{CAN} exceeded some threshold value comprised the active sub-network. Figure 1.4A plots the size of the I_{CAN} active sub-network for five different thresholds (-2, -3, -3.5, -4, and -5 pA) during the course of one representative simulation.

Note, I_{CAN} may transiently exceed 9 nA, but its average over the entire analytic window is much lower; thus threshold is one thousand-fold less than peak I_{CAN}. Cumulative cell ablation caused the I_{CAN} active sub-network size to fluctuate and progressively diminish until the rhythm stopped. I_{CAN} active sub-network size often locked onto a particular value, and remained there despite ongoing cellular ablations, then fluctuated between levels, before finally locking onto a new

smaller size. Although not illustrated in Figure 1.4, each decrement of the I_{CAN} active sub-network size was accompanied by a corresponding decrease in burst frequency (further explained below and in Figure 1.5).

We further analyzed active sub-networks based on I_{NaP}, I_{syn}, and s using the same network realization and cell-deletion sequence. A range of threshold values for I_{NaP}, I_{syn}, and s were used to compute active sub-network size (Figure 1.4B-D). I_{NaP} transiently reaches several hundred picoamperes but its average over the analysis window is much lower. We used a threshold range from ~0 to -8.0 pA (-2, -2.75, -3.5, -4.25, and -4.75 pA are shown in Figure 1.4B). Regardless of threshold, the I_{NaP} active sub-network size declined linearly without precipitous changes during the ablation sequence. These results suggest that I_{NaP} is not diagnostic for a breakdown in network function.

I_{syn} also transiently measures over one hundred picoamperes but its average over the analysis window is much lower. We used a threshold range from -0.25 to -1.2 pA (Figure 1.4C shows -0.25, -0.4, -0.5, -0.6, and -0.8 pA because larger thresholds produced active sub-networks of size zero). I_{syn} active sub-network size showed step-wise increases for intermediate thresholds with more noise compared to the I_{CAN} active sub-network. These increases occurred at approximately the same time points where the I_{CAN} active sub-network decreased in size, which suggest that deficits in I_{CAN} (and the I_{CAN} active sub-network) caused by cell ablation are partially compensated by ionotropic synaptic current I_{syn} (and the I_{syn} active sub-network).

A I_{CAN}

active sub-network size (number of neurons)

-2 pA
-3 pA
-3.5 pA
-4 pA
-5 pA

B I_{NaP}

-2 pA
-2.75 pA
-3.5 pA
-4.25 pA
-4.75 pA

C I_{syn}

-0.25 pA
-0.4 pA
-0.5 pA
-0.6 pA
-0.8 pA

D s

0.0003
0.0009
0.0015
0.0027
0.0033

burst index (1, 2, ... , 213)

21
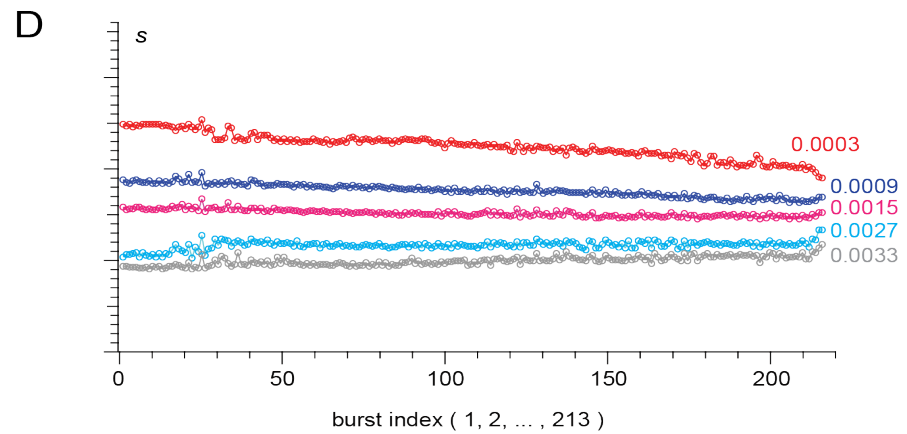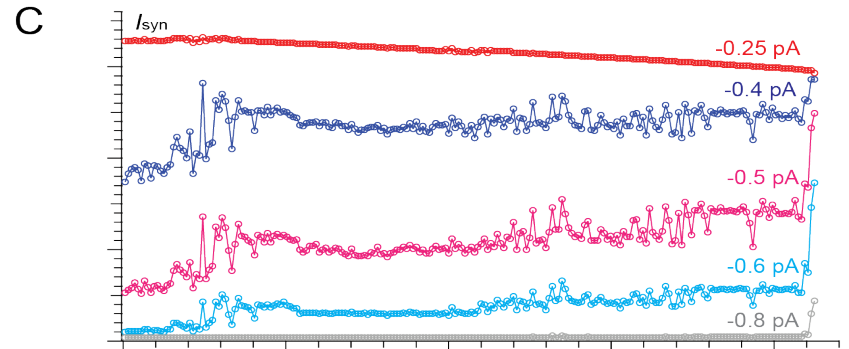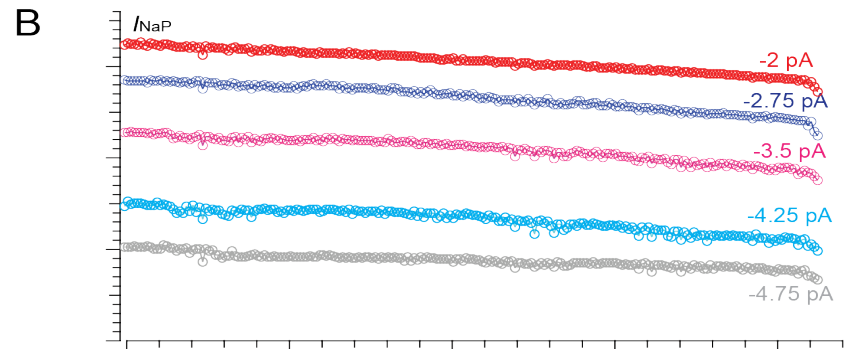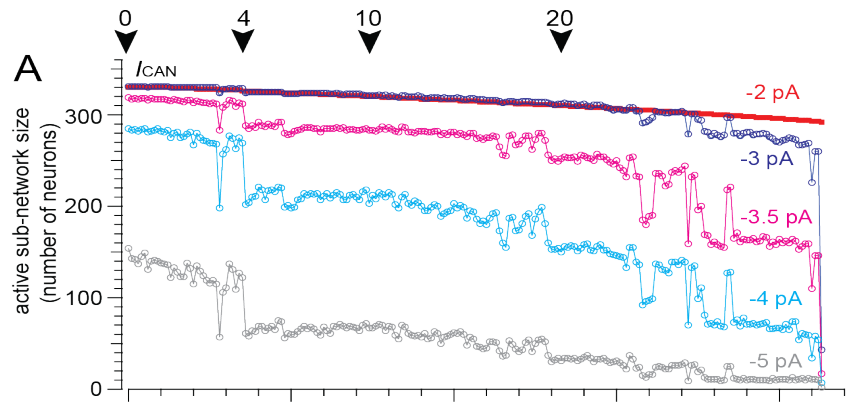
Figure 1.4. Active sub-network properties for a sequence of inspiratory-like bursts given different I_{CAN} thresholds. **A**, Active sub-network size (number of neurons) for five representative I_{CAN} thresholds (indicated above each trace) plotted versus sequential burst indices (1-213) for one simulation. Color represents different threshold values. Arrows indicate deletions 0, 4, 10, and 20. **B**, Active sub-network size (number of neurons) for five representative I_{NaP} thresholds (indicated above each trace) plotted versus sequential burst indices (1-213) for one simulation. **C**, Active sub-network size (number of neurons) for five representative I_{syn} thresholds (indicated above each trace) plotted versus sequential burst indices (1-213) for one simulation. **D**, Active sub-network size (number of neurons) for five representative s thresholds (indicated above each trace) plotted versus sequential burst indices (1-213) for one simulation.

In the case of the synaptic gating variable *s* (all thresholds on the unitless interval [0,1]), no network degradation was seen for any threshold. Only a slight increase was shown when the network-wide rhythm was approaching the rhythm termination. These results suggest that *s* is not diagnostic for a breakdown in network function.

It may seem counterintuitive that the network burst output did not change during the ablation sequence (Figure 1.3, red traces) while the I_{CAN} active sub-network size decreased stepwise (Figures 1.4A and 1.5, as well as n=6 simulations shown in Figure 1.6). Although the average I_{CAN} declined during the sequence, network burst output remained stable because I_{CAN} has a biphasic influence on the ability to generate action potentials; intra-burst spiking decreases when I_{CAN} is too low or too high. I_{CAN} generally ensures that inspiratory bursts remain more robust and larger in magnitude than is needed to sustain rhythmogenesis, q.v., (Kam et al., 2013b). However, the ability of I_{CAN} to enhance burst magnitude

causes depolarization block of spiking when its magnitude is large, which cuts down on the number of spikes per burst (Rubin et al., 2009) (also see example cells in Figure 1.3). Thus, as the average I_{CAN} decreases during the cumulative cell ablation sequence, neurons with low g_{CAN} decrease burst amplitude and generate fewer intra-burst spikes, whereas other neurons with larger g_{CAN} generate more intra-burst spikes because the ability of I_{CAN} to cause depolarization block of spiking is reduced during the course of the ablation sequence. As a result, the network burst output – as quantified by the running time spike histogram – does not decline.

To further investigate the properties of the I_{CAN} active sub-network during constituent neuron deletions, we repeatedly simulated the exact same network realization (same as Figure 1.4, starting from the same initial conditions) but we stopped the deletion sequence after 0, 4, 10, and 20 ablations and then continued the simulation for 1025 s to observe steady-state behavior. Figure 1.5 shows Poincaré maps of instantaneous burst frequency (left column) and I_{CAN} active sub-network size (right column) with a corresponding time series of network activity (insets). Points in the Poincaré maps are color-coded according to elapsed time in the series.

Under the circumstance of no neuron deletions (Figure 1.5A), instantaneous frequency and I_{CAN} active sub-network size remain tightly clustered, which shows the dynamics of the network fluctuating around a limit cycle. A representative sample shows a point at 0.308 Hz burst frequency, where the active sub-network size measures 140.
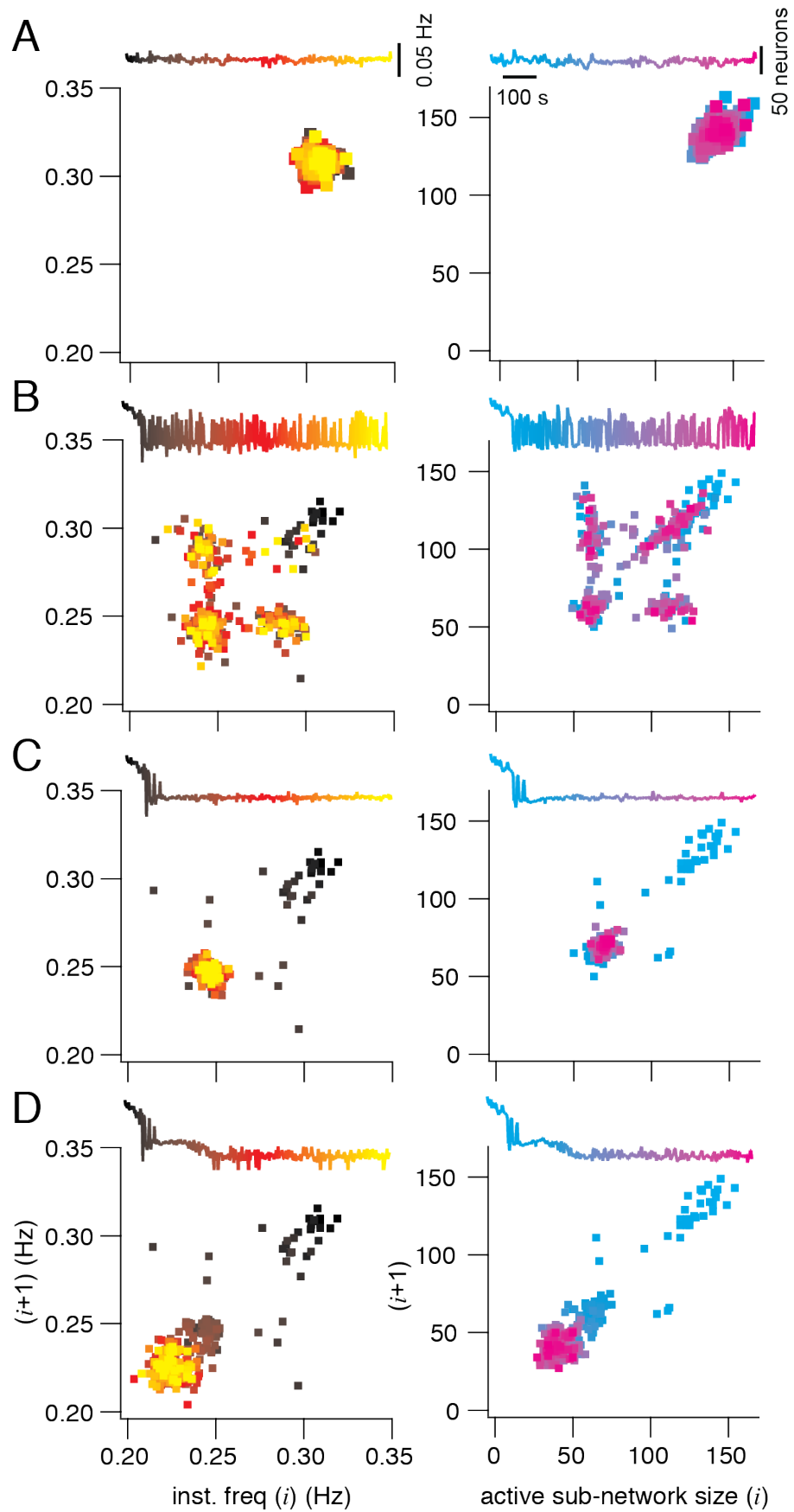
Figure 1.5. Poincaré maps of instantaneous burst frequency and active sub-network size. Each panel shows the map for frequency or active sub-network size for the cycle i+1 plotted versus the prior cycle (i). Frequency maps are at left (black to yellow). Active sub-network size maps are at right (cyan to magenta). Each Poincaré map features an inset of the time series, where temporal relations are color coded to points in the map. Vertical calibrations are given in panel (A). **A**, Poincaré maps without any neuron deletions. **B**, **C**, and **D** show the same information for the same network realization as (A) where the ablation tally was frozen after 4, 10, or 20 ablations respectively.

That steady state is impaired after only four deletions. The I_{CAN} active sub-network then alternates between the former steady state and a new lower state with representative instantaneous frequency of 0.247 Hz and active sub-network size of 67 (Figure 1.5B). The Poincaré map shows that these two states are repeatedly visited throughout the simulation (note the spread of color coding in the Poincaré map for the corresponding time series).

When six more neurons are deleted (for a total of 10), the network completes its transition to the (0.247 Hz, 67) low state (Figure 1.5C), and the Poincaré map homes in on the lower state that first appeared in the 4-deletion case (note the yellow and magenta points are concentrated at the low state).

This steady state (0.247 Hz, 67) remains the sole periodic attractor for the system despite subsequent cellular ablations 11-19. Nevertheless, another transition occurs after a total of 20 neurons are deleted, leading to a new steady state with representative instantaneous frequency of 0.223 Hz and an active sub-network of 39 neurons (Figure 1.5D).
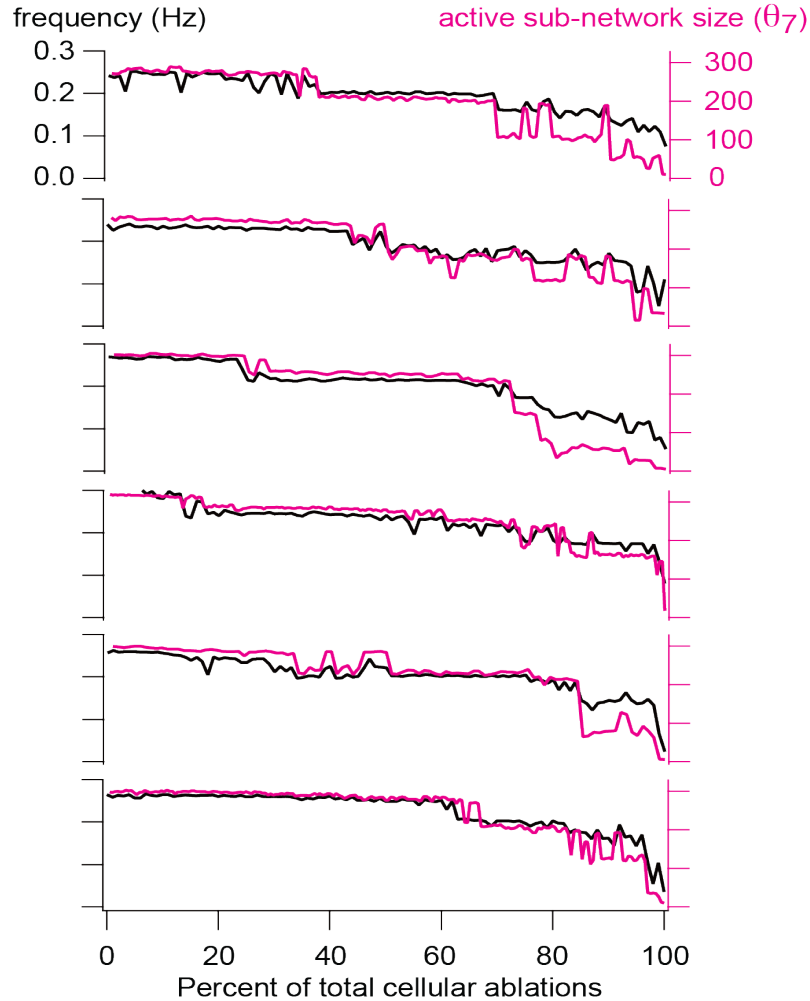
Figure 1.6. Group data for instantaneous frequency and active sub-network size. Instantaneous frequency (Hz) and active sub-network size (number of neurons) at threshold $\theta_7 = -3.5$ pA are plotted for cumulative neuron deletion simulations on six different network realizations. Black traces show instantaneous frequency (Hz); red traces show active sub-network size (number of neurons) for each cycle period, plotted versus the percentage of total cellular ablations (%).

These analyses demonstrate that cumulative deletions diminish the I_{CAN} active sub-network size in tandem with instantaneous frequency via state-flickering and step-like transitions. This dynamical behavior observed when passing through critical thresholds is seen in many other systems, from ecosystems to financial

markets (Scheffer et al., 2009) but our system shows a more complicated pathway with the state-flickering and discrete transitions. Figure 1.6 shows six different network realizations to illustrate that step-like decreases in the active sub-network size and frequency characterize how the system generally behaves in response to cumulative cellular ablation.

1.3.3 Role of I_{CAN} in model network bursts

I_{CAN} generates inspiratory bursts in the Rubin-Hayes model. Therefore, it is straightforward to predict that neurons with greater I_{CAN}, which appear more frequently in the active sub-network, play a more important role in rhythmogenesis. We ordered the neurons according to average I_{CAN}, which was correlated with in-degree, the number of presynaptic partners (Figure 1.7A). Large in-degree did not represent a greater overall synaptic conductance because g_{syn} was scaled according to total number of inputs, i.e., the product of in-degree and g_{syn} was uniform among neurons (see Methods). To test whether neurons with larger I_{CAN} were more important for rhythmogenesis, we ablated neurons according to I_{CAN} ordering (instead of randomly). Figure 1.7B shows eight cumulative-ablation simulations (eight different network realizations, eight random deletion sequences, n=8) in which targeting neurons high in the I_{CAN} ordering systematically decreased the ablation tally (black triangles, 20±7) required to stop the rhythm compared to random deletions (cyan circles, 32±9). Conversely, targeting neurons low in the I_{CAN} ordering systematically raised the ablation tally (magenta X's, 46±17) to stop the rhythm. A standard one-way ANOVA showed that there was a statistically significant effect ($\alpha = 0.05$) of

targeting condition on mean ablation tally (F = 9.1723, p = 0.0014). Post hoc

comparisons using the Tukey HSD test indicated that the mean ablation tally for

the higher I_{CAN} ordering was significantly different than the lower I_{CAN} ordering

(mean difference = 25.375, SD = 14.9467, p = 0.0009). However, the ablation

tallies of random deletion sequences did not significantly differ from the higher

I_{CAN} ordering (mean difference = 11.75, SD = 14.9467, p = 0.1415). We interpret

these data to indicate that the neurons with higher I_{CAN} tend to play a more

important role, and that deleting such neurons damages the overall ability to

spontaneously generate network bursts. Conversely, neurons with lower I_{CAN} play

a less crucial rhythmogenic role, and their selective ablation causes less

deleterious network effects.
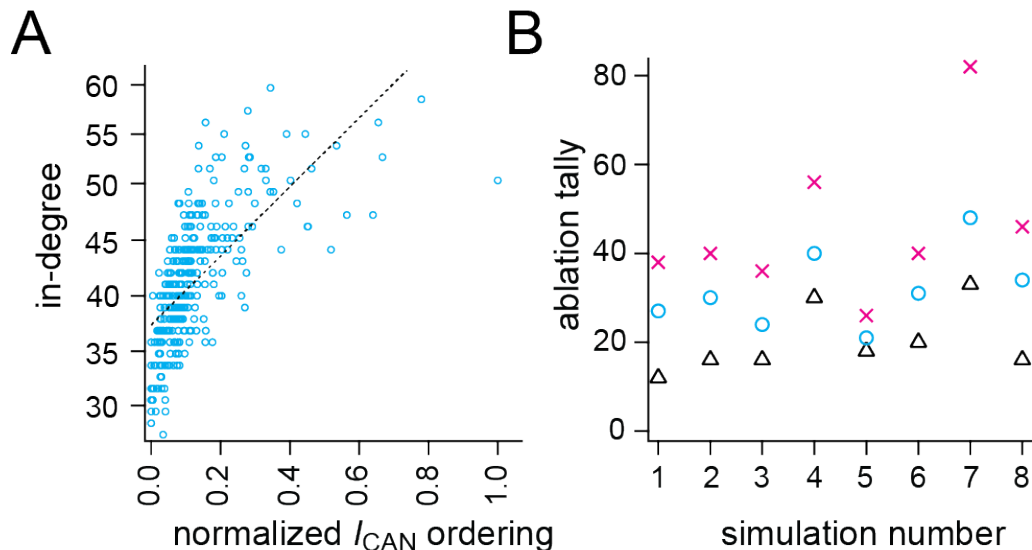
Figure 1.7. In-degree correlates with normalized I_{CAN} ordering and targeted ablation

tallies. **A**, Linear regression between in-degree (unitless) and normalized I_{CAN} ordering

among neurons in the same network. I_{CAN} order was computed based on the maximum

number of appearances in the active sub-network given 15 different thresholds. Blue

symbols show the scattered distribution of in-degrees and normalized I_{CAN} ordering.

Linear fit is shown by a dotted line. **B**, Ablation tallies (number of neurons) for three

deletion strategies on different network realizations (n=8). X-symbols mark the tally

from eight different simulations where low I_{CAN}-order neurons were selectively ablated.

Triangles mark when high I_{CAN}-order neurons were selectively ablated. Circles mark

the tally for random neuron deletions (control default strategy).

I_{CAN} active sub-network analyses of targeted cumulative ablation simulations

(Figure 1.7B, black triangles) were qualitatively identical to the active sub-

network analyses for random deletion simulations except for their lower tally (not

shown). Furthermore, the global and local metrics for the underlying graph G(*n,p*)

were also the same in targeted cumulative ablation simulations and were

indistinguishable from the results in Figure 1.2 when plotted along the same

abscissa (percent of total cellular ablations) which normalizes for the lower

ablation tally in targeted cumulative ablation simulations.

1.3.4 Recurrent excitation and pre-inspiratory latency

To investigate recurrent excitation, we tracked each neuron from its quiescent

post-burst baseline membrane potential until the peak of the subsequent

inspiratory burst. Many neurons begin spiking prior to the inspiratory burst (e.g.,

Figure 1.3). Early activation during the pre-inspiratory phase (i.e., pre-inspiratory

latency) has been hypothesized to be a key rhythmogenic property for 25 years

(Smith et al., 1990; Rekling et al., 1996; Rekling and Feldman, 1998). Pre-

inspiratory latency depends overwhelmingly on input resistance; preBötC

neurons with low g_{leak} tend to spike early in their pre-inspiratory phases (Del

Negro et al., 2002a; Koizumi and Smith, 2008).

Figure 1.8 shows constituent neurons sorted by pre-inspiratory latency for the same network realization as in Figures 1.3-1.5. Latency rank order (earliest activating neurons obtain lower rank) is plotted versus activation cycle time, i.e., when the first action potential occurs during the interburst interval. Latency for constituent neurons 1 to ~210 remains relatively fixed (Figure 1.8a, b-d lower panels). Individual network cycles are not identical (Carroll and Ramirez, 2013; Carroll et al., 2013; Kam et al., 2013b) but pre-inspiratory latency for a neuron generally remains within a few tens of ms from cycle to cycle. An early-spiking neuron does not convert to a late-spiking one, and vice versa. Interneurons low in the latency rank order (i.e., rank order 1-210) spike spontaneously and respond to synaptic input such that by cycle time ~4 s they are ostensibly all active (Figure 1.8a, b-d lower panels). However, before the network-wide burst occurs, all the remaining neurons (i.e., rank order >210) need to be recruited. The recruitment curve inflects upward as excitation spreads to the neurons with highest latency rank order.

The network-wide burst occurs where the recruitment curve is vertical. Cumulative neuron deletions shift the inflection point of the recruitment curve to higher and higher latency rank order. Sample bursts at three different time points have their inflection points at neurons with latency rank order 213, 230, and 251, respectively (Figure 1.8a-c, top panels. Note, that the figure legend reports the time points and ablation tallies that correspond to Figure 1.8a-d). In the process, the time required for the network-wide burst to occur lengthens. This recruitment

process can last ~30 s or more for an extensively lesioned network (e.g., Figure 1.8c top panel).

Cumulative ablations ultimately preclude this final transition to the network-wide burst phase. For the 200 sec of network activity shown in Figure 1.8d interneurons whose latency rank order exceeds 251 never activate.
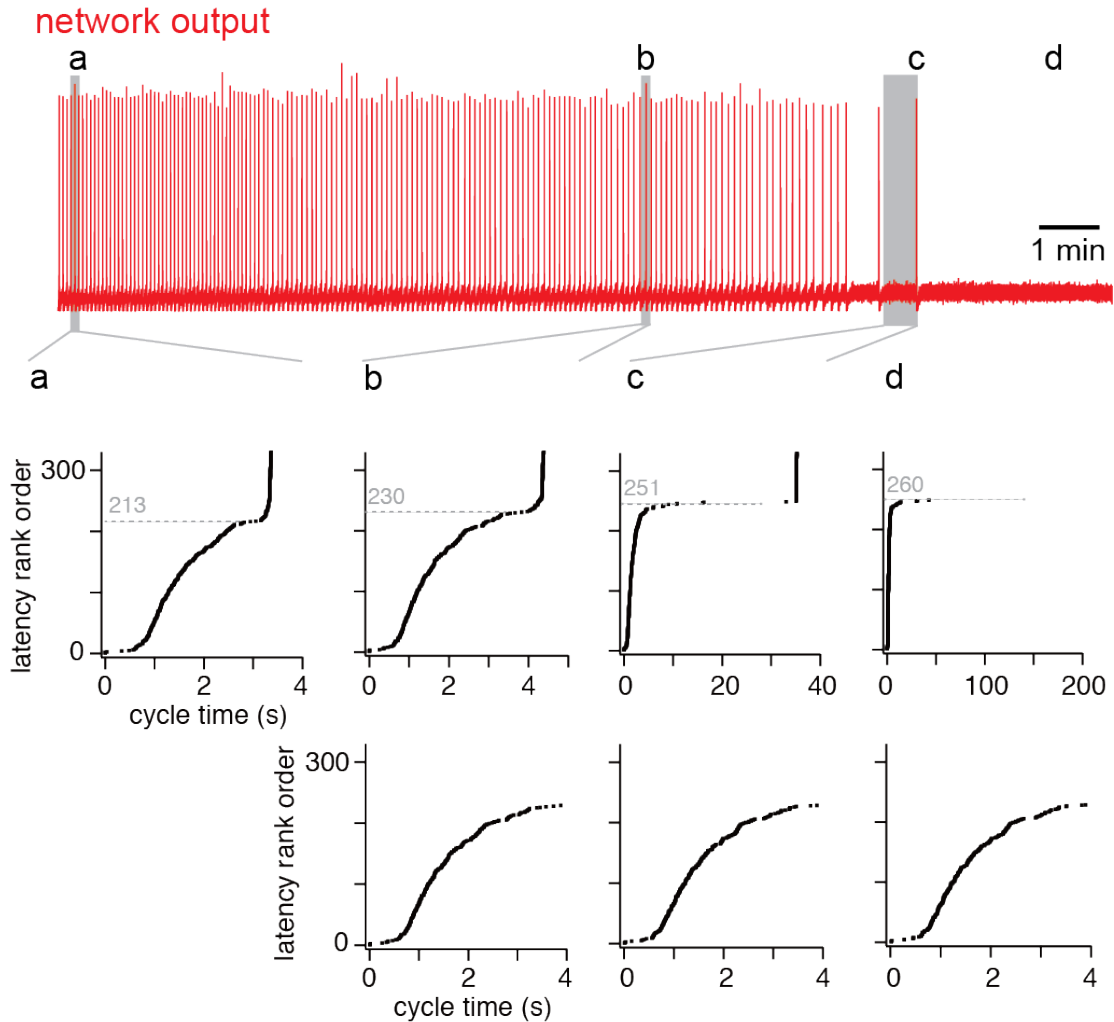
Figure 1.8. Latency rank order of all constituent neurons in the network at four specific time points in a simulation. Upper panel (red) shows the running time spike histogram for a random neuron deletion simulation. **a**, **b**, and **c** indicate three cycles leading to network-wide bursts (at time points 16 s, 557 s, 814 s, respectively). **d** indicates the time after the last burst. The middle panel shows the latency rank order (defined in

Results) for cycles **a**, **b**, and **c** and after rhythm termination (**d**) plotted versus cycle

time (in units of s). The dotted line indicates latency rank order (unitless) of the neuron

after which the curve inflects upward, leading to a network-wide burst. The lower panel

shows the same data as the middle panel but where cycle time is limited to 0-4 s,

emphasizing the similarity of **b**, **c**, and **d**.

1.3.5 Rate of recurrent excitation

Cumulative neuron ablation impairs recurrent excitation. To measure this deficit

we defined the rate of recurrent excitation during the interburst interval to be the

number of neurons that emerge from quiescence and spike per ms. Note that a

constituent neuron may spike during the interburst interval but then fall quiescent

again, and in that case would not be double counted in our analysis (only the first

spike matters). This definition enabled us to measure the speed of propagation of

activity throughout the network. We computed the rate of recurrent excitation

while the network was still functional, as well as after rhythm cessation by

applying a transient stimulus. Whenever the rate of recurrent excitation exceeded

1 neuron/ms a network-wide burst occurred, even when the interburst interval

was long. However, if the rate of recurrent excitation did not reach 1 neuron/ms,

then no network-wide burst could be spontaneously generated (Figure 1.9a-d,

which correspond to Figure 1.8a-d).

An experimental study showed that glutamate un-caging onto 4-9 preBötC

neurons evokes inspiratory bursts when the network is quiescent (Kam et al.,

2013a), which we later replicated in network models (Wang et al., 2014). To test

the hypothesis that a rate of recurrent excitation exceeding 1 neuron/ms evokes

network-wide bursts, we computed the pre-inspiratory latency and rate of

recurrent excitation for a simulated un-caging experiment, using the network

realization from Figure 1.8.
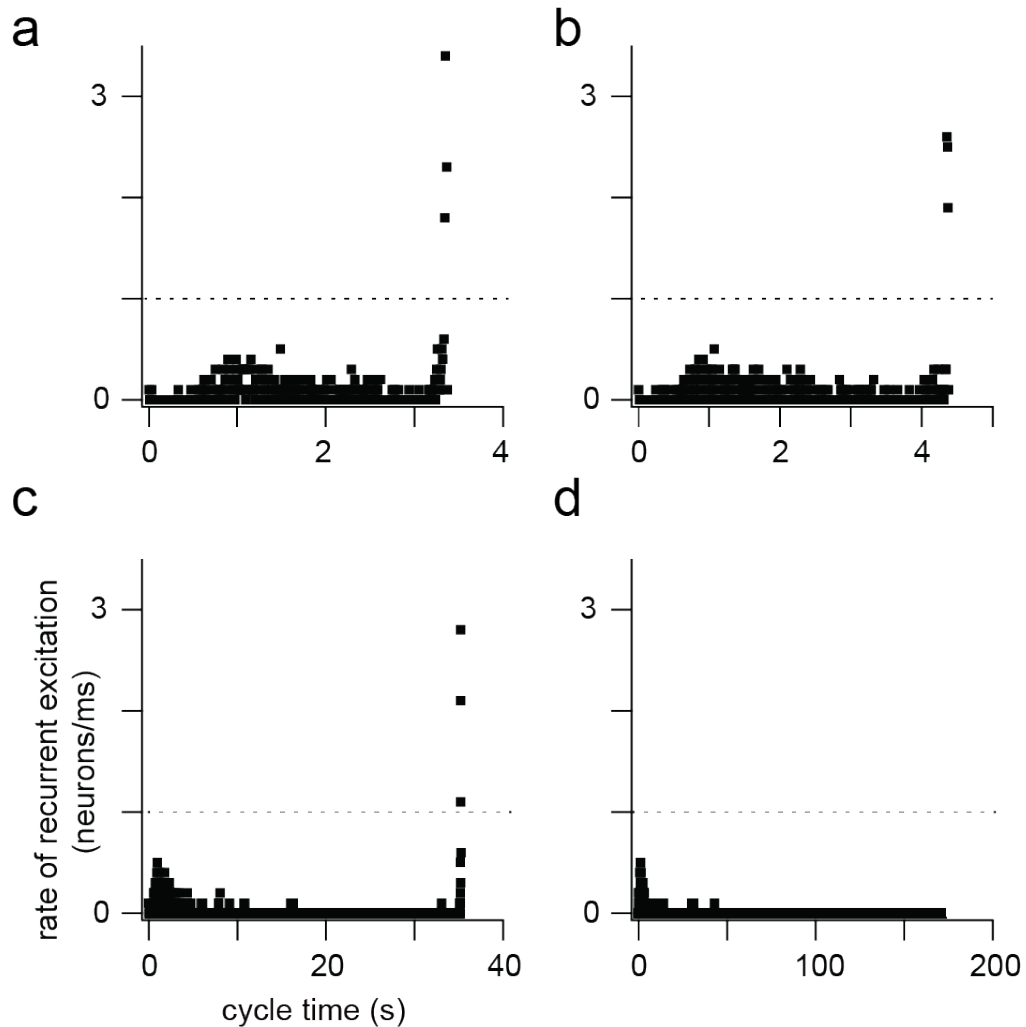
Figure 1.9. Rate of recurrent excitation (neurons/ms) plotted at four specific time

points in a simulation (same time points as in Figure 1.8). Dotted line in each panel

indicates the threshold rate (1 neuron/ms); see text for details.

The rhythm terminated after 32 ablations in that particular network realization. At

975 s the ablated network was no longer spontaneously active (Figure 1.10A),

yet simultaneously and transiently stimulating four neurons (the synaptic gating

variable was raised to $s = 0.6$ for 200 ms) evoked a network-wide burst (Figure

1.10B), showing that the network was capable of generating an inspiratory burst, but not autonomously and without sustainable rhythmicity.
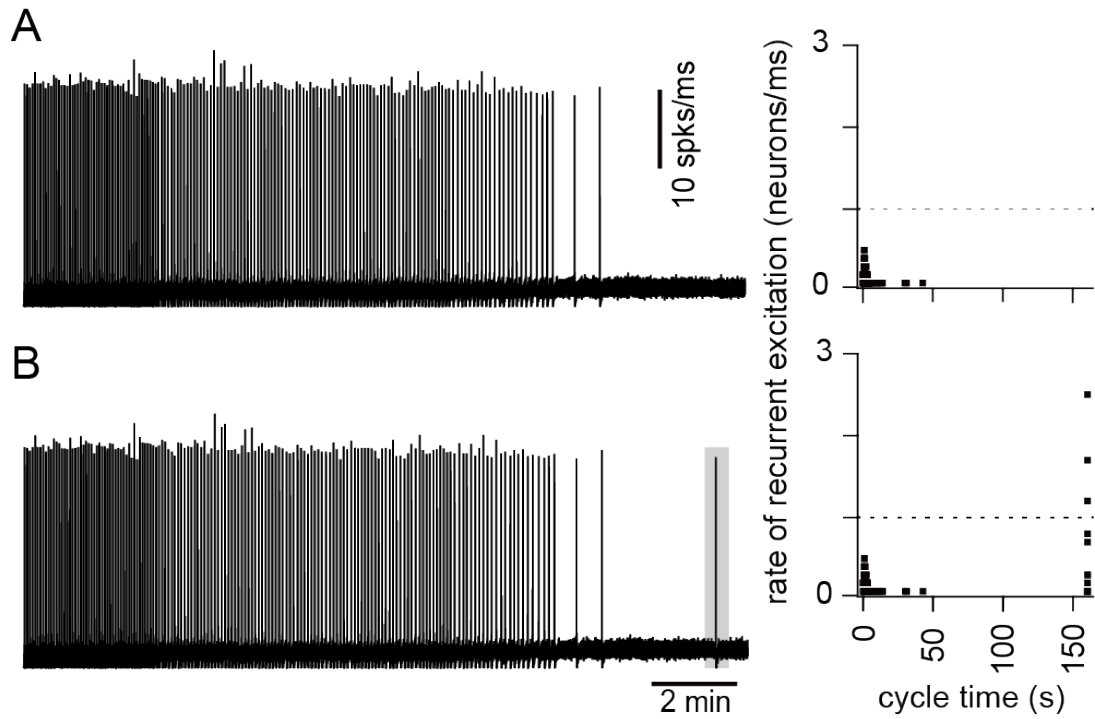
Figure 1.10. Stimulation of four individual constituent neurons (which remain in the network after cumulative ablation stops rhythmicity) evokes a network-wide burst and accelerates the rate of recurrent excitation. Panel (B) differs from (A) only in that four neurons are transiently stimulated three simulated minutes after rhythm cessation (see Materials and Methods for details of stimulation). For the same network realization and random neuron deletion sequence as in Figures 1.8 and 1.9, **A** and **B**, Running time spike histogram (10 spks/ms) versus cycle time. Time calibration applies to both traces. At right, the rate of recurrent excitation (right,) is plotted versus cycle time (s), where the cycle time is re-initialized to zero immediately following the final network-wide burst. The dotted line indicates the threshold rate of 1 neuron/ms (also see Figure 1.9).

1.4 DISCUSSION

To understand the composition of the core inspiratory central pattern generator, studies performed in vivo selectively targeted neurokinin-1 receptor-expressing

rhythmogenic preBötC neurons for saporin poisoning, which resulted in a progressive cumulative lesion (Gray et al., 2001; McKay et al., 2005). The animals developed pathological and in some cases fatal breathing phenotypes over the course of several days, during which time saporin killed off a significant fraction of the rhythmogenic preBötC core. It is not possible to know how much of the preBötC was destroyed since neither the network size at the start of those studies, nor the total number of cells killed, was known.

Subsequently, we developed a cell-specific detection and laser ablation methodology to interrogate preBötC network structure and function, as well as establish quantitative cellular parameters that govern its operation (Hayes et al., 2012; Wang et al., 2013, 2014). We reported that cumulative destruction of 85±20 (mean ± SD) interneurons derived from Dbx1-expressing precursors, corresponding to ~15% of the preBötC core population, slowed and then irreversibly stopped the respiratory rhythm. However, the experiments could not explain why it slowed down and stopped, so we sought an explanation via modeling. The model is experimentally well-founded. The Rubin-Hayes model (Rubin et al., 2009) as formulated subsequently by Dunmyre and colleagues (Dunmyre et al., 2011) serves as our preBötC interneuron. Network size (n) and connection probability (p) were determined empirically (Hayes et al., 2012; Wang et al., 2014). Parameters g_{NaP} and E_L were selected from a physiologically realistic range of values that yielded networks whose cycle period matched typical slice rhythms; varying these parameters to maintain the cycle period had no undue influence on ablation tally (see Figure 1.1). The Erdős-Rényi

configuration was chosen as a starting point. No existing data suggest that preBötC network structure conforms to either scale-free or small-world configurations, which are reasonable alternative paradigms (Watts and Strogatz, 1998; Barabási and Albert, 1999; Newman, 2010).

The model preBötC remains topologically strongly connected in response to cumulative ablation of its constituent neurons, as we determined by a suite of global and local metrics. To more deeply assess the effects of cumulative ablation we had to screen the network for measures of activity: if a presynaptic neuron is spiking and the postsynaptic neuron registers synaptic potentials (which can be monitored via I_{CAN}, I_{NaP}, I_{syn}, or s) then these partners are ostensibly part of the active sub-network.

These criteria enabled us to quantify how cumulative ablations degrade the size and rhythmic frequency of the system. Active sub-networks based on I_{NaP}, I_{syn}, or s did not reveal degradation of the core oscillator network during ablation sequences. The I_{CAN} active sub-network, however, did degenerate progressively. Curiously, the I_{CAN} active sub-network did not degrade smoothly but rather decreased in stepwise transitions. These step-like changes in frequency and size were novel and completely non-intuitive results in a respiratory network modeling study. Although each network realization is unique, step-like degradation of the I_{CAN} active sub-network was a characteristic pattern that occurred in every simulated experiment. The steps occurred at unpredictable intervals such that stable periodic regimes could be maintained during several consecutive cellular ablations before another transition. These transitions often (but not always)

exhibited bistability where the I_{CAN} active sub-network alternated between two states, each having a characteristic active sub-network size and network-wide burst frequency. These results indicate that the core oscillator defends stable periodic regimes, and can do so over the course of sequential deletions (e.g., ablations 11-19, see Figure 1.4A). Nevertheless, as constituent cells are lost to ablation, the I_{CAN} active sub-network gets progressively smaller and the rhythm slows down in tandem until spontaneous functionality is unsustainable.

Based on previously published modeling results (Wang et al., 2014), this study provides a more complete explanation for rhythm cessation in the preBötC in response to cumulative neuron deletions. Additionally, we define and then analyze active sub-networks to discover that I_{CAN} coupled with in-degree is an important factor to explain burst initiation and the sustainability of spontaneous rhythms. Finally, we discovered that the rate of recurrent excitation is the key factor for maintaining spontaneous rhythmogenic function in the network model. By rank ordering the neurons by pre-inspiratory latency, we found that cumulative neuron deletions would decelerate the process of recurrent excitation such that when the rate of recurrent excitation fails to achieve a threshold of 1 neuron/ms, then spontaneous rhythm and burst generation is precluded (further discussed below).

1.4.1 Cellular factors for rhythmogenesis

As a synaptically triggered inward current, I_{CAN} manifests postsynaptic burst-generating capacity. We ordered constituent neurons based on average I_{CAN} magnitude, which positively correlated with in-degree. Constituent large in-

degree neurons have a greater probability of synaptic inputs arriving synchronously, compared to lower in-degree neurons, which maximizes I_{CAN} activation. In selective targeting experiments that preferentially ablated cells according to I_{CAN} rank-order, rhythm cessation occurred at lower tallies, which verifies the importance of I_{CAN} for rhythmogenesis in this model system. Inspiratory burst generation relies on I_{CAN} in the Rubin-Hayes model (Rubin et al., 2009), as well as in other contemporary models (Toporikova and Butera, 2011; Jasinski et al., 2013) Experimental evidence shows that I_{CAN} is expressed in preBötC neurons and contributes substantially to bursts (Crowder et al., 2007; Pace et al., 2007a; Mironov, 2008, 2013; Pace and Del Negro, 2008; Rubin et al., 2009; Mironov and Skorova, 2011). Nevertheless, the importance of I_{CAN} and burst generation has recently been challenged by an alternative mechanism based on less intense 'burstlets' that may reflect recurrent excitation at the network level in the absence of robust bursts and motor output (Kam et al., 2013b). Our modeling framework could be correct – or correct in part – about recurrent excitation and network dynamics, while wrongly asserting the central importance of I_{CAN}, but that remains to be evaluated.

The other major cellular property that promotes network rhythmogenesis was gleaned from pre-inspiratory latency analysis. Constituent neurons with high input resistance (low g_{leak}) are more sensitive to incoming synaptic inputs, which enhance graded potentials postsynaptically and lead to early spiking in the pre-inspiratory phase. Therefore, these high input resistance neurons play a more important role than those with low input resistance in the process of recurrent

excitation. This conclusion has considerable experimental credibility (Del Negro et al., 2002a; Koizumi and Smith, 2008).

We rank-ordered the constituent neurons according to pre-inspiratory latency and plotted latency rank order versus cycle time (Figure 1.8). The slope of this curve (its derivative) quantifies constituent neurons recruited per unit time, a measure of the rate of recurrent excitation (Figure 1.9). Whether spontaneously active, or evoked to burst via a transient stimulus, if the rate of recurrent excitation does not achieve 1 neuron/ms, then a network-wide burst cannot occur. Therefore, rhythm cessation reflects not destruction of network topology or diminution of excitability, but rather impediments in the ability of excitation to spread through network constituents and achieve a threshold recruitment rate, which here measured 1 neuron/ms.

This threshold rate pertains to the model network assembled from Rubin-Hayes neurons according to parameters listed above (Materials and methods). The real system – or other models – may exhibit a slightly different threshold rate, but our analyses suggest that a particular threshold rate of recurrent excitation most likely exists and governs when spontaneous rhythms are sustainable in the preBötC whether studied in vivo, in vitro, or in silico.

I_{NaP} is widely expressed in preBötC neurons. Here we set g_{NaP} to 1 nS, which facilitates the richest set of dynamical behaviors in the Rubin-Hayes model (Dunmyre et al., 2011). I_{NaP} is a predominantly somatic current that facilitates high frequency intra-burst spiking which also underlies voltage-dependent bursting in preBötC neurons after synaptic isolation (Del Negro et al., 2002a,

2002b, 2005; Peña et al., 2004; Ptak et al., 2005). However, inspiratory synaptic

drive appears to be largely mediated by convolved synaptic intrinsic currents and

expressed on dendrites (Pace et al., 2007a; Mironov, 2008; Pace and Del Negro,

2008; Del Negro et al., 2011). Synaptic integration does not appear to be

boosted by I_{NaP} (Pace et al., 2007b; Koizumi and Smith, 2008). Elevating g_{NaP},

while balancing E_L to maintain slice-like cycle period in the network, did not

systematically influence the ablation tally needed to cause rhythm cessation.

Furthermore, I_{NaP} active sub-networks did not degrade in response to cumulative

ablations (see Figure 1.4B). Therefore, in Erdős-Rényi-structured preBötC-like

networks assembled from Rubin-Hayes interneuron models, we conclude that

I_{NaP} does not play a specialized rhythmogenic role. Nevertheless, the role of I_{NaP}

continues to be investigated at different stages of development, in different

physiological states (e.g., hypoxia and hypercapnia), and in different model

organisms (e.g., rats, mice, and hamsters, among others).

1.4.2 Disparities between experiments and simulations

In experiments we observed an exponential relaxation of the respiratory motor

output amplitude in response to 10-15 cumulative Dbx1 neuron deletions (Wang

et al., 2014). However, no such precipitous decrement in output amplitude

occurred in simulations.

Experimentally the amplitude of respiratory motor output is monitored via

hypoglossal (XII) nerve discharge (Funk and Greer, 2013). Dbx1 preBötC

neurons in some cases project to the XII nucleus and thus serve in a premotor

capacity (Wang et al., 2014). Deleting such neurons experimentally would

presumably impair burst output amplitude without obligatory effects on burst frequency. In contrast, the amplitude in simulations is computed from the running-time spike histogram, which is based on the raster plot of preBötC rhythmogenic neurons. As explained earlier, I_{CAN} has a biphasic influence on action potential generation. Intra-burst spiking decreases when I_{CAN} is too low or too high. Therefore, as constituent neurons are deleted from the network and the overall I_{CAN} decreases, spike output capability is enhanced in some neurons, while in others that capability is diminished; the net result is that network-wide intra-burst spiking is maintained in the model system despite cumulative cellular ablations. This model does not account for the premotor population. Here, each model neuron contributes equally to the rhythmic amplitude. We contend that a more complete simulation of the respiratory brainstem network, which accounts for an intercalated premotor population of Dbx1 neurons, will be necessary to fully replicate the experimental results, particularly the drop in amplitude in response to cumulative ablation (Wang et al., 2014).

Experimentally, 85±20 constituent neuron deletions irreversibly terminated the respiratory rhythm (Wang et al., 2014), whereas the tally measured 39.1 ± 13.2 (mean ± SD) in simulations. What can explain this disparity?

We detected 705 Dbx1 neurons in the preBötC experimentally. Putative rhythmogenic neurons were identified by fluorescent protein expression despite the fact that Dbx1 derived neurons are not limited to the preBötC and that not all valid Dbx1 targets are respiratory (Bouvier et al., 2010; Gray et al., 2010; Picardo et al., 2013). In addition, a subset of Dbx1 preBötC neurons projects directly to

the XII motor nucleus and thus may consist of premotor rather than rhythm-generating interneurons. Deleting these neurons is superfluous with regard to the tally of cellular ablations required to impair network functionality (Wang et al., 2014). By contrast, our simulations assume that all constituent neurons in the model network are rhythmogenic; therefore, removing any one of them can diminish network functionality. The biphasic effect of I_{CAN} on intra-burst spiking (see 'Active sub-network analysis' in Results) explains why the amplitude of inspiratory burst-related spiking does not decrease despite progressive decreases in the average magnitude of I_{CAN}.

Another possible reason for the disparity in the ablation tallies may pertain to discrepancies in network complexity. The actual topology of the Dbx1 interneuron network in the preBötC remains unknown. Our model is reasonably well configured based on empirical data but it may lack clustering effects among constituent neurons that, in the real system, would endow greater robustness and increase the ablation tally needed stop the rhythm. We used Erdős-Rényi graphs for network structure because it is the most generalized random network model without any additional assumptions on the intrinsic positional differences among neurons such as hubs or small-world properties. Thus, special network structures (e.g., hubs or small worlds) cannot explain rhythm cessation following cumulative cellular ablation.

Even though the experimental and simulation tallies are different, we contend that the model may provide insights into why the real preBötC core oscillator ceases spontaneous function when subjected to piecewise disassembly in vivo

or in vitro. Cellular ablations do not destroy the structure of the underlying network (its constituent cells remain connected formally even after 30% of the network is removed), but rather hinder the rate at which neurons can recruit one another to start spiking in the interburst interval, i.e., the rate of recurrent excitation. For arrhythmic conditions, such as the in vitro model in its lesioned state, or the preBötC under pathological conditions in vivo (including saporin lesions or disease states leading to respiratory failure) our analyses suggest that restoration of network functionality may be possible if simultaneous activation of several units can be accomplished via exogenous stimulation or the strength of excitatory transmission among constituent neurons can be augmented.

CHAPTER 2. Functional interactions between mammalian respiratory rhythmogenic and premotor circuitry

2.1 INTRODUCTION

Inspiratory breathing movements emanate from neural activity in the preBötzinger complex (preBötC) (Smith et al., 1991; Feldman and Del Negro, 2006; Feldman et al., 2013; Moore et al., 2013) as well as a network of premotor neurons that transforms inspiratory rhythm into a coordinated set of motor commands serving ventilation. Because our knowledge of the preBötC presently exceeds that of the premotor circuits, we employed experiments and modeling to advance understanding of how brainstem premotor neurons interconnect with the preBötC and influence inspiratory-related motor patterns.

Interneurons whose progenitors express the homeodomain transcription factor Dbx1 (hereafter referred to as Dbx1 neurons) may comprise the rhythmogenic core of the preBötC (Bouvier et al., 2010; Gray et al., 2010; Picardo et al., 2013). Rhythms that originate in the preBötC drive a complement of respiratory muscles including the tongue protractor (genioglossus) that helps maintain airway patency during breathing behavior. Hypoglossal (XII) motoneurons in the dorsomedial medulla innervate these protractor muscles. XII premotor neurons, which convey inspiratory-related drive to XII motoneurons, have been identified in the intermediate reticular formation intercalated between the preBötC and the XII motor nucleus (Ono et al., 1994; Woch et al., 2000; Peever et al., 2002; Koizumi et al., 2008; Fregosi et al., 2011). Interestingly, Dbx1 neurons also situated in the intermediate reticular formation adjacent to preBötC constitute a significant set of XII premotor neurons (Wang et al., 2014; Revill et al., 2015).

Positing that Dbx1 preBötC neurons largely contribute to rhythmogenesis and Dbx1 reticular neurons primarily contribute to premotor drive transmission, we tested those roles experimentally in a rhythmically active slice model of breathing (Funk and Greer, 2013). We employed photonics to cumulatively destroy Dbx1 preBötC neurons while monitoring rhythmic motor output in real time. After ~15 ablations the magnitude of inspiratory motor output measured from the XII nerve root decreased by half; further ablations slowed spontaneous rhythmic frequency, which ceased after an ablation tally of 85 ± 20 (Wang et al., 2014). Later we adapted the technique to destroy Dbx1 neurons from the intermediate reticular formation, which decreased the magnitude of XII motor output linearly without affecting the frequency of the respiratory rhythm (Revill et al., 2015).

The observations that ablations in the preBötC exerted an immediate and profound amplitude effect on XII motor output, whereas cumulative ablations in the reticular formation attenuated XII motor output in a graded manner, were non-intuitive and unexpected results. Therefore, we aimed to construct a model XII premotor network (i.e., a simulated intermediate reticular formation) to connect to an established model preBötC (Song et al., 2015) such that when cumulatively deleting neurons from either population, the frequency and amplitude of the fictive nerve output would match the experimental results in the targeted laser ablation experiments summarized above.

This study provides a feasible blueprint for the assembly of a rudimentary rhythm and pattern-generating neural circuit that improves our understanding of how

Dbx1-derived interneurons of the lower medulla generate and regulate breathing behavior.

2.2 MATERIALS AND METHODS

2.2.1 Rubin-Hayes preBötC interneuron model

Each preBötC neuron is a Rubin-Hayes model (Rubin et al., 2009; Dunmyre et al., 2011), featuring Hodgkin-Huxley-like spiking currents with four additional currents: calcium-activated non-specific cation current (I_{CAN}) (Crowder et al., 2007; Pace et al., 2007a; Mironov, 2008, 2013; Pace and Del Negro, 2008; Mironov and Skorova, 2011), excitatory synaptic current mediated by AMPA receptors (I_{syn}) (Funk et al., 1993; Ge and Feldman, 1998), persistent sodium current (I_{Na-P}) (Del Negro et al., 2002a; Ptak et al., 2005; Koizumi and Smith, 2008) and Na/K ATPase pump current (I_{pump}) (Del Negro et al., 2009; Krey et al., 2010). The Rubin-Hayes model is in the public domain (http://senselab.med.yale.edu/modeldb/ShowModel.asp?model=125649).

The current-balance equation takes the form:

$$C\frac{dV}{dt} = -I_{leak}(V) - I_{Na}(V, m, h) - I_K(V, n) - I_{CAN}(V, Ca) - I_{NaP}(V, h_{Na-P}) -$$
$$I_{syn}(V, s_1 \dots s_N) - I_{pump}(Na)$$

where

$$\frac{dx}{dt} = (x_\infty(V) - x)/T_x(V)$$

$$\frac{ds}{dt} = \left((1 - s)s_\infty(V) - k_s s\right)/T_s$$

$$\frac{dCa}{dt} = \varepsilon\left(\sum_{i=1}^N s_i \cdot k_{synCa} - k_{Ca}(Ca - Ca_\infty)\right), \text{ and}$$

$$\frac{dNa}{dt} = \alpha(-I_{CAN}(V, Ca) - I_{pump}(Na))$$

describe the evolution of the state variables, for each x in $\{m, h, n, h_{Na-P}\}$.

Whole-cell currents are described with chord-conductance equations, in some cases modified for Ca^{2+} or Na^+ gating (Li and Rinzel, 1994):

$$I_{leak}(V) = g_{leak}(V - E_L)$$

$$I_{Na}(V, m, h) = g_{Na}m^3 h(V - E_{Na})$$

$$I_{Na-P}(V, h_{Na-P}) = g_{Na-P}m_{Na-P\infty}h_{Na-P}(V - E_{Na})$$

$$I_K(V, n) = g_K n^4(V - E_K)$$

$$I_{CAN}(V, Ca) = g_{CAN}(V - E_{CAN})/(1 + \exp((Ca - k_{CAN})/\sigma_{CAN}))$$

$$I_{syn}(V, s_1 \ldots s_N) = g_{syn}\sum_{i=1}^{N} s_i(V - E_{syn})$$

where N is the number of presynaptic neurons, $\{s_1 \ldots s_N\}$ reflects presynaptic s variables, and

$$I_{pump}(Na) = r_{pump}(\phi(Na) - \phi(Na_\infty)).$$

The remaining functions, including those for voltage-dependent channel gating, are:

$$x_\infty(V) = 1/\left(1 + \exp\left(\frac{V - \theta_x}{\sigma_x}\right)\right)$$

$$T_x(V) = T_{x_{max}}/\cosh\left(\frac{V - \theta_x}{2\sigma_x}\right)$$

$$\phi(Na) = Na^3/(Na^3 + k_{Na}^3).$$

Model parameters are set to the following values for preBötC neurons:

$C = 45\ pF, g_{leak} = 3 \pm 0.78\ nS, E_L = -61.46\ mV, g_{Na} = 150\ nS, E_{Na} = 65\ mV,$

$g_{Na-P} = 1\ nS, g_K = 30\ nS,\ E_K = -75\ mV, g_{CAN} = 4 \pm 0.75\ nS, E_{CAN} = 0\ mV,$

$\theta_m = -36\ mV, \sigma_m = -8.5\ mV, T_{m_{max}} = 1\ ms, \theta_h = -30\ mV, \sigma_h = 5\ mV,$

$$T_{h_{max}} = 15\ ms, \theta_n = -30\ mV, \sigma_n = -5\ mV, T_{n_{max}} = 30\ ms, Na_\infty = 5\ mM,$$

$$\theta_s = 15\ mV, \sigma_s = -3\ mV, T_s = 15\ ms, \theta_{m_{Na-P}} = -40\ mV, \sigma_{m_{Na-P}} = -6\ mV,$$

$$\theta_{h_{Na-P}} = -48\ mV, \sigma_{h_{Na-P}} = 6\ mV, T_{Na-P} = 1000\ ms, k_{Ca} = 22.5\ ms^{-1},$$

$$\theta_{CAN} = 0.9\ \mu M, \sigma_{CAN} = -0.05\ \mu M, k_s = 1, k_{synCa} = 1200\ \mu M \cdot ms^{-1},$$

$$r_{pump} = 200\ pA, k_{Na} = 10\ mM, Ca_\infty = 0.05\ \mu M, g_{syn} = 3.25\ nS,$$

$$\varepsilon = 0.0007, \alpha = 6.6 \times 10^{-5}\ mM \cdot pA^{-1} \cdot ms^{-1}, E_{syn} = 0\ mV$$

We modeled XII premotor neurons using the Rubin-Hayes formulation with a few parameters adjusted to fit measurements of respiratory premotor neurons (Koizumi et al., 2008):

$$E_L = -65 \pm 1.8\ mV, g_{leak} = 1.23 \times (3 \pm 0.78)\ nS, g_{Na-P} = 0.45\ nS.$$

The synaptic gating variable s, which was coupled to the ordinary differential equation for Ca^{2+}, represents both ionotropic and metabotropic glutamatergic receptor activation.

2.2.2 Network model of preBötC and reticular formation

We previously modeled the preBötC as a directed Erdős-Rényi random graph (Newman et al., 2001). The model preBötC with n = 250 interneurons and interconnection probability p = 0.1625 produces a rhythm with a realistic mean cycle period (Wang et al., 2014).

Premotor interneurons that project to inspiratory-related XII motoneurons have been identified in the intermediate reticular formation, which is intercalated between the preBötC and the XII nucleus (Dobbins and Feldman, 1994; Ono et al., 1994; Peever et al., 2002; Chamberlin et al., 2007; Koizumi et al., 2008; Volgin et al., 2008; Stanek et al., 2014). Since the intermediate reticular

formation contains oral-motor as well as respiratory interneurons, the total

number of XII premotor neurons dedicated to respiration is unknown. Koizumi

and colleagues (Koizumi et al., 2008) functionally identified 146 XII premotor

neurons in rhythmically active slices preparations from neonatal rodents *in vitro*:

136 located in the intermediate reticular formation and 10 within the dorsal part of

the preBötC. These functionally identified premotor interneurons expressed a

variety of transmitter phenotypes.

Our model network selectively incorporates glutamatergic Dbx1-derived premotor

neurons in the intermediate reticular formation and the dorsal preBötC (Wang et

al., 2014; Revill et al., 2015). We fixed the Dbx1 reticular premotor population

size at $n = 100$, which is based on Koizumi's (2008) estimate but slightly reduced

to account for functionally identified inspiratory XII premotor neurons that are not

glutamatergic. Reticular premotor neurons receive synaptic input from the

preBötC, but do not project back to it (Koshiya and Smith, 1999; Koizumi et al.,

2008). This coupling arrangement reflects the orthodromic mode of transmission

from preBötC to premotor neurons to genioglossus XII motoneurons. All synaptic

connections in this study are excitatory.

To represent the fraction of Dbx1 XII premotor neurons within the preBötC (Wang

et al., 2014), we randomly selected 50 constituent neurons that interconnect

locally in the preBötC but furthermore contribute directly to network output (thus

modeling a projection to the XII nucleus). Fictive nerve output was quantified as a

running-time spike histogram from the raster plot of spike activity in all 100

reticular premotor neurons and 50 preBötC neurons (i.e., 20% of the preBötC

population) that project directly to the XII nucleus (Wang et al., 2014). The amplitude of this ensemble network rhythm represents fictive XII nerve output, i.e., it mimics experimental recordings of XII motor nerve roots *in vitro* (Smith et al., 1991; Funk and Greer, 2013) and thus is depicted as distinct sites of projection in Figure 2.1A.
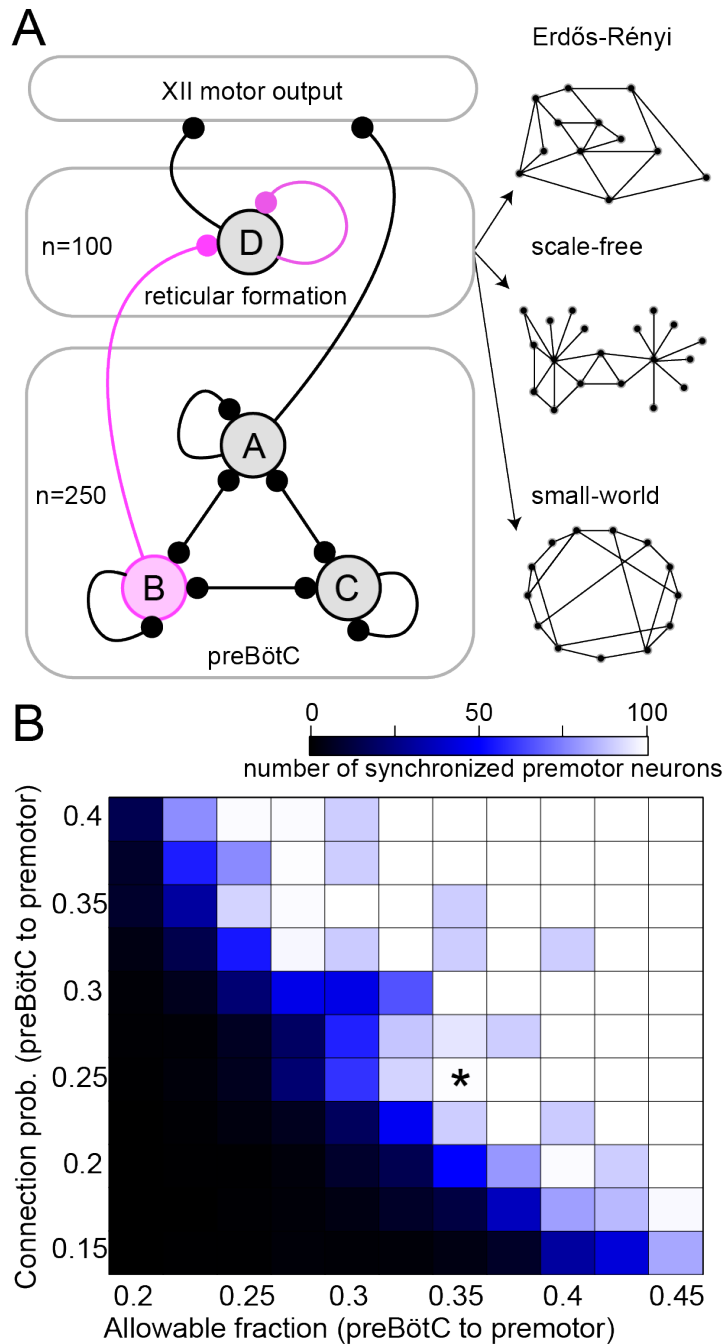
Figure 2.1. Diagram of the preBötC, intermediate reticular formation, and XII nucleus, which generate inspiratory related rhythm and motor output, respectively. **A**, The preBötC network (bottom lozenge) consists of 250 neurons. Some preBötC neurons (set B) are allowed to connect to the reticular formation premotor system (middle lozenge), 50 preBötC neurons (set A) directly connect to model XII nucleus to influence fictive nerve output. The rest of the preBötC neurons only connect within the preBötC (set C). All preBötC neurons (sets A, B, C) are allowed to connect to each other with a fixed connection probability. The reticular premotor system consists of 100 neurons (set D) that all project to the model XII nucleus. Circles represent neuron populations and lines with round terminations signify directed synaptic projections. Synaptic projections among neurons within the same population are indicated by a recurrent connection (e.g., the line projecting from A back into A.) Interconnection between the preBötC and the reticular premotor system is either Erdős-Rényi (random) or obeys an anti-preferential attachment rule (see text for details). The synaptic interconnection for constituent neurons of the reticular premotor system is either Erdős-Rényi, scale-free or small-world (B-C, see text for details). Specific connection topologies are not accurately represented in this schematic, which rather shows a basic schematic of the whole system. We also show three cartoon diagrams representing respectively three characteristic networks: Erdős-Rényi (A, right top), scale-free (A, right middle) and small-world network (A, right bottom). **B,** interconnection between model preBötC and reticular premotor networks as a function of the allowable fraction, i.e., the fixed proportion of preBötC neurons that may connect to reticular premotor neurons, and probability that they do so. Blocks show the number of synchronized premotor neurons according to the colorimetric scale (top) for one 30-s simulation. No simulated deletions were performed. The asterisk indicates the parameter pair (0.36, 0.25) that ensures full synchronization of constituent premotor neurons.

Figure 2.1A provides a diagram of the model system. Black elements, including the population size of the preBötC and reticular premotor population, remain fixed, whereas magenta elements were adjusted, such as 1) the specific number of preBötC neurons that project to the reticular formation, 2) the connectivity from preBötC to reticular premotor neurons, as well as 3) the connectivity among reticular premotor interneurons.

The fraction of preBötC neurons that were candidates for projection to the reticular premotor neurons (i.e., allowable fraction) was varied from 0.2 to 0.45 with a step size of 0.025. Whether a preBötC neuron in this reticular-projecting subset actually synapsed onto each individual XII premotor neuron was further governed by a connection probability that varied from 0.15 to 0.4 with a step size of 0.025. For each parameter pair we performed 10 simulations (i.e., 10 unique network realizations). Qualitative network behavior appears to depend inversely on the allowable fraction of projected preBötC neurons and the connection probability. If the allowable fraction equals or exceeds 0.35 and the connection probability exceeds 0.2, then the XII premotor population fully synchronizes with the preBötC rhythm (Fig. 2.1B).

Connectivity among XII premotor neurons is unknown, so we examined three canonical network structures: Erdős-Rényi (random), scale-free, and small world (Watts and Strogatz, 1998; Barabási and Albert, 1999; Newman et al., 2001). Each constituent neuron is a vertex in the network, and its connections are dubbed edges (or links). Figure 2.1A provides a schematic of connectivity but does not accurately depict the topology of vertices and edges.

<u>Erdős-Rényi</u>

Each vertex is connected with equal probability p to any of the other $n–1$ vertices in the network (Newman et al., 2001). Figure 2.1A (right, top) shows a cartoon diagram of an example of an undirected Erdős-Rényi network. However in our case the synaptic connection among neurons are directed; hence p is also the directed connection probability.

<u>Scale free</u>

The degree (number of connections a vertex possesses, in or out) distribution for all vertices follows a power law. Scale-free networks feature hubs, i.e., vertices that are very highly connected compared to the rest. We generated scale-free networks using the Barabási-Albert preferential attachment model (Barabási and Albert, 1999). Figure 2.1A (right, middle) shows a cartoon diagram of an undirected scale-free network.

<u>Small world</u>

The characteristic path length L (i.e., the smallest number of edges separating any two vertices in the network, averaged over all such pairs) grows proportionally with the logarithm of the size of the network n, i.e., $L \propto \log(n)$. This characteristic path length in small-world networks is significantly shorter compared to lattice networks (non-random regular networks where each node connects to all of its nearest neighbors) with the same level of clustering. We generated small-world networks using a random rewiring procedure from the initial lattice network where each neuron connects to exactly 20 other neurons

within the network (Watts and Strogatz, 1998). Figure 2.1A (right, bottom) shows
a cartoon diagram of a small-world network.

The connectivity from Dbx1 preBötC interneurons to reticular premotor neurons
is also unknown. In the situations where the reticular network is modeled as
scale-free or small-world, the preBötC is connected to the reticular network via
an anti-preferential attachment model in order to balance the synaptic level for
premotor neurons. We computed a weighted connection probability p_{ij} between
preBötC neuron i and reticular premotor neuron j given by

$$p_{ij} = p_{baseline} * \frac{average\ in-degree\ of\ all\ premotor\ neurons}{in-degree\ of\ premotor\ neuron\ j}\ ,$$

where $p_{baseline}$ is 0.175.

2.2.3 Numerical methods

We simulated network models on the SciClone computing cluster at the College
of William and Mary. We employed a 4th-order Runge-Kutta numerical integration
routine with a fixed time step of 0.25 ms using NeuronetExperimenter software
(http://neuronetexp.sourceforge.net/) to simulate large populations of neurons
with arbitrary connectivity. Network models were subjected to 100 random
neuron deletions from either preBötC or reticular formation in order to measure
the amplitude and frequency of respiratory-related network output, and then
compare it to experimental results (Wang et al., 2014; Revill et al., 2015). One
neuron was deleted every 20 s (simulated time) by setting the synaptic gating
variable and its corresponding differential equation to zero, which disconnects
the neuron from the rest of the network. Deleted neurons then no longer
contributed to the fictive nerve output.

2.3 RESULTS

2.3.1 Ablating preBötC and reticular interneurons cause disparate effects on respiratory rhythm and motor output

Cumulative photonic destruction of Dbx1 preBötC neurons impairs and then irreversibly precludes inspiratory rhythm generation (Wang et al., 2014). The amplitude of motor output (monitored from the XII cranial nerve root *in vitro*) decreased precipitously after ablating 10-15 Dbx1 neurons; further ablations decelerated spontaneous rhythm and then stopped it altogether after destruction of ~85 Dbx1 preBötC neurons. Figure 2.2A shows a previously unpublished representative experiment from (Wang et al., 2014). Numerical simulations replicated perturbation and cessation of spontaneous rhythm when the model preBötC was subjected to cumulative random deletions (Song et al., 2015), but lacked the precipitous decrease in network output, which we postulate is because the model incorporated only the preBötC but not premotor or motor circuits.

Surmising that a more realistic model should feature reticular XII premotor circuits to properly replicate network output, we performed cell-selective photonic ablation experiments in rhythmically active slices to interrogate the role(s) of Dbx1 reticular neurons (Revill et al., 2015). The preBötC, reticular formation, and XII nuclei are bilaterally distributed in the brainstem, and that bilateral symmetry is retained in rhythmically active slices used for laser ablation experiments *in vitro* (see Funk and Greer, 2013; Wang et al., 2014; Revill et al., 2015 for details). Deleting Dbx1 reticular neurons from one side of the medullary slice preparation decreased the amplitude of the ipsilateral XII motor output linearly without

affecting frequency. Figure 2.2B shows a previously unpublished representative experiment from (Revill et al., 2015). The contralateral XII output was unaffected. In general, selective laser ablation of 97 ± 20 (mean ± SD) Dbx1 reticular neurons caused a 36 ± 4 % and 54 ± 3 % (mean ± SD) decrease in ipsilateral XII amplitude and area, respectively (Revill et al., 2015).
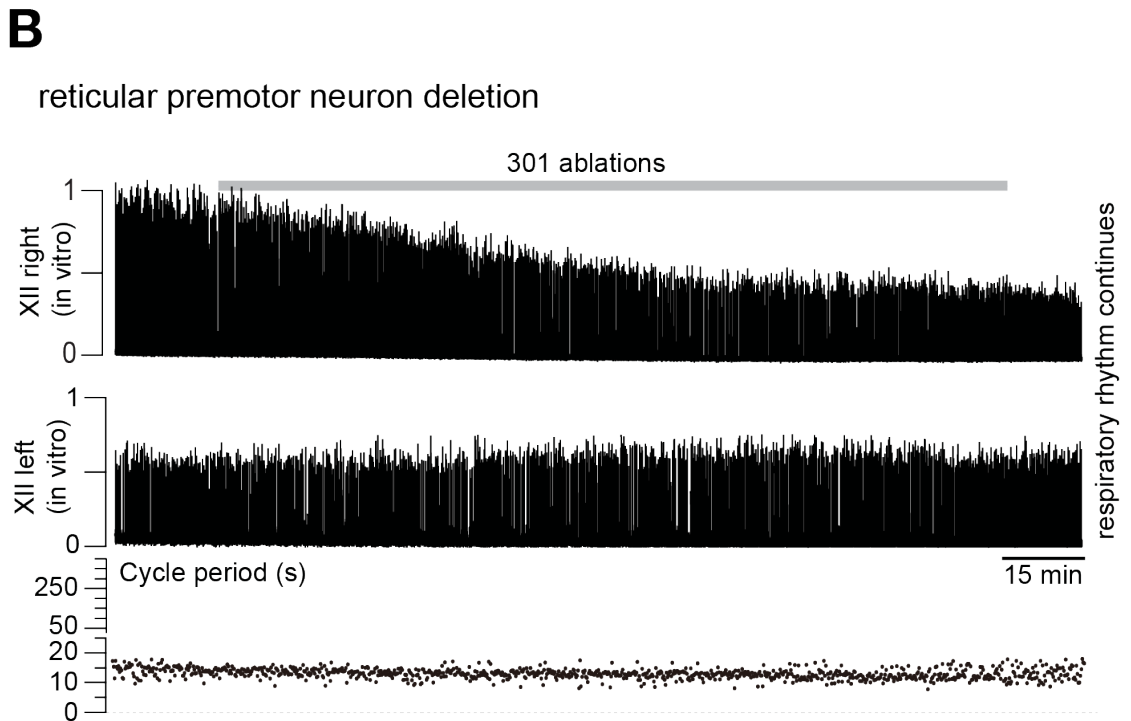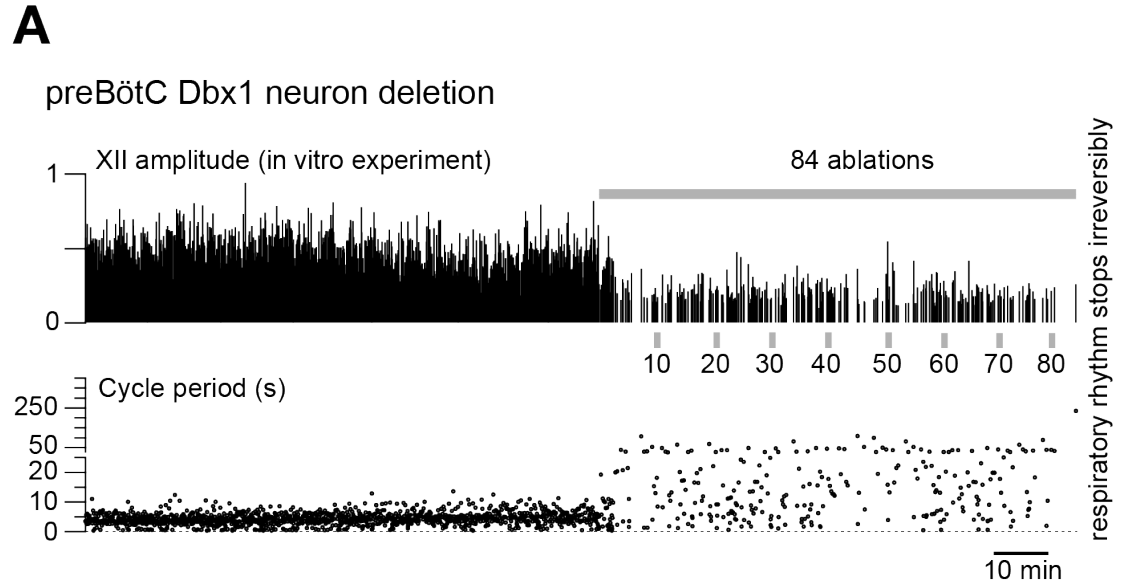
Figure 2.2. A, *In vitro* experiment showing sequential, cumulative laser ablation of

Dbx1 preBötC neurons induced precipitous decline in the inspiratory related XII motor

output, with concomitant rhythm deceleration followed by its cessation. Cell-selective

detection and laser ablation experiments in the preBötC are thoroughly documented in

the original publications (Hayes et al., 2012; Wang et al., 2013, 2014). In brief, slices

that retain the preBötC, the intermediate reticular formation, as well as the XII motor

nucleus and motor nerve root were perfused with 27 °C artificial cerebrospinal fluid at

4 ml/min and the external K^+ concentration was maintained at 9 mM. Top: normalized

amplitude of the XII motor nerve discharge (motor output) measured via suction

electrode and then amplified, full wave-rectified, and smoothed for display. The grey

bar indicates the cumulative laser-ablation phase with the total ablation tally. Bottom: a

time-series plot of respiratory cycle period measured in real time during the laser

ablation experiment. The ordinate scale is continuous, but the tick scale changes at 25

s (5-s ticks are utilized from 0 to 25 s; 50-s ticks are utilized from 26 to 400 s). Cycle

period exceeding 250 s indicates irreversible rhythm termination. **B,** *In vitro* experiment

showing sequential, cumulative Dbx1 reticular neuron laser ablations from the right

side of the slice preparation *in vitro*, which caused a linear decline in the ipsilateral

(right) XII amplitude with no concomitant perturbation of respiratory cycle period.

Methodological details can be found in the original publication (Revill et al., 2015). Top:

normalized amplitude of the right XII motor nerve rootlet. The grey bar indicates

cumulative laser-ablation phase with the total ablation tally. Middle: normalized

amplitude measured from left XII nerve rootlet. Bottom: a time-series plot of respiratory

cycle period measured in real time during the laser ablation experiment. To match Fig.

2.2A, the ordinate scale is continuous, but the tick scale changes at 25 s (5-s ticks are

utilized from 0 to 25 s; 50-s ticks are utilized from 26 to 400 s).

2.3.2 Erdős-Rényi network for the premotor population

To attempt to replicate these *in vitro* experiments *in silico*, we first set up a network such that 36% of the preBötC neurons (i.e., 90 of the 250 model Dbx1 preBötC neurons) were allowed to connect to an Erdős-Rényi reticular network (e.g., Fig. 2.1A) with a fixed probability of 0.25. Then we performed sequential random ablations from the model preBötC (Fig. 2.3).

The first model Dbx1 preBötC neuron deletion was performed at 30 s (simulated time); a large portion of the XII premotor population started spiking tonically, which elevated the baseline of the running-time spike histogram. This running-time spike histogram encodes the firing patterns of all premotor neurons projecting to XII motoneurons, and thus it represents the model analog of XII nerve output recordings, which we dubbed 'fictive nerve output' (Figs. 2.3-2.5). The running-time spike histogram incorporates 50 preBötC neurons projecting to XII motoneurons (population A in Fig. 2.1A) and the 100 reticular premotor neurons (population D in Fig. 2.1A) and implicitly assumes that the XII motoneuron output is a linear readout of its constituent inputs. The tonic-spiking pattern in fictive nerve output (Fig. 2.3) was maintained throughout the simulation regardless of the ablation tally. Therefore, showing only the first four ablations suffices to demonstrate the outcome of the experiment. Here, the connectivity of the preBötC and reticular formation, as well as the connectivity within the reticular population itself, are independent. Reticular XII premotor neurons cannot generate rhythmic activity alone, but rather entrain to rhythmic input from the preBötC. Therefore, as preBötC neurons are deleted, the reticular premotor neurons to which they project lose rhythmic synaptic drive but connectivity

among reticular neurons remains unchanged. These premotor neurons, which

have lost preBötC drive, cease to burst in sync with the preBötC but may engage

in recurrent excitation with other reticular neurons and spike tonically.

Nine other simulations of the same network configuration showed qualitatively

similar results (not shown). These data suggest that an Erdős-Rényi network is

not a realistic model for the reticular premotor circuit because the outcome of *in*

silico experiments (Fig. 2.3) did not match the corresponding *in vitro* experiments

(Fig. 2.2A as well as Wang et al., 2014) particularly with respect to the amplitude

of motor output.

Figure 2.3. Simulated random deletion of preBötC neurons wherein the reticular

premotor system is modeled as an Erdős-Rényi network. Top: raster plot of 50

preBötC neurons (index 1-50) and 100 premotor neurons that project to the XII

nucleus (index 51-150). Simulation lasts 100 s in total. The grey bar indicates the

cumulative laser-ablation phase with the total ablation tally. Each dot on the raster plot

corresponds to a spike in a single neuron. Bottom: running-time spike histogram

(spks/ms) computed from the raster plot.

2.3.3 Scale-free network for the XII premotor population

Configuring the XII premotor population as a scale-free network (e.g., Fig. 2.1A)

results in a large standard deviation of the in-degree distribution (in-degree

ranged from 22.9 to 77.0, with SD of 14.2, N = 50 networks) compared to that of

the Erdős-Rényi premotor population (in-degree ranged from 22.4 to 45.9, with

SD of 4.7, N = 50 networks). Nevertheless, high-in-degree vertices are sparse,

so the overall network connectivity remained commensurate with the parameter

sets identified in Fig. 2.1B. Each premotor neuron in a scale-free reticular

network received approximately the same number of synapses as in the Erdős-

Rényi configuration (median in-degree measured 33.2 for the scale-free

configuration and 33.5 for the Erdős-Rényi configuration).

We implemented an anti-preferential attachment rule (see "Network model

consisting of the preBötC and intermediate reticular formation" in Materials and

Methods) when connecting preBötC neurons to the reticular premotor network;

i.e., more interconnections with other reticular premotor neurons reduce the

likelihood of input from the preBötC, and vice versa. Then, preBötC neurons

were randomly and cumulatively ablated from the model system (Fig. 2.4A).

Approximately half of the reticular premotor network stopped discharging bursts

after the ninth deletion, which is qualitatively similar to the experimental results

(see Fig. 2.2A). Forty-one out of 100 simulations of different realizations of the

same network configuration showed qualitatively similar results (not shown), in

which 7.3 ± 6.3 (mean ± SD) neuron deletions would induce the precipitous

amplitude decline while 34.2 ± 7.8 (mean ± SD) neuron deletions led to rhythm termination. The other 59 simulations showed no qualitative change in the fictive nerve output as the growing ablation tally slowed and stopped the rhythm.

A

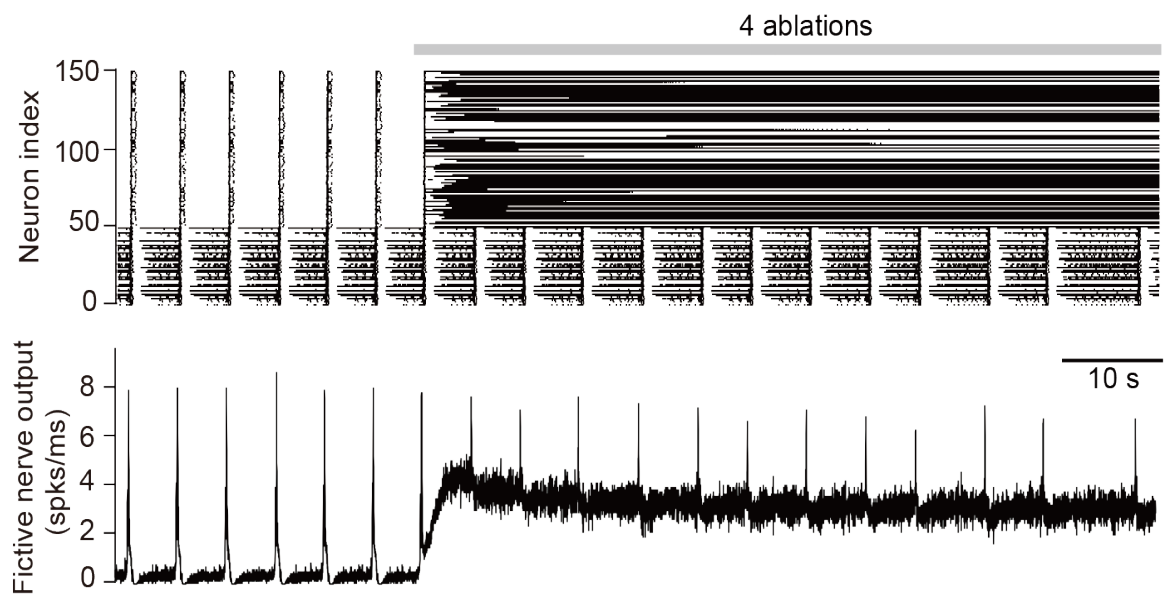preBötC Dbx1 neuron deletion

B
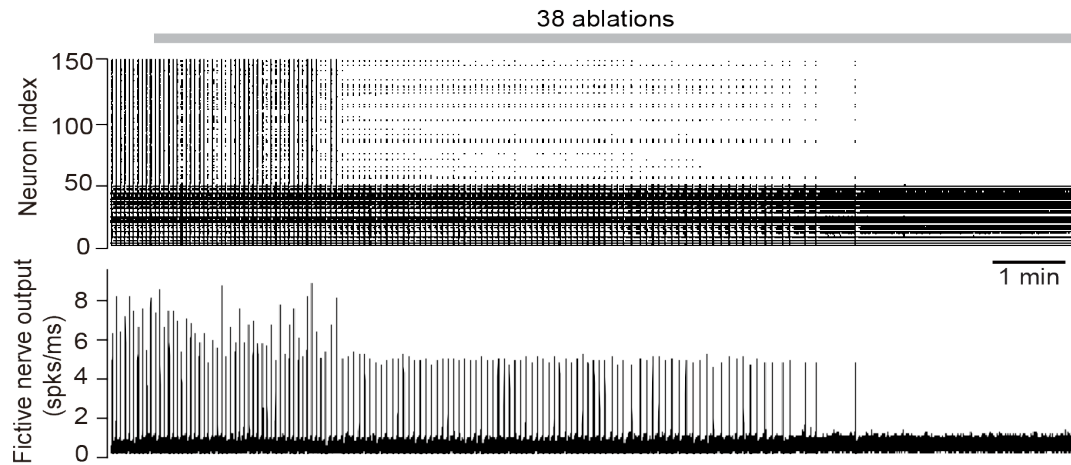
reticular premotor neuron deletion

Figure 2.4. A, Simulated random deletion of preBötC neurons wherein the reticular

premotor system is modeled as a scale-free network. **B,** Simulated random deletion of

reticular premotor neurons from a scale-free network configuration. Top: raster plot of

50 preBötC neurons (index 1-50) and 100 premotor neurons that directly project to the

XII nucleus (index 51-150). Simulation lasts 800 s in total. The grey bar indicates the

cumulative laser-ablation phase with the total ablation tally. Each dot on the raster plot

corresponds to a spike in a single neuron. Bottom: running-time spike histogram

(spks/ms) computed from the raster plot.

To further test the scale-free reticular network configuration, we randomly and

cumulatively deleted XII premotor neurons matching the experiment in Fig. 2.2B

($N = 50$). Fictive nerve output dropped initially and then stabilized (Fig. 2.4B)

instead of decreasing linearly throughout the ablation sequence, which differed

from the experimental result (see Fig. 2.2B). These data suggest that a scale-

free network captures some, but not all, features of a realistic model for the

reticular premotor circuit.

2.3.4 Small-world network for the XII premotor population

We sought to remodel the reticular premotor system while preserving

connectivity commensurate with the Erdős-Rényi-like premotor network (to

ensure synchronized activity in XII premotor neurons, see Fig. 2.1B) as well as

the anti-preferential attachment rule to connect the preBötC neurons with the

reticular premotor network (which successfully replicated the amplitude drop in

response to preBötC neuron ablation, see Figs. 2.2A and 2.4A).

Scale-free networks feature highly connected 'hub' vertices whose deletion can

cause abrupt changes in function such as catastrophic system failure (Barabási

and Albert, 1999; Newman et al., 2001). We reasoned that hubs are unlikely to

exist in the Dbx1 reticular premotor network because our cumulative ablation experiments *in vitro* never failed catastrophically (see Fig. 2.2B and Revill et al., 2015). If hubs exist in the real system, it seems unlikely that we would have failed to delete one in the context of hundreds of ablations randomly targeting Dbx1 reticular neurons performed *in vitro*. We have also implemented the anti-preferential attachment interconnection on a Erdős-Rényi-like premotor network and performed the preBötC neuron ablations, where almost all reticular premotor neurons end up spiking tonically (not shown, n = 10).

Therefore, we re-assembled the reticular premotor system as a small-world network (e.g., Fig. 2.1A). The in-degree ranged from 28.3 to 40.3, with SD of 2.4, and the median in-degree measured 34.0, which is similar to the in-degree distribution and the median in-degree of the Erdős-Rényi and scale-free network configurations. We again connected the preBötC to the reticular premotor network via anti-preferential attachment.

We randomly deleted model Dbx1 preBötC neurons and monitored fictive nerve output (Fig. 2.5A). The rhythm decelerated and terminated after a tally of 47 total ablations (the simulation reached a final tally of 53 but rhythm cessation occurred at 47); fictive nerve output experienced a precipitous drop in amplitude after the 13th deletion. These results broadly matched the experiments (see Fig. 2.2A and Wang et al., 2014). When we randomly deleted model Dbx1 neurons from the reticular premotor population instead, output decreased linearly to a steady-state level of attenuation without perturbing rhythmic frequency (Fig. 2.5B), which was

also consistent with the Dbx1 reticular premotor neuron laser ablation

experiments (see Fig. 2.2B and Revill et al., 2015).

A

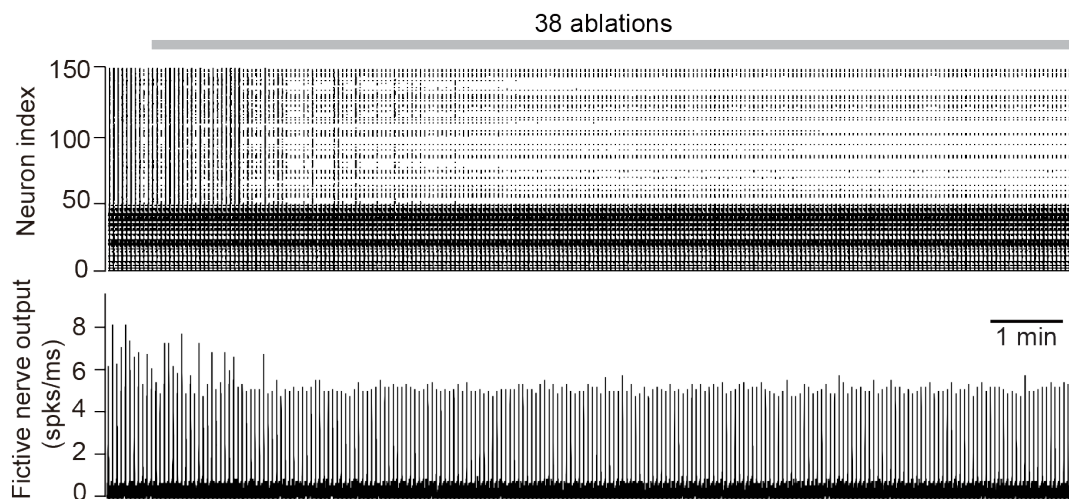preBötC Dbx1 neuron deletion

B

reticular premotor neuron deletion
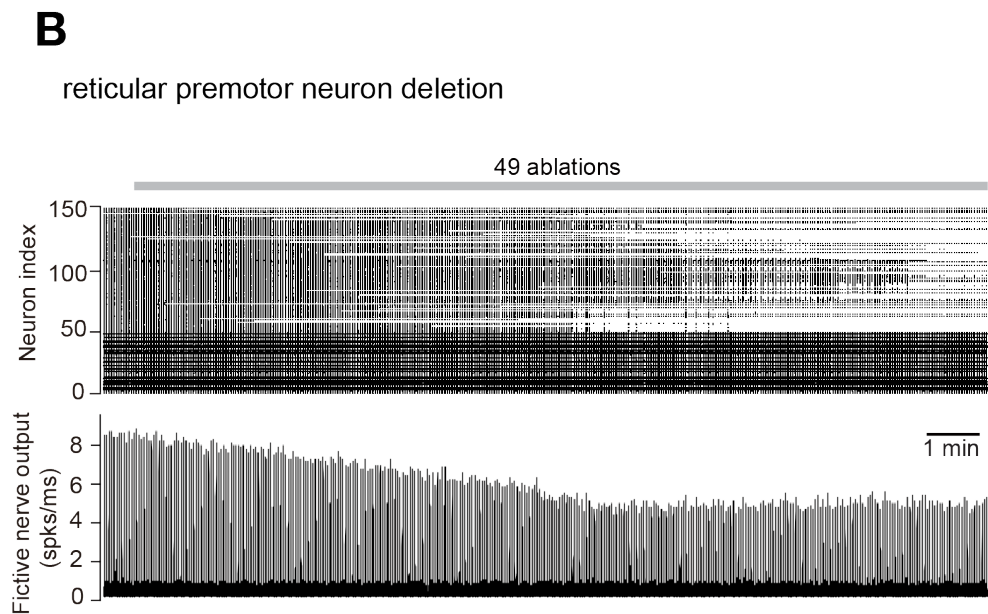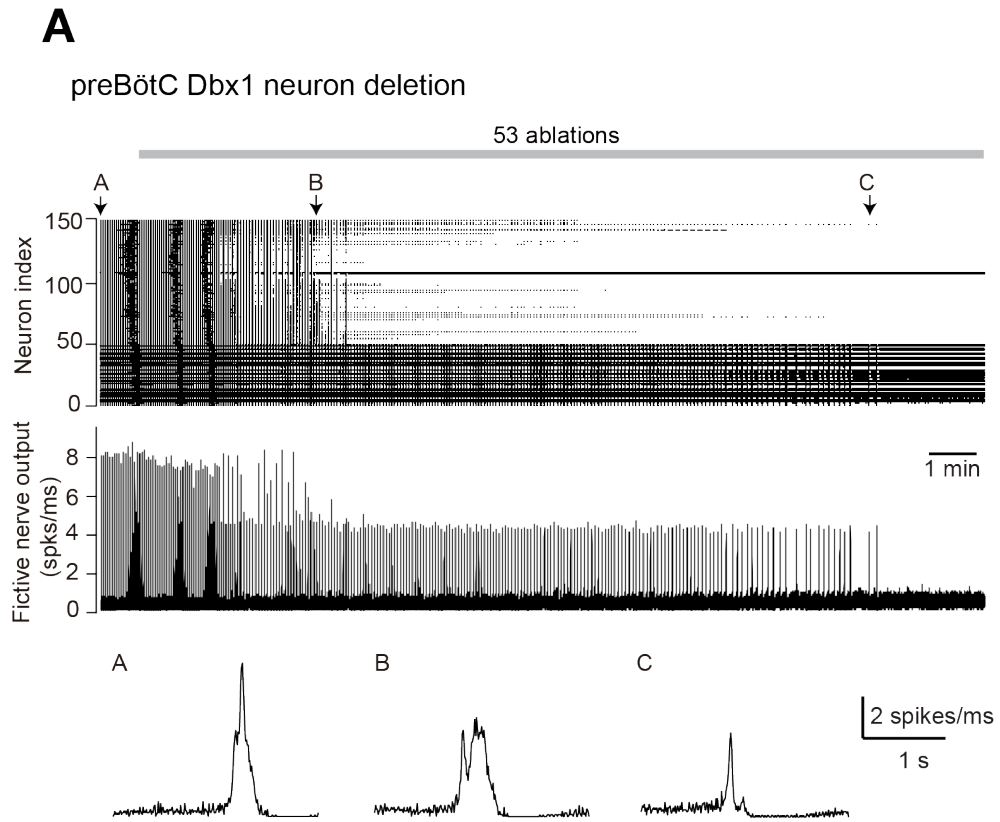
Figure 2.5. A, Simulated random deletion of preBötC neurons wherein the reticular

premotor system is modeled as a small-world network with fictive nerve outputs for

three individual network-wide bursts indicated by A, B and C (indicated above the

raster plot) at different stages of the simulated experiment. **B,** Simulated random

deletion of reticular premotor neurons from a small-world network configuration. Top:

raster plot of 50 preBötC neurons (index 1-50) and 100 premotor neurons that directly

project to the XII nucleus (index 51-150). Simulation lasts 1000 s in total. The grey bar

indicates the cumulative laser-ablation phase with the total ablation tally. Each dot on

the raster plot corresponds to a spike in a single neuron.

In a total of 150 different realizations of the reticular premotor network in a small-

world configuration, our simulations accurately reproduced the effects of preBötC

neuron ablations in 38 cases (25.3% of 150 simulations, 95% CI is 18 to 32%),

which is far from the majority of cases. However, the ability to accurately

reproduce the reticular ablation experiment was much greater. In a total of 50

realizations of the reticular premotor network in a small-world configuration, we

successfully replicated the results of Dbx1 reticular neuron ablations in 42 cases

(84% of 50 simulations, 95% CI is 74 to 94%). These data suggest the viability of

a small-world network to model the real reticular premotor system, but

furthermore suggest that the precipitous drop in output following Dbx1 preBötC

neuron ablation depends on additional factors that were not accurately captured

in our simulations. Since the model preBötC neurons follow three qualitatively

different coupling schemes (see populations A, B, and C in Fig. 2.1A), we

speculated that a precipitous output-drop, which invariably resulted from ablation

experiments *in vitro* (Fig. 2.2A and Wang et al., 2014), might depend on which

certain subset of Dbx1 preBötC neurons are targeted for ablation.

To address this, we conducted three sets of preBötC neuron deletion simulations. Each set was repeated 50 times. Each run continued for 1030 simulated sec (50 neuron deletions, one every 20 sec after a 30 sec initialization phase) and employed the same group of 50 network realizations referenced above. Only the random deletion sequence that targeted a specific subset of preBötC neurons changed in each case.

In the first case, we randomly deleted 50 neurons from among the 200 of the Dbx1 preBötC neurons that had no direct connection to the XII nucleus (sets B and C in Fig. 2.1A). For the second case, we specifically targeted the 50 Dbx1 preBötC neurons that connected to the XII nucleus (set A in Fig. 2.1A). For the third simulation, we selectively targeted 50 neurons from among the 90 Dbx1 preBötC neurons (set B in Fig. 2.1A, 36% of 250 preBötC neurons) that connected to the reticular premotor population (set D in Fig. 2.1A). The fictive nerve output showed four characteristic patterns (Fig. 2.6): 1) lack of function, i.e., no network-wide bursts; 2) stable amplitude for the duration of the simulation; 3) tonic spiking in the premotor network after a certain number of ablations, causing a shift in the baseline amplitude (e.g., see Fig. 2.3 for a simulation with that type of output); and 4) precipitous amplitude drops after a number of neuron deletions (see Figs. 2.2A, 2.4A, and 2.5A, as well as Wang et al., 2014 for illustrations of this behavior).
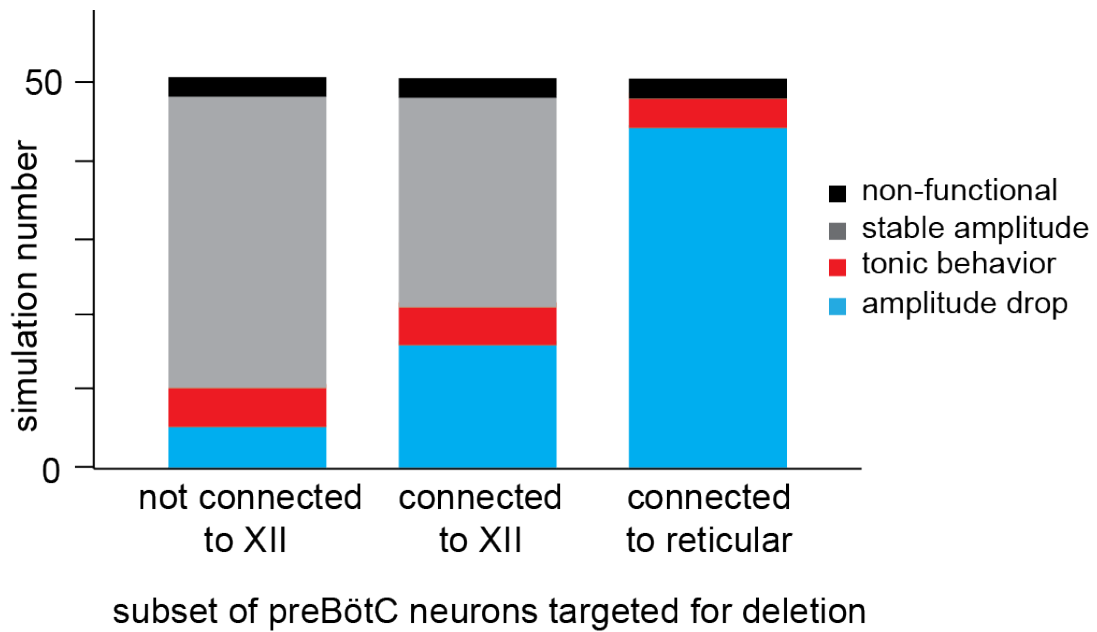
Figure 2.6. Deletion sequence analysis performed on 50 separate trials of cumulative ablation of model preBötC neurons. For three deletion strategies (horizontal axis), 50 simulations were conducted on the same group of 50 realizations of the same configuration for both the preBötC and a small-world reticular premotor network. Each simulation result falls into one of four possible outcomes, represented in different colors. Black: non-functional, i.e., the network never achieves a network-wide burst. Gray: stable amplitude, i.e., no precipitous decline in the output amplitude before rhythm termination. Red: tonic behavior, i.e., a large portion of premotor neurons spikes tonically after several preBötC neuron deletions. Cyan: precipitous amplitude drop, i.e., the rhythmic amplitude precipitously declined after a few neuron deletions.

Of the four patterns described above, only the fourth matches the *in vitro* targeted Dbx1 preBötC neuron laser-ablation experiments (see Fig. 2.2A and Wang et al., 2014). We categorized output patterns 1, 2, and 3 collectively as unsuccessful and output pattern 4 as successful. Five out of 50 simulations (10%) were successful in the first set of simulations, 16 simulations (32%) were successful in the second group, and 42 simulations (84%) were successful in the

third group. These results indicate that the third strategy, which targeted Dbx1

preBötC neurons that project to reticular premotor neurons (set B, Fig. 2.1A),

caused a precipitous drop in the fictive nerve output amplitude more often than

the other two strategies. Assuming the null hypothesis that all strategies would

be equally effective, we performed a Chi-Square test to analyze the results

$(\mathcal{X}^2 = 59.28, p < 0.00001)$. If targeting strategy has no impact on how the fictive

nerve output responds to cumulative ablation, then a result such as this would be

extremely unlikely to occur by chance, which bolsters our confidence that

targeting strategy is an important factor that influences the precipitous drop in

network output characteristic of the *in vitro* laser ablation experiments.

2.4 DISCUSSION

We developed laser ablation methodology with real-time physiological monitoring

to quantify the cellular parameters of respiratory rhythm- and pattern-generating

circuits (Hayes et al., 2012; Wang et al., 2013). Cumulative deletion of Dbx1

preBötC interneurons slowed and then stopped respiratory rhythm. Surprisingly,

the magnitude of inspiratory motor output declined precipitously before the 15th

neuron deletion. By contrast, laser ablation of Dbx1 reticular neurons decreased

motor output linearly without affecting frequency. Here we present a plausible

model that replicates these experiments and thus provides testable predictions

regarding the configuration of rhythmogenic and XII premotor circuits.

The performance of this network system depends on the choice of the Rubin-

Hayes model for preBötC and reticular premotor neurons. This model

incorporates the two major burst-generating inward charge carriers, INa-P and

I_{CAN}, as well as excitatory synaptic connections. However, synaptically triggered intracellular Ca^{2+} dynamics coupled to I_{CAN} activation, which motivated the development of the Rubin-Hayes model, have been challenged by studies that perturbed metabotropic receptors and intracellular Ca^{2+} release without stopping rhythmogenesis (Beltran-Parrazal et al., 2012; Ben-Mabrouk et al., 2012). These results do not invalidate the model because Rubin-Hayes recapitulates recurrent excitation dynamics that all respiratory neurobiologists agree is essential for rhythmogesis (Funk et al., 1993; Wallén-Mackenzie et al., 2006; Carroll and Ramirez, 2013; Carroll et al., 2013); recurrent excitation also underlies another influential and contemporary model of respiratory rhythmogenesis (Guerrier et al., 2015). Furthermore, excitatory synapses evoke subthreshold Ca^{2+} accumulation in the Rubin-Hayes model via an agnostic mechanism not explicitly wedded to metabotropic receptors or intracellular Ca^{2+} release. Two-photon Ca^{2+} imaging in preBötC neurons dialyzed intracellularly with QX-314 demonstrate postsynaptic Ca^{2+} accumulation during inspiratory phases that does not depend on Na+ spiking (Del Negro et al., 2011). Therefore, synaptically triggered subthreshold Ca^{2+} increases occur via an unknown mechanism whose dynamics are codified in the Rubin-Hayes model.

We have modeled the preBötC rhythmogenic core as an Erdős-Rényi network (Wang et al., 2014; Song et al., 2015). Several preBötC modeling studies employed all-to-all connectivity (Butera et al., 1999; Purvis et al., 2007; Jasinski et al., 2013), which is not realistic: paired recordings in the preBötC showed that the excitatory synapses between putative rhythm generators are sparse

(approximately 13%, Rekling et al., 2000). In contrast, Guerrier et al. (2015) constructed a random geometric network in which a synaptic connection from one neuron to another is exponentially proportional to the distance between them. The Guerrier model creates a far too robust preBötC whose rhythmic function stops after 44% of constituent neurons are deleted, whereas inspiratory rhythms in vitro and in our Erdős-Rényi model of the preBötC cease after ~15% of the constituent neurons are ablated (Hayes et al., 2012; Wang et al., 2014; Song et al., 2015).

We created 100 reticular premotor neurons, initially coupled in Erdős-Rényi configuration, which showed that network-wide synchronization depends on approximately 90 out of 250 preBötC neurons projecting to premotor neurons with a connection probability of $p = 0.175$. This last parameter served as a baseline connection probability when we reconfigured the reticular premotor system as scale-free or small-world networks. Comparing laser ablation simulations to their corresponding experimental benchmarks provided testable insights into the structure and function of the real system.

2.4.1 Reticular premotor network configurations

We compared three network configurations for the XII premotor population. The Erdős-Rényi premotor network synchronized well, but did not replicate Dbx1 preBötC neuron ablation experiments. Deleting a model preBötC neuron diminishes rhythmic drive to the Erdős-Rényi premotor network, but its local connectivity has no relationship to preBötC input. So the premotor circuit may still

undergo recurrent excitation, which leads to tonic spiking instead of rhythmic bursts in sync with the preBötC.

We surmised that connectivity between the preBötC and the reticular premotor system – and connectivity within the reticular population – cannot be independent. Alternative connectivity schemes should counterbalance synaptic input from reticular premotor neurons with synaptic drive from preBötC neurons.

We then modeled the XII premotor population as a scale-free network. The anti-preferential attachment rule ensures that each XII premotor neuron receives proportional synaptic drive from both preBötC and premotor populations. It self-adjusts to maintain a fixed (total) level of synaptic input and is an important testable prediction for future studies.

Subsequently deleting model preBötC neurons predominantly affects XII premotor partners that receive fewer inputs from within the reticular network. Accordingly, XII premotor neurons that receive input from the preBötC are not connected richly enough within the reticular formation to promote recurrent excitation, which might otherwise lead to tonic spiking and induce the rest of the XII premotor population to spike tonically as well. By virtue of their relatively sparse connectivity within the reticular formation, these XII premotor neurons likely receive input from other remaining preBötC neurons and thus may continue to burst in sync with the preBötC, albeit with lower burst magnitude. Therefore, cumulatively deleting model preBötC neurons causes reticular premotor neurons to either burst with lower amplitude or go silent.

The scale-free premotor network configuration accurately replicated the Dbx1 preBötC neuron ablation experiments, but its output did not decline linearly in response to reticular neuron ablations, which occurred in every Dbx1 reticular neuron laser-ablation experiment.

We re-modeled the XII premotor population as a small-world network, rich in local connections yet short in average path length, with anti-preferential attachment connectivity from the preBötC. This configuration generated a precipitous decline in the fictive nerve output in the case of cumulative preBötC neuron deletions. Because each reticular premotor neuron in the small-world network contributes commensurately to the network output, cumulatively deleting reticular neurons diminishes the fictive nerve output linearly as the ablation tally increases, consistent with the experiments (Revill et al., 2015). Our XII premotor population model comports with neuroanatomical evidence that some reticular formation networks are small-world (Achard et al., 2006; Bassett and Bullmore, 2006; Humphries et al., 2006).

Guerrier et al. (2015) demonstrated that synaptic dynamics (including facilitation and depression) can influence network behavior in ways that may override topological features. Could a disparity in synaptic dynamics, rather than network topology, explain the differential effects of laser ablation of Dbx1 preBötC versus Dbx1 reticular premotor neurons? Dbx1 preBötC neurons express synaptic properties predicted by Guerrier (Kottick and Del Negro, 2015), but similar information about excitatory synapses among Dbx1 reticular premotor neurons is not yet available. Nonetheless, Dbx1 reticular premotor neurons have a lower

level of excitability compared to Dbx1 preBötC neurons (Revill et al., 2015) and thus we modeled them as such. Without knowledge regarding synaptic disparity between preBötC and reticular premotor neurons, we favor a topological explanation for the differential effects of laser ablation.

2.4.2 Implications for respiratory rhythmogenic circuitry

With a small-world reticular premotor network and anti-preferential attachment from the preBötC, preBötC-neuron deletions caused a precipitous decline in the fictive nerve output in ~25% of simulations (which occurred in 100% of the experiments). However, if we selectively targeted preBötC neurons directly connected to premotor neurons, then a precipitous decline in fictive nerve output occurred 84% of the time. Furthermore, when we examined all the simulations we found that a precipitous decline in the fictive nerve output occurred by random chance whenever the deletion sequence contained a substantial fraction of preBötC neurons with direct connections to the reticular premotor system. This analysis suggests we preferentially photo-ablated Dbx1 preBötC neurons directly connected to the XII premotor network. The most parsimonious explanation would be that Dbx1 preBötC neurons that connect to reticular premotor neurons are concentrated at the rostral face of the preBötC, which is exposed by transverse slice preparations (Hayes et al., 2012; Wang et al., 2013, 2014). Laser ablation experiments would be predisposed to ablate these reticular-projecting neurons rather than other Dbx1 preBötC interneurons with only local connections. We cannot be sure that Dbx1 local-only preBötC interneurons are more prevalent at depth in the preBötC, but the evidence for XII

premotor neurons at the rostral edge of the preBötC is strong. For example,

premotor neurons for tongue protruder muscles are located in the area

immediately rostral to and within the preBötC (Dobbins and Feldman, 1994).

Dbx1 neurons at the rostral-dorsal border of the preBötC project to the reticular

formation (Picardo et al., 2013; Revill et al., 2015), and physiological transection

and pharmacological studies attribute premotor function to the rostral edge of

preBötC (Funk et al., 1993; Ruangkittisakul et al., 2014).

This study provides a framework for analysis of the respiratory rhythm- and

pattern-generating circuits underlying breathing. An important prediction is the

anti-preferential connections from the preBötC to the small-world reticular

formation. This could arise due to activity-dependent synaptic elimination (Flavell,

2006; Yogev and Shen, 2014) because an overabundance of synapses and

neurons is commonplace during development (Cowan et al., 1984; O'Donovan,

1999). Analogous to our model assembly, the embryonic reticular formation may

form a small-world network. Then, as preBötC synapses connect to reticular

neurons, synapses are pruned to balance the excitation among reticular neurons

and preBötC inputs during 'fetal breathing' (Kobayashi et al., 2001). This

effectively may account for how an anti-preferential attachment rule emerges in

the real system.

CHAPTER 3. "Next generation" cellular model of rhythmogenic preBötC neurons

3.1 INTRODUCTION

Inspiratory breathing movements, which are a fundamental aspect of respiration, originate due to neural rhythms from the preBötzinger complex (preBötC) in the ventral medulla. Efforts to understand the neural origins of breathing have employed *in vivo* and *in vitro* experimental studies, but *in silico* modeling studies have also provided an important contribution during the last few decades. The last two chapters of research focused on network modeling to understand the structure and function of the preBötC as well as interactions between the preBötC and the adjacent population of respiratory-related hypoglossal premotor neurons. In constructing the network models, we adopted the well-established Rubin-Hayes model (Rubin et al., 2009). This model has provided a framework for analyzing respiratory rhythm and motor pattern. However, it is not without its limitations. The Rubin-Hayes model was formulated such that biophysical mechanisms were abstract rather than explicitly modeled by physiologically realistic equations, which has been problematic in terms of evaluating and testing the cellular and ionic mechanisms of rhythm generation experimentally. Furthermore, the Rubin-Hayes model was designed to simulate typical breathing (i.e., eupnea) but respiratory behaviors also include sighs (augmented breaths that occur periodically and can be triggered by emotional stimuli) as well as gasping under pathological and hypoxic conditions, which Rubin-Hayes does not accommodate. For these reasons, we sought to consolidate some of the successes of Rubin-Hayes, then adopt successful aspects of other contemporary

models, and thus synthesize and develop a new canonical model of a

rhythmogenic preBötC interneuron at a more realistic and informative level.

Hence in this study, by reviewing the history of respiratory neurobiological

modeling and comparing the advantages of a few symbolic models, we aim to

construct a cellular model, which, with the original Rubin-Hayes model as

foundation, is more biophysically realistic and makes testable predictions to

guide experimental protocols. This iterative process, we contend, will lead to

refinement of the model and ultimately advance understanding of respiratory

rhythm generation in mammals.

3.1.1 Chain-of-inhibition model and birth of the pacemaker hypothesis

Some of the first modeling studies of mammalian respiration date back to 1970s

and '80s. Von Euler and colleagues proposed a central pattern generator (CPG)

model for breathing that consisted of inhibitory and excitatory interneurons in a

recurrent loop (von Euler, 1983). However, experimental limitations at the time

precluded an unambiguous test of the model. All cell-recording experiments were

performed on heavily barbiturate-anesthetized animals (generally cats), which

drastically enhanced chloride-mediated synaptic inhibition and thus

overemphasized the role of synaptic inhibition. In addition, it was impossible to

systematically manipulate or perturb rhythm-generating circuits in the whole-

animal context.

The ability to interrogate respiratory rhythmogenic circuits was greatly advanced

by the advent of *in vitro* preparations, which retained respiratory active circuits *ex

vivo* and thus exposed the brainstem and spinal cord for electrophysiological

recordings as well as ionic and pharmacological manipulations (Suzue, 1984; Smith et al., 1990). Using isolated brainstem-spinal cords, so-called *en bloc* preparations, Feldman and Smith (Feldman and Smith, 1989) tested the von Euler model by substituting large impermeant anions for chloride ions in the bathing solution. This manipulation abolished chloride-mediated synaptic inhibition, which the model necessitated, and yet respiratory rhythm generation *in vitro* continued with no change in frequency (Feldman and Smith, 1989). Having falsified the von Euler scheme (at least *in vitro*), these results gave credence to the idea that specialized pacemaker neurons could be the basis for respiratory rhythmogenesis (Feldman and Cleland, 1982). However, this idea of pacemaker-driven respiratory rhythm was highly speculative at first because there was no existing data regarding autorhythmic respiratory-related neurons and, furthermore, the site of rhythm-generation was still not known.

3.1.2 preBötzinger complex and voltage-dependent pacemaker neurons

The next major watershed study reported the discovery of the preBötC in 1991. This anatomically and functionally specialized site was first identified by serial transection experiments in *en bloc* preparations, which demonstrated that the preBötC was necessary and sufficient for rhythmogenesis *in vitro* (Smith et al., 1991). Furthermore, that study established that *en bloc* preparations could be further reduced such that ~500-μm-thick transverse medullary slices containing the preBötC, as well as premotor and respiratory-related hypoglossal (XII) motoneurons, could generate robust respiratory-related oscillations and motor output *in vitro*. These rhythmically active slices were experimentally

advantageous because they exposed the preBötC and thus enabled intracellular

recordings from putatively rhythmogenic preBötC interneurons in the context of

breathing-related rhythms and motor output *in vitro*.

Interneurons with voltage-dependent pacemaker-like properties were recorded

and characterized within preBötC. These putative respiratory pacemakers could

generate alternating cycles consisting of bursts of action potentials followed by

periods of quiescence if their baseline membrane potential was within -60 to -50

mV. Smith et al. proposed that these interneurons could be specialized for

respiratory rhythm generation, a theory that was dubbed the *pacemaker*

hypothesis of rhythmogenesis, or simply the *pacemaker hypothesis*.

Henceforth, the pacemaker hypothesis became a viable explanation for

respiratory rhythm generation. The modeling of the pacemaker hypothesis

advanced greatly in 1999, when Butera et al. proposed a cellular model in which

voltage-dependent bursting-pacemaker behavior in preBötC neurons arises due

to the fast activation and slow inactivation of persistent Na$^+$ current (I_{Na-P}) (Butera

et al., 1999). The Butera model, based on a Hodgkin-Huxley equations for the

major charge carriers, provided two key experimentally testable predictions: first,

that respiratory frequency should depend on the voltage-dependence of

activation for I_{NaP}, and second that inspiratory burst duration (i.e., burst

termination) should be linked to voltage-dependent slow inactivation of I_{Na-P}.

Although I_{Na-P} was the central ionic mechanism underlying the Butera model, it

had not been measured or quantified. The existence of I_{Na-P} was inferred from

extracellular recordings of pacemaker-like activity in medullary neurons (including,

but not limited to, those in the preBötC) in a bathing solution with lowered Ca^{2+}, which precludes pacemaker-like activity due to voltage-gated Ca^{2+} currents (Johnson et al., 1994).

Later in 2002, I_{Na-P} was measured via a series of ramp depolarization voltage-clamp experiments (Del Negro et al., 2002a), making it possible to begin quantitatively modeling the current. To further characterize the biophysics of Na^+ currents by quantifying the amplitude as well as the activation and inactivation, Ptak et al. (2005) applied a train of high-frequency (25 Hz) voltage pulses to preBötC neurons and then found that both I_{Na-F} and I_{Na-P} were reduced in amplitude by the equivalent amount, hence deducing that both types of whole-cell Na^+ current were generated by the same population of Na^+ channels (Ptak et al., 2005). Their analyses provided a unified Na^+ channel model that could account for both transient (fast) Na^+ current (I_{Na-F}) and $I_{Na-P.}$

The underlying idea that I_{Na-F} and I_{Na-P} are not separate channels *per se* was also indicated by Taddese and Bean (Taddese and Bean, 2002) who showed that I_{Na-P} was likely to originate from incomplete inactivation (0.5 – 4% at steady-state) of the total Na^+ conductance as well as modal gating schemes in conventional Na^+ channels (Alzheimer et al., 1993; Bennett et al., 1995).

Nevertheless, I_{Na-P} was not the sole ionic mechanism that could give rise to bursting-pacemaker activity in the preBötC. Ca^{2+}-activated non-specific cation current (I_{CAN}) was discovered as an excitatory inward current that could also contribute to pacemaker-like bursting in a subset of preBötC neurons (Thoby-Brisson and Ramirez, 2001). At first this report appeared to bolster the

pacemaker hypothesis because it showed that more than one ionic mechanism could drive authorhythmic cellular behaviors in the preBötC. However, the pacemaker hypothesis gradually fell out of favor because pharmacological antagonists such as riluzole that targets I_{Na-P} (Doble, 1996; Urbani and Belluzzi, 2000) and flufenamic acid that targets I_{CAN} (Guinamard et al., 2013) could be applied to block I_{CAN} and I_{Na-P} and yet neither blocker would abolish rhythmogenesis except when co-applied at extreme concentrations that induce with multiple side effects of the drugs (Del Negro et al., 2002b, 2005; Peña et al., 2004). The pharmacological experiments were generally inconsistent with an obligatory role for pacemaker-like preBötC neurons in rhythmogenesis, and emphasized the viability of rhythmogenesis due to network properties (Grillner, 2006; Grillner and Jessell, 2009).

3.1.3 Group pacemaker hypothesis and recurrent excitation

Even though pacemaker-like preBötC neurons are highly unlikely to be rhythmogenic, the two inward currents I_{CAN} and I_{Na-P} are ubiquitously expressed in preBötC neurons, regardless of whether those neurons exhibit pacemaker-like activity (Crowder et al., 2007; Pace et al., 2007a, 2007b). Building on a speculative notion first proposed by Rekling, and then articulated by an influential review by Rekling and Feldman (Rekling and Feldman, 1998), our laboratory formulated the idea that I_{CAN} might augment burst generation in a network consisting of excitatory neurons with synaptic connections among them. Consistent with that mechanism, excitatory synaptic transmission has been

acknowledged as an essential property for rhythmogenesis (Funk et al., 1993; Wallén-Mackenzie et al., 2006).

As alluded to above, the group pacemaker hypothesis proposed that recurrent excitation was essential, such that respiratory rhythm generation is a network property that emerged from the recurrent interactions among these neurons instead of an individual cellular property (Rekling and Feldman, 1998). An explicit mathematical model of the group pacemaker was established in 2009; rhythmic inspiratory bursts were only possible in that model when synaptic transmission was coupled to activation of I_{CAN} (Rubin et al., 2009). The Rubin-Hayes model illustrated rhythm generation that did not rely on a voltage-dependent 'pacemaker' current such as I_{Na-P}, but rather the recurrent synaptic excitation among neurons coupled to burst-generating post-synaptic currents like I_{CAN}.

Nonetheless, I_{Na-P} is ubiquitously expressed in the preBötC, so the Rubin-Hayes model was modified later to include both I_{Na-P} and I_{CAN} (Dunmyre et al., 2011). The group-pacemaker model was widely applied in a series of network studies including not only the rhythmogenic populations within the preBötC but also the premotor neurons located in the intermediate reticular formation (Wang et al., 2014; Song et al., 2015, 2016) but its veracity as a model of rhythm generation *per se* has still not been fully evaluated.

3.1.4 Pacemaker-like models with more biophysical realism

In parallel with models of the group-pacemaker mechanism (Rubin et al., 2009; Dunmyre et al., 2011) an alternative pacemaker-like model of preBötC neurons in 2011, inspired by Thoby-Brisson and Ramirez (2001) and their identification of

I_{Na-P} and I_{CAN}-mediated bursting neurons, introduced two types of independent

bursting modules incorporated into one cell (Toporikova and Butera, 2011). In

this two-compartment model of a preBötC neuron, the voltage-dependent

activation and inactivation of I_{Na-P} acted as the mechanism for bursting in the

somatic compartment while the dendritic compartment formed rhythmic bursts as

a result of Ca^{2+}-related oscillations and I_{CAN}. This Toporikova-Butera model

featured electrotonic coupling between somatic and dendritic compartments so

that their oscillations could be synchronized. Jasinski and colleagues (2013) then

modified Toporikova-Butera by combining these compartments into a single-

compartment. The cellular pacemaker-like activity of the Jasinski model does not

solely depend on I_{Na-P} or Ca^{2+} related oscillations and I_{CAN}. Blocking either ionic

mechanism does not fully abolish the bursting rhythm of the cell (Jasinski et al.,

2013). The Jasinski model also featured a detailed Ca^{2+} material-balance system

including a Calcium-induced-Calcium-release (CICR) subsystem modeling the

Ca^{2+} exchange between cytosol and erdoplasmic reticulum (ER), an inositol

(1,4,5)-trisphosphate (IP_3)-mediated intracellular Ca^{2+} releasing pathway, and a

high-voltage activated (HVA) Ca^{2+} channel (Jasinski et al., 2013). The Jasinski

model was a significant advance because it introduced biophysical realism into

preBötC modeling, yet it was at the same time atavistic because by nature it was

still a pacemaker-like model, the rationale of which is questionable since no

existing data support the obligatory role of pacemaker neurons in respiratory

rhythm generation, no putative 'pacemakers' have ever been recorded *in vivo*,

and considerable data from *in vitro* experiments argue against the pacemaker hypothesis and strongly favor network mechanisms of rhythm generation. While the models by Toporikova, Butera, and Jasinski et al. provide a detailed description of intracellular Ca^{2+} dynamics, the role of the IP_3-mediated intracellular Ca^{2+} release was questioned by several contemporary studies that attenuated or blocked CICR mechanisms but did not significantly perturb respiratory bursts and rhythms (Beltran-Parrazal et al., 2012; Ben-Mabrouk et al., 2012). We surmise from these studies that intracellular Ca^{2+} dynamics (CICR mainly) and I_{CAN} activation might serve as a 'safety factor', which enhances the robustness of inspiratory bursts without being obligatory for rhythmogenesis. This idea that a large I_{CAN}-mediated burst is not rhythmogenic does not solely come from the CICR-related experiments summarized above but is also consistent with the burstlet hypothesis proferred by Kam and Feldman (Kam et al., 2013b), which proposed that when a preBötC burst occurred, its high amplitude inspiratory component was always preceded by a pre-inspiratory subthrehold activity that resembled a burstlet. This last particular point was a crucial one in our present work, because we included I_{CAN}, akin to Rubin-Hayes, but de-emphasized its central role and importance in light of these data from 2012, as well as our own ongoing experiments (Picardo, Dorst, Guinamard, and Del Negro, unpublished 2016).

3.1.5 Burst termination: the role of pumps and synaptic depression
The understanding of mechanisms contributing to burst termination has developed continuously since the original Rubin-Hayes model was proposed in

2009. It was suggested that Na^+, as the dominant inward charge carrier for the inspiratory bursts mediated by I_{CAN}, would accumulate during the inspiratory burst and in turn recruit the electrogenic Na/K ATPase pump to produce the outward current, I_{pump}, aiding in the burst termination. The possible role of I_{pump} in burst termination was experimentally investigated by quantifying its amplitude during arbitrary-waveform voltage-clamp experiments. preBötC neurons were clamped at E_K at the end of a simulated inspiratory burst, which thus precluded K^+ currents, and enabled the investigators to measure the contribution of I_{pump} by pharmacological subtraction (Del Negro et al., 2009). The authors showed that I_{pump} consisted of a dynamic component exceeding 400 pA, which was present at the termination of the burst phase and then significantly decayed within 25-100 ms, as well as a tonic component measuring approximately 100 pA which might only contribute to maintaining the resting membrane potential and thus influencing the network excitability by virtue of being relevant in all preBötC neurons (Del Negro et al., 2009).

Aside from the Na/K ATPase pump, modeling and experimental studies have identified the role of short-term synaptic depression in inspiratory burst termination as well as the inspiratory-expiratory phase transition (Kottick and Del Negro, 2015). The synaptic depression was first a theoretical idea embedded in Rubin-Hayes, which was modeled abstractly using a synaptic gating variable such that synaptic depression was induced by a depolarization block of spiking during the burst phase, stopping further Ca^{2+} influx and diminishing the remaining spikes in the burst, therefore contributing to burst termination (Rubin et al., 2009).

Aiming to provide a model for synaptic dynamics in rhythmogenesis with more biophysical realism, Guerrier et al. later proposed a detailed model to describe the interactions of pools of synaptic vesicles (readily releasable and recycling, respectively) as well as a recovering state, and their effects on the release of neurotransmitters between presynaptic and postsynaptic preBötC neurons. The Guerrier et al. model, which was otherwise simple and generic in its modeling of somatic electrical properties, could to a great extent, account for synaptic facilitation and recurrent excitation as the burst initiation mechanism, and synaptic depression due to the limited number of docking sites for synaptic vesicles as the burst termination mechanism (Guerrier et al., 2015).

3.1.6 The 'next generation' preBötC neuron model: objectives and directions

By comparing and synthesizing the modeling studies on the rhythmogenic neurons within the preBötC, the cellular model this study proposes includes a unified Na^+ channel that exhibits both fast and persistent Na^+ current, an HVA voltage-dependent Ca^{2+} current which influences cellular excitability and I_{CAN} activation, a realistic I_{CAN} that is essential for generating augmented sigh-like bursts, a Na/K ATPase pump as one of the burst-terminating mechanisms in conjunction with and a glutamatergic synapse-driven recurrent excitation model – with synaptic facilitation for burst initiation and synaptic depression for burst termination – similar to Guerrier et al.'s model. This synthesized cellular model, when coupled in a rudimentary network model suitable for bifurcation and other analyses related to nonlinear dynamics, can account for most experimental results regarding respiratory rhythmogenesis and therefore provides new insights

and testable predictions to direct future experimental investigations of respiratory rhythm- and pattern-generating circuitry.

3.2 MATERIALS AND METHODS

3.2.1 Model description

The cellular model included in the present study features Hodgkin-Huxley-type spiking currents with 6 additional currents: calcium-activated non-specific cation current (I_{CAN}) (Crowder et al., 2007; Pace et al., 2007a; Mironov, 2008, 2013; Pace and Del Negro, 2008; Rubin et al., 2009; Mironov and Skorova, 2011), unified Na^+ current combining I_{Na-F} and I_{Na-P} (I_{Na}) (Ptak et al., 2005), excitatory synaptic current (I_{syn}) (Guerrier et al., 2015; Kottick and Del Negro, 2015), Na/K ATPase pump current (I_{pump}) (Del Negro et al., 2009; Rubin et al., 2009; Krey et al., 2010), voltage-dependent Ca^{2+} current (I_{Ca}) (Toporikova and Butera, 2011; Jasinski et al., 2013), and Na^+ and K^+ leakage currents.

The current balance equation takes the form:

$$C\frac{dV}{dt} = -I_{leak}(V,Na) - I_{Na}(V,h,Na) - I_K(V,n) - I_{CAN}(V,Ca) - I_{syn}(V,r)$$

$$-I_{Ca}(V,m_{Ca},h_{Ca},Ca) - I_{pump}(Na)$$

where

$$m(V) = 1 / \left(1 + \exp\left(\frac{V-\theta_m}{\sigma_m}\right)\right)$$

$$\frac{ds}{dt} = (s_\infty(V) - s)/T_s(V), \text{ in which } s = \{h,n,m_{Ca},h_{Ca}\}$$

$$\frac{dCa}{dt} = -\alpha_{Ca} \cdot I_{Ca}(V,m_{Ca},h_{Ca},Ca) - Ca/\tau_{Ca}$$

$$\frac{dNa}{dt} = \alpha_{Na}(-I_{CAN}(V,Ca) - I_{pump}(Na) - rate_{Na} \cdot I_{Na}(v,h,Na))$$

$$\frac{dr}{dt} = \alpha_r \cdot glut(V, y_{dock}) \cdot (1-r) - \beta_r \cdot r$$

$$\frac{dx}{dt} = \frac{(XP-x)}{\tau_f} + k_x \cdot (1-x) \cdot H(V - \theta_V)$$

$$\frac{dy_{free}}{dt} = \frac{(1 - y_{free} - y_{dock})}{\tau_{rec}} - \frac{1}{\tau_{dock}} \cdot (y_{dock_{max}} - y_{dock}) \cdot y_{free} \cdot \left(1 + \left(\frac{x - XP}{XP} \cdot H(V - \theta_V)\right)\right)$$

$$\frac{dy_{dock}}{dt} = \frac{y_{dock_{max}} - y_{dock}}{\tau_{dock}} \cdot y_{free} \cdot \left(1 + \left(\frac{x - XP}{XP} \cdot H(V - \theta_V)\right)\right) - \left(\left(\frac{1}{\tau_{rel}}\right) \cdot y_{dock} \cdot \left(\frac{x - XP}{XP}\right)\right) \cdot H(V - \theta_V)$$

describe the dynamics of the state variables for each s in $\{h, n, m_{Ca}, h_{Ca}\}$;

intracellular Ca^{2+} concentration, Ca; the activation of Na^+ channel m, Na^+

concentration, Na; AMPA receptor-mediated ionotropic synaptic gating variable, r;

synaptic facilitation variable x; the fraction of synaptic vesicles in the recycling

pool (RP), y_{free}; and the fraction of synaptic vesicles in the readily releasable

pool (RRP), y_{dock} (Fig. 3.1).

It is also worth mentioning that the activation of Na^+ current is now modeled

using the steady-state equation instead of an ODE in the Rubin Hayes model for

the reason that the time constant for the activation of Na^+ current was measured

10% of that for the inactivation (Ptak et al., 2005).

The synaptic dynamics are slightly modified from that in the Guerrier et al.'s

study (Guerrier et al., 2015) such that we added a synaptic gating variable r,

which is modeled for AMPA receptor-mediated synaptic transmission onto a

postsynaptic neuron. The synaptic facilitation variable x governs all possible

mechanisms regarding vesicular release with *XP* being its equilibrium and τ_f its facilitation rate. The heavyside function *H* determines if the membrane potential is above the spike threshold θ_V. For each presynaptic bouton, synaptic vesicles are divided into two pools and one recovering stage: RP, RRP and recovering stage, satisfying the conservation equation $y_{free} + y_{dock} + y_{rec} = 1$. Synaptic vesicles are modeled using mass-action equations, modeling the exchanges among different pools. y_{free} depends on vesicles in the recovering stage with the time constant τ_{rec}. On the other hand, at rate τ_{dock}, the flux of vesicles to the RRP is limited by the available sites $y_{dock_{max}} - y_{dock}$ where $y_{dock_{max}}$ is the maximal number of sites in the RRP. Synaptic vesicles in the RRP are available to be released as neurotransmitters at rate τ_{rel}.
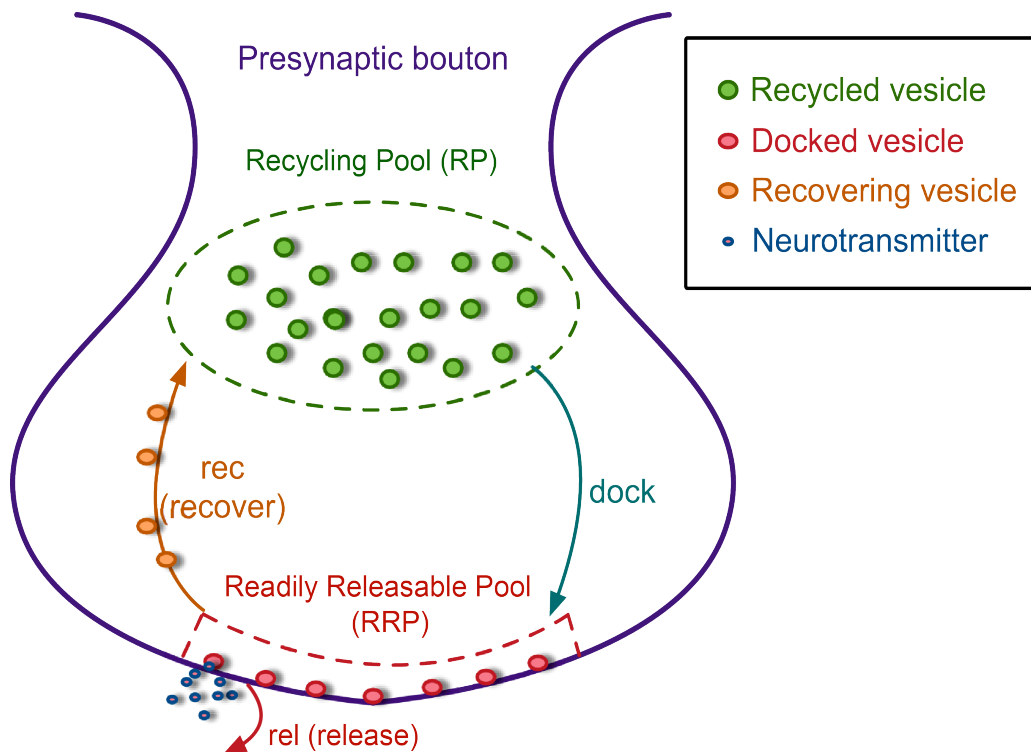
Figure 3.1. Schematic diagram of synaptic dynamics. Vesicles are divided into two pools: a recycling pool (RP, green) and a readily releasable pool (RRP, red), as well as one stage where vesicles are recovering ("rec", yellow). Vesicles in the RRP, after release, recover via mass action kinetics into the RP (yellow arrow). Vesicles in the RP proceed to dock in the RRP (cyan arrow). Vesicles in the RRP are available to release (red arrow) neurotransmitters (blue circles), which in this model represents excitatory transmitter glutamate as is required in the preBötC for respiratory rhythmogenesis.

Whole-cell currents are modeled with chord-conductance equations, in some circumstances modified or adopted from previous established rhythmogenic neuronal models (Ptak et al., 2005; Rubin et al., 2009; Toporikova and Butera, 2011; Jasinski et al., 2013; Guerrier et al., 2015):

$$I_{leak}(V,Na) = g_{kl} \cdot (V - E_K) + g_{nal} \cdot (V - E_{Na}(Na))$$

$$I_{Na}(v,h,Na) = g_{na} \cdot m^3(V) \cdot h \cdot (V - E_{Na}(Na))$$

$$I_K(V,n) = g_K \cdot n^4 \cdot (V - E_K)$$

$$I_{syn}(V,r) = g_{syn} \cdot r \cdot (V - E_{syn})$$

$$I_{Ca}(V,m_{Ca},h_{Ca},Ca) = g_{Ca} \cdot m_{Ca} \cdot h_{Ca} \cdot (V - E_{Ca}(Ca))$$

$$I_{CAN}(V,Ca) = g_{CAN} \cdot (V - E_{CAN}) / \left(1 + \exp\left(\frac{Ca - k_{CAN}}{\sigma_{CAN}}\right)\right)$$

$$I_{pump}(Na) = r_{pump} \cdot \left(\frac{Na^3}{Na^3 + k_{Na}^3} - \frac{Na_{base}^3}{Na_{base}^3 + k_{Na}^3}\right).$$

The remaining functions including voltage-dependent channel gating are:

$$s_\infty(V) = 1 / \left(1 + \exp\left(\frac{V - \theta_s}{\sigma_s}\right)\right) \text{ for each s in } \{n, m_{Ca}, h_{Ca}\}$$

$$T_n(V) = T_{n_{max}} / \cosh\left(\frac{V - \theta_n}{2\sigma_n}\right)$$

$$h_\infty(V) = (1 - nap_{ss}) / \left(1 + \exp\left(\frac{V - \theta_h}{\sigma_h}\right) + nap_{ss}\right)$$

$$T_h(V) = \exp(V \cdot h_{slow}) + 1$$

$$glut(V, y_{dock}) = y_{dock} \cdot H(V - \theta_V)$$

$$E_{Na}(Na) = 26.54 \cdot \ln\left(\frac{120}{Na}\right)$$

$$E_{Ca}(Ca) = 13.27 \cdot \ln\left(\frac{4}{Ca}\right).$$

Parameters are set to the following values for the model:

$C = 45\ pF, g_{kl} = 2.84\ nS, g_{nal} = -61.46\ mV, g_{Na} = 114\ nS, E_K = -74\ mV,$

$g_K = 40\ nS, g_{CAN} = 1\ nS, V_{CAN} = 0\ mV, k_{CAN} = 0.9\ \mu M, E_{CAN} = 0\ mV,$

$g_{syn} = 0.55\ nS, E_{syn} = 0\ mV, \theta_m = -36\ mV, \sigma_m = -8.5\ mV, T_{m_{max}} = 1\ ms,$

$\theta_h = -30\ mV, \sigma_h = 5\ mV, T_{h_{max}} = 15\ ms, \theta_n = -15\ mV, \sigma_n = -4.5\ mV,$

$T_{n_{max}} = 40\ ms, \theta_{mCa} = -35\ mV, \sigma_{mCa} = 6\ mV, T_{mCa} = 0.5\ ms, \theta_{hCa} = -52.4\ mV,$

$\sigma_{hCa} = -5.2\ mV, T_{hCa} = 100\ ms, rate_{Na} = 0.1, nap_{ss} = 0.015, h_{slow} = -0.06,$

$\alpha_{Ca} = 0.025\ \mu M \cdot pA^{-1} \cdot ms^{-1}, \theta_{CAN} = 0.9\ \mu M, \sigma_{CAN} = -0.05\ \mu M, k_s = 1,$

$Na_{base} = 5\ mM, \tau_{Ca} = 500\ ms, \alpha_r = 4, \beta_r = 0.05, y_{dock_{max}} = 0.2,$

$\alpha = 6.6 \times 10^{-5}\ mM \cdot pA^{-1} \cdot ms^{-1}, r_{pump} = 400\ pA, k_{Na} = 10\ mM, \tau_f = 700\ ms,$

$\theta_V = -20\ mV, XP = 0.3, \tau_{rel} = 47\ ms, \tau_{rec} = 3000\ ms, \tau_{dock} = 1000\ ms.$

3.2.2 Numerical simulation and analysis

We use XPPaut to conduct self-coupled simulations of our cellular model

(http://www.math.pitt.edu/~bard/xpp/xpp.html). We employed a 4th-order Runge-

Kutta numerical integration routine with a fixed time step of dt = 0.25 ms using

NeuronetExperimenter software (http://neuronetexp.sourceforge.net/) to simulate

two neurons coupled to one another.

Since a heavyside step function evaluates spike discharge, the system is

discontinuous. However, analyzing a model using bifurcation theory requires

continuity. Therefore during the bifurcation study, we use a steep sigmoidal

function to approximate the heavyside function, with the same threshold value:

$Sigm(V) = 1/(1 + \exp(-2 \cdot (V - \theta_V)))$.

To further understand the dynamics of this model, we analyzed bifurcations

associated with burst initiation and termination, using PyDStool

(http://pydstool.sourceforge.net) to locate the bifurcation points. We adopt the

fast-slow analysis pioneered by Rinzel and his colleagues as well as trainees

(Bertram et al., 1995; Rinzel and Ermentrout, 1998a) to analyze the rhythmic

activity of our model. Different time scales among the variables in a system

enable us to categorize the variables as either *fast* or *slow* (Bertram et al., 1995).

In the context of the respiratory cycle – which consists of an inspiratory burst (or

active) phase as well as an interburst interval or (*quiescent* phase) – the

oscillation of fast variables would occur rapidly during a single spike whereas the

oscillation of slow variables would occur over the duration of the entire

respiratory cycle. During cycles of respiratory activity, the evolution of the slow

variables causes the fast dynamics to alternate between quiescent and active

phases periodically. From the perspective of fast variables, slow variables can be treated as parameters so that we could analyze the bursting dynamics by studying the solution structure for the fast variables. The topology of solutions of the fast variables represents a *slow manifold*, i.e., the collection of active and quiescent states of the fast variables, which is traversed during the respiratory cycle by the evolution of the slow variables.

Specifically, to investigate the dynamics as our cellular model transitions in and out of the active (inspiratory burst) and quiescent (interburst interval) phases, it is appropriate to study the bifurcation structure of the fast-variable system, using a slow variable as a parameter whose value we exploit to explore the solution structure of the fast subsystem. In the present study, we select the slow variable Na^+ concentration as the bifurcation parameter.

3.3 RESULTS

3.3.1 Self-coupled simulation and bifurcation analysis

In the original study of the Rubin-Hayes model, intracellular Ca^{2+} concentration was the critical variable responsible for initiating inspiratory-like bursts (Rubin et al., 2009). As a minimal model of a network, which is suitable for geometric (phase plane) and bifurcation analyses, the Rubin-Hayes model was coupled to itself with an autapse (i.e., a synapse from a neuron onto itself). The basal state of the Rubin-Hayes model is tonic spiking, which triggers synaptic transmission, and elicits Ca^{2+} accumulation such that I_{CAN} activates and then generate a burst of activity. To recap, I_{CAN} is inexorably associated with inspiratory burst generation in the Rubin-Hayes model. However, in the present model, we lessen

the role of I_{CAN} so that blocking I_{CAN} altogether would not dramatically affect

normal rhythmogenesis because recent data (reviewed in 3.1 above) suggests

that I_{CAN} does not strongly activate during normal eupnea-like inspiratory bursts,

yet I_{CAN} may contribute greatly during sigh-like burst generation.

Therefore, without the same dependence on I_{CAN} for eupnea-like rhythmic

inspiratory bursts in the new model, we reasoned that Ca would not be the most

relevant slow state variable for assessing the solution structure of the model (i.e.,

acting as a bifurcation parameter in the fast-slow analysis), particularly with

regard to burst initiation. In order to determine the most relevant slow variable for

this model that acts as a slowly varying bifurcation parameter transitioning the

system in (and out) of the burst phase, we conduct self-coupled simulations,

blocking a few currents individually to investigate the influence of the currents

and their relevant state variables to the system (Fig. 3.2).

When blocking the synaptic current, the neuron goes from rhythmic bursting to

slow (~0.5 Hz) tonic spiking. This shows that synaptic current, when present,

enables tonic spiking to become bursting. Obviously, g_{syn} influences the ability to

burst because it facilitates recurrent excitation. However, because the system

itself, even in the absence of synaptic current (i.e., g_{syn} = 0 nS), is already in an

oscillatory (i.e., tonic spiking) regime, the synaptic related gating variables x,

y_{free} and y_{dock} cannot be responsible for transitions to the quiescent phase, but

instead only influence the nature of the active (bursting) phase by governing

whether it is characterized by single spikes or bursts consisting of multiple spikes

(bursts). Thus, we conclude that synapse-related state variables cannot be

suitable parameters for studying the bifurcations that underlie transitions in the respiratory cycle.

Intact model

-57 mV

$g_{syn} = 0$

-57 mV

$g_{ca} = 0$

-57 mV

$g_{CAN} = 0$

-57 mV

| 20 mV

2 s
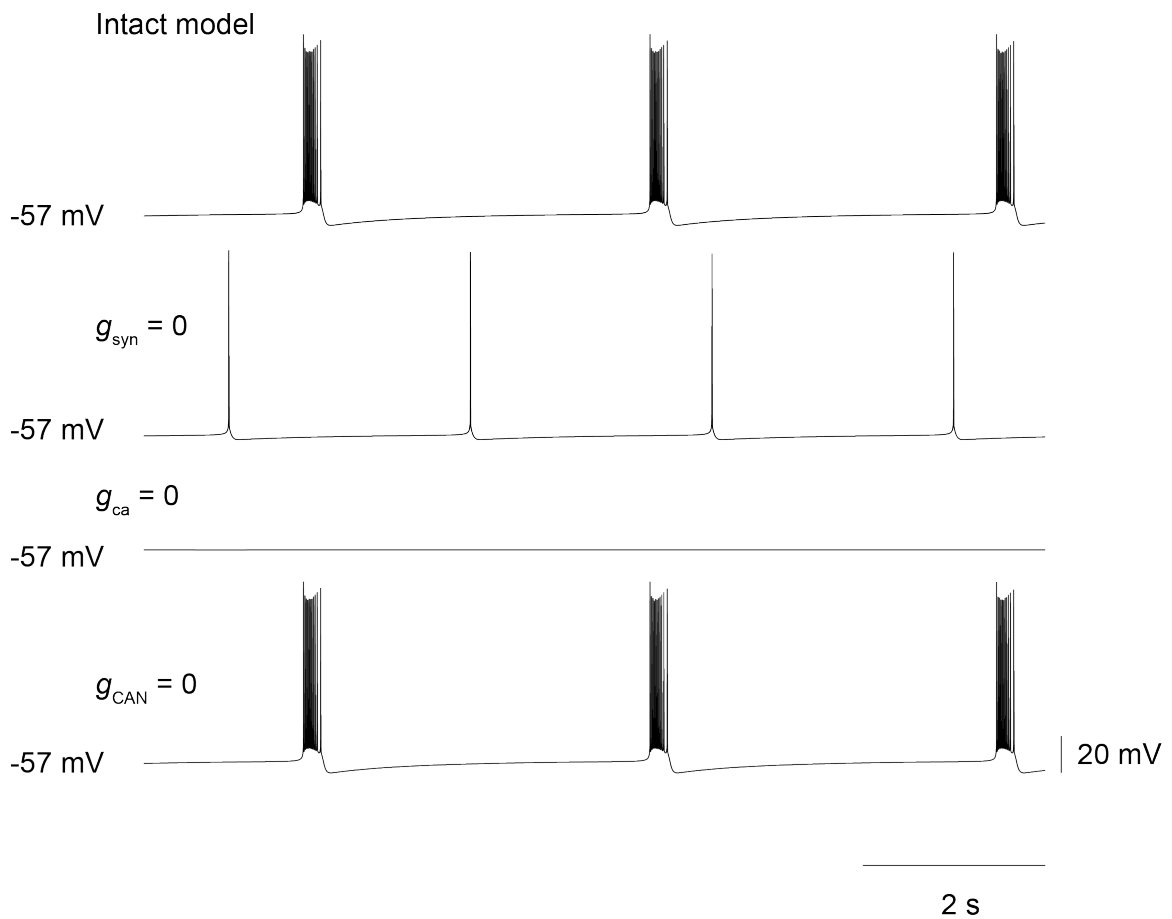
Figure 3.2. Self-coupling and individual current-blocking simulations. We couple a model neuron to itself via an autapse, and then run the simulation for 10 simulated sec (intact model). Then we repeat the simulation for three different conditions: $g_{syn} = 0$ nS (blocking synaptic current), $g_{Ca} = 0$ nS (blocking voltage-dependent Ca^{2+} current) and $g_{CAN} = 0$ nS (blocking I_{CAN}). The membrane potential trajectory is shown for each scenario. Time and voltage calibrations are shown, along with baseline membrane potential (in each trace).

Next, when we block voltage-dependent Ca^{2+} current, the neuron remains quiescent, which at first seems to satisfy the criterion for a good bifurcation parameter (i.e., it could cause the neuron to transition from the active to the

94

quiescent state). However, g_{Ca} is still not an ideal bifurcation parameter for the following reason. Akin to tonic current in the Jasinski model and leakage current in the Rubin-Hayes model, both of which govern excitability so as to induce tonic spiking (which seeds recurrent excitation during the pre-inspiratory phase), our model relies on voltage-dependent Ca^{2+} current to influence excitability and ensure tonic spiking since its fractional activation at baseline membrane potential would give rise to some minimal leakage-like current, and thus serve a similar function. Therefore blocking it would naturally put the system in quiescence. The role of voltage-dependent Ca^{2+} current in this model could be substituted by a tonic current or a lower K^+ leakage conductance (g_{kl} = 2.8 nS) that provides the system with the same control of excitability to induce tonic spiking in the absence of synaptic transmission. So we conclude that g_{Ca} or I_{Ca}-associated state variables are not ideal bifurcation parameters.

In addition, when we block I_{CAN}, neuronal bursting is not affected, further suggesting that Ca is not the slow variable we are seeking as a bifurcation parameter to study the system either.

From these current blocking simulations, we deduce that Na^+ concentration is possibly a key variable that influences respiratory cycle dynamics. In particular, it directly determines the reversal potential for Na^+, which influences both Na^+ current and Na^+ leakage current. Moreover, Na^+ concentration affects the Na/K ATPase pump current, which along with synaptic depression, acts as a burst termination mechanism (Del Negro et al., 2009; Kottick and Del Negro, 2015). Na acts as a slow variable that accumulates during the burst phase and its

increments activate the pump, which in turn pumps out (i.e., decreases) Na$^+$ and due to its inherent electrogenicity hyperpolarizes the neuron. Pump-mediated hyperpolarization terminates the burst phase and thus engenders the inter-burst interval. From the perspective of those fast variables in the system such as the glutamate gating variable r and the activation or inactivation gating variables of I_{Na}, Na then could be parameterized for us to study the system dynamics during the burst phase and burst termination. Accordingly, we used Na as a bifurcation parameter and we studied the slow manifold of solutions to the fast-variable system during the respiratory cycle (Fig. 3.3) and then delved further to compute a two-parameter bifurcation diagram with g_{syn} as an auxiliary parameter to investigate its impact on the solution structure of the fast variables traversed during a complete respiratory cycle and examine how that solution structure varied with g_{syn} (Fig. 3.4).

First we consider g_{syn} at 0.6 nS, the same synaptic strength as the example neuron model shown in Fig. 3.2, and explore the solution structure of the system of fast variables as a function of Na$^+$. Figure 3.3 shows the numerically computed bifurcation diagram (i.e., the slow manifold) and superimposes a full burst cycle in membrane potential-Na$^+$ space (i.e., V-Na space). Next we analyze how the inspiratory burst initiates and terminates. Since we are focusing on the biophysically realistic Na range of [4.8 mM, 6 mM] in this analysis, we do not shown the complete bifurcation diagram, which encompasses a wider range of Na, including values that are far beyond what is physiologically realistic. We raise this issue because in the range we show [4.8 mM, 6 mM] the bifurcation diagram

appears to have disparate branches, but in fact those branches are connected if one visualizes the entire diagram. The complete bifurcation diagram consists of a branch of stable nodes at the lowest values for membrane potential, which is connected to an unstable branch of saddle points at the left-most knee of the slow manifold (which coincides with $Na \sim 5$ mM, see Figs. 3.3 and 3.4). The branch of saddles proceeds toward increasing values of Na and then ends at a Hopf bifurcation point at $Na \sim 30$ mM. The branch created at the Hopf bifurcation returns toward (lower) realistic ranges of Na. As per a Hopf bifurcation, the branch of limit cycles encloses a node. The stability of nodes and limit cycles is not uniform throughout the branch. We have to study the stability of the entire branch and for now confine our interest to the realistic range of Na [4.8 mM, 6 mM].

We begin analyzing a respiratory cycle in the quiescent phase where the membrane potential is approximately -57 mV and Na^+ concentration is decreasing due to pump activity. In the diagram shown in Fig. 3.3, the state point would be on the lowest branch of the slow manifold, moving leftward toward the left knee of the slow manifold. When Na reaches approximately 5.05 mM, the system crosses a saddle-node (SN) bifurcation at the left knee, wherein the quiescent state disappears. The system then approaches an attracting stable limit cycle, which is the onset of spiking in the model neuron, and Na starts to increase again. In Fig. 3.3, the state point traverses the sawtooth-shape oscillations at membrane potentials between (approximately) -55 and +40 mV while generally moving rightward. Because spiking in the model generates

recurrent synaptic excitation (in this case via the autapse), the spiking

accelerates during the burst (although it is not possible to visualize that speed-up

in *V-Na* space) and the spike amplitude decreases concurrently.
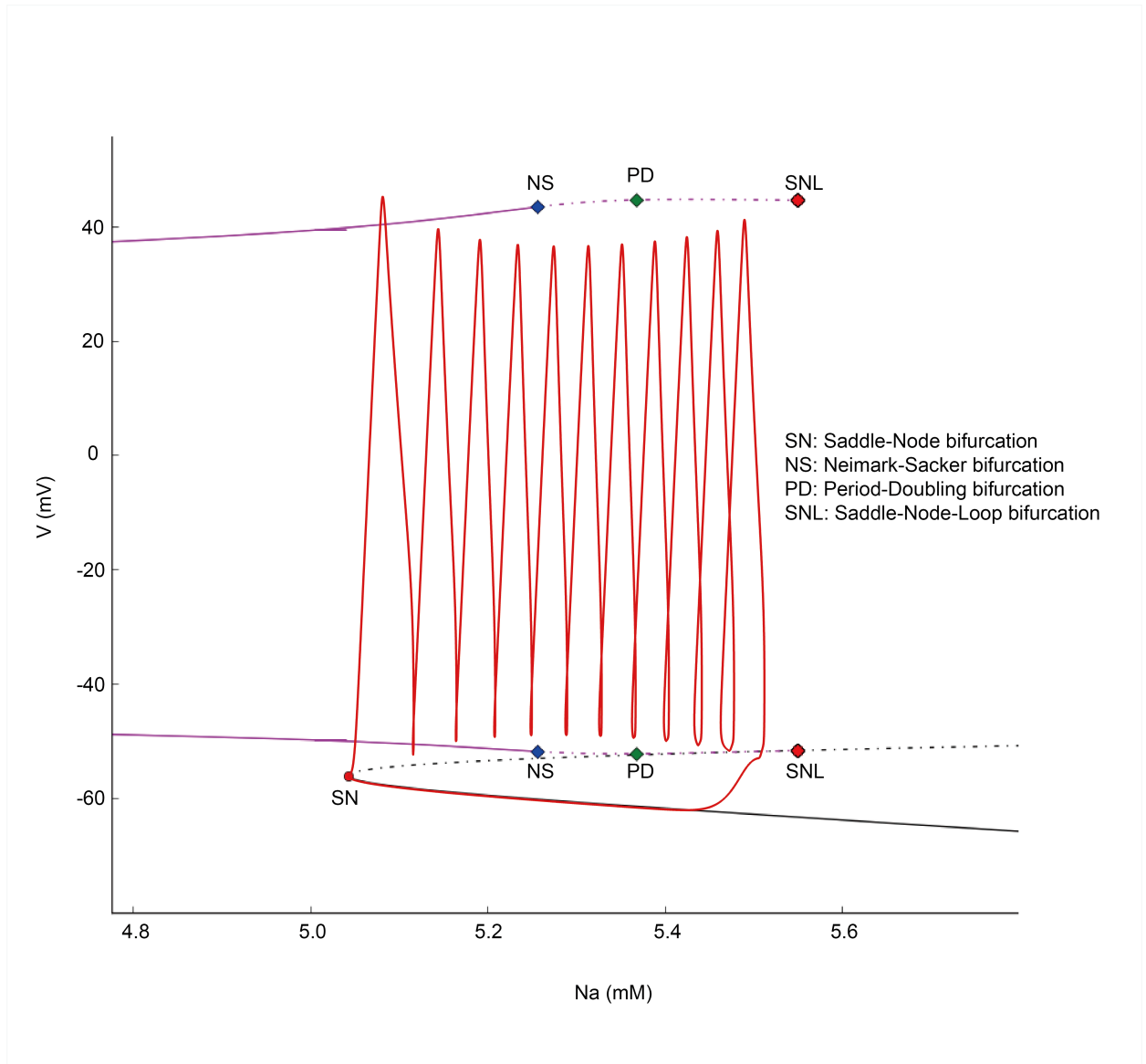
Figure 3.3. Bifurcation diagram for g_{syn} = 0.6 nS using *Na* as the bifurcation

parameter. SN, NS, PD and SNL indicate the bifurcation points or limit points. SN

refers to saddle-node bifurcation; NS refers to a Neimark-Sacker bifurcation; PD refers

to a period-doubling bifurcation; and SNL refers to saddle-node-loop bifurcation. Solid

black line indicates the stable branch of nodes; the dotted line stands for the unstable

branch of saddle points. The superimposed red trace shows the trajectory of a complete respiratory cycle. The active phase (burst) originates at the SN bifurcation point and evolves clockwise. The trace that overlays the stable branch of nodes up to the SN bifurcation represents the trajectory during the quiescent (inter-burst interval) phase. Purple lines (stable is solid and unstable is dotted) represent the maximum and minimum amplitudes of spikes in the active state.

As the burst continues, a Neimark-Sacker (NS) bifurcation occurs, that is oscillations in the state variable *Na* periodically modulate the spike (voltage) oscillation, which creates a torus. At the NS bifurcation, the limit cycle of the spike oscillation becomes unstable, and thereafter appears to be drawn to the torus, which we surmise to be weakly attracting (but the precise nature of the NS bifurcation remains to be demonstrated). Although the precise position and the stability of the torus has yet to be numerically determined, it appears to be weakly attracting because when we start a simulation using a point close to the NS bifurcation on the unstable limit cycle as the initial condition, then a train of spiking at ~20 Hz occurs for longer than 16 sec before the system transitions to the quiescent phase.

Meanwhile during the active phase, synaptic depression begins to show its effects such that the inward (depolarizing) current due to recurrent synaptic excitation is decreasing in strength, and is unable to counteract the hyperpolarizing electrogenic outward current of the Na/K ATPase pump. The contribution of the pump is most easily visible in Fig. 3.3 when *Na* passes ~5.4 mM and the hysteresis loop in *V-Na* space becomes apparent (at the nadir of each spike oscillation *Na* slightly decreases). This change in the balance of

synaptic drive (which acts to further depolarize the neuron) compared to the Na/K ATPase pump (which in contrast acts to hyperpolarize the neuron) occurs at a period-doubling (PD) bifurcation, where the limit cycle of the spike becomes strongly unstable. The net effect of the PD bifurcation is to increase the amplitude of the spike oscillation (this is clear in Fig. 3.3 as the sawtooth-like spike increases in magnitude), prolong the inter-spike interval, and cause the membrane potential to approach the unstable manifold of the saddle point (neither the prolongation of the inter-spike interval nor the manifold of the saddle are visible in the V-Na space of Fig. 3.3). Eventually Na increments cause the membrane potential to cross the unstable manifold of the saddle point, which is a separatrix, and the trajectory in the new basin of attraction evolves to the stable branch of stable nodes (at approximately -60 mV). The transition to quiescence occurs near a saddle-node-loop (SNL) bifurcation in the system ($Na \sim 5.58$ mM); the proximity to the homoclinic orbit formed at the SNL explains why the spike rate slows down after passing the PD point (Rinzel and Ermentrout, 1998b; Strogatz, 2001). During the quiescent phase (i.e., inter-burst interval) Na slowly decreases as the system follows the stable branch of nodes toward the SN bifurcation point where the next burst will initiate, restarting another active phase. This cycle repeats periodically.

To determine the effect of synaptic strength on burst initiation and termination, we then vary g_{syn} in a two-parameter bifurcation study (Fig. 3.4). Recalling the analyses from Fig. 3.3, with g_{syn} = 0.6 nS, the burst initiates at the SN and terminates just prior to the SNL. Now considering other values for g_{syn} on two-

parameter bifurcation graph in Fig. 3.4A, we can see that in the absence of synaptic transmission (g_{syn} = 0 nS), the termination point of the active phase (nominally considered to be the SNL) collides with the SN bifurcation.
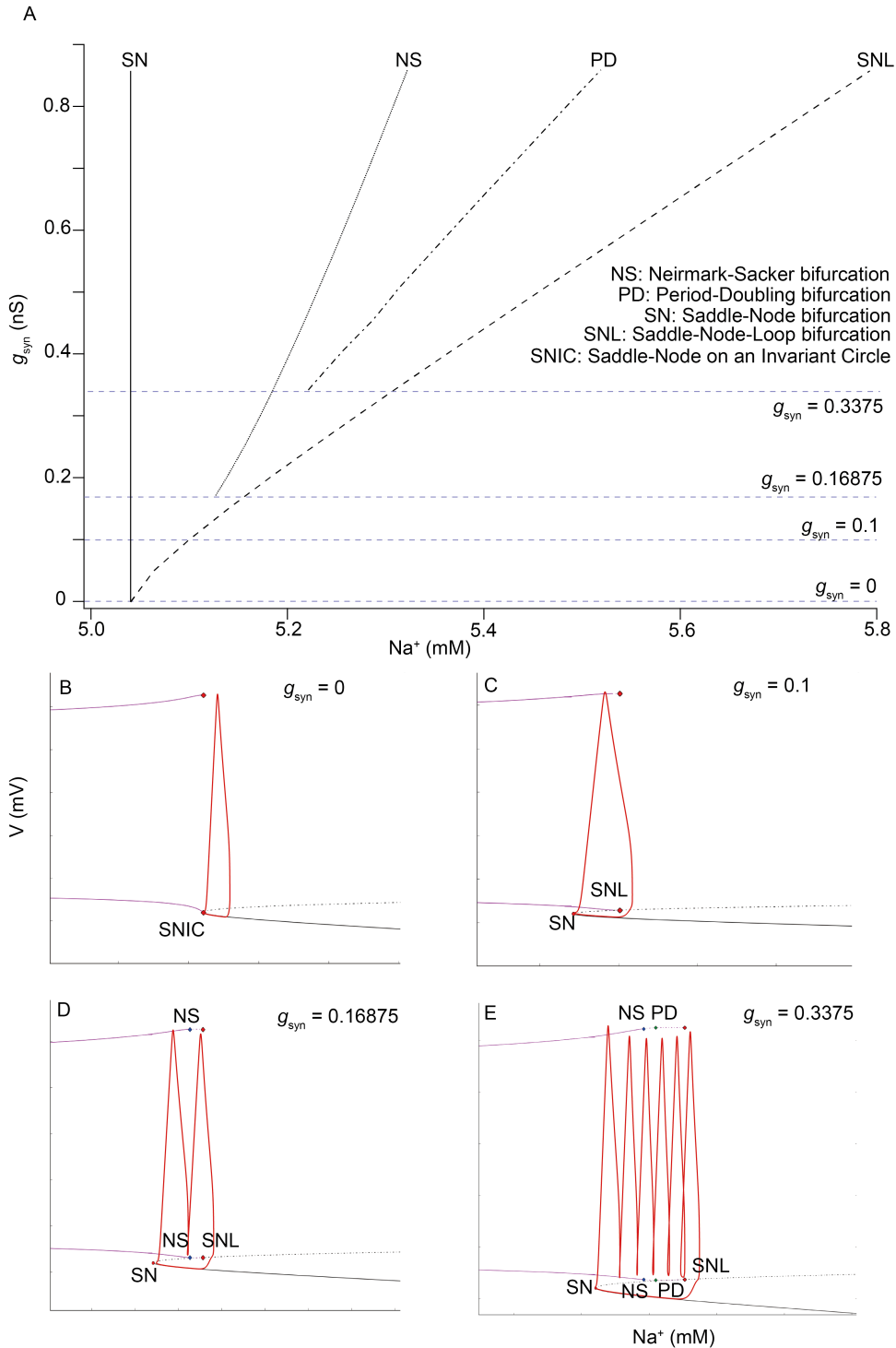
Figure 3.4. A. Two-parameter bifurcation diagram. For a selection of g_{syn} values, bifurcation points are numerically computed using *Na* as the bifurcation parameter. The solid line represents the saddle-node (SN) bifurcation. The finely dotted line represents the Neimark-Sacker (NS) bifurcation. The dash-dot line represents the period-doubling (PD) bifurcation, and the dashed line represents the saddle-node-loop (SNL) bifurcation. Blue horizontal dashed lines indicate four representative g_{syn} values, whose corresponding one-parameter bifurcation diagrams (*V-Na* space) in panels **B**, **C**, **D** and **E**. **B-E**. The bifurcation diagrams representing the slow manifold of the system for g_{syn} = 0 (**B**), 0.1 (**C**), 0.16875 (**D**), and 0.3375 (**E**), all in units of nS. The display conventions for panels B-E are in the same manner as Figure 3.3; each is superimposed with the red simulation trace of V versus *Na*.

Their intersection forms a saddle-node on an invariant circle (SNIC) bifurcation. This revised version (g_{syn} = 0 nS) of the model neuron generates tonic spikes instead of bursts. During each spike oscillation, the system traverses the SNIC bifurcation, and generates only one spike before the active phase terminates (Fig. 3.4B). The inter-spike interval takes place on the branch of stable nodes. According to the conventions in Fig. 3.3, the system evolves clockwise in Fig. 3.4B.

Increasing the g_{syn} to 0.1 nS exterminates the degenerate SNIC bifurcation but it does not destroy the existence of a homoclinic orbit. For g_{syn} > 0 nS, the minimum voltage reached during the limit cycle (indicated by lower purple curves in Figs. 3.3 and 3.4B-E) moves up onto the branch of saddle points. Now the homoclinic orbit is formed by the intersection of the stable and unstable manifolds of the saddle, which is recognized as a saddle-node-loop (SNL) bifurcation (Fig. 3.4A and C).

As g_{syn} is increased further, a NS bifurcation appears near g_{syn} = 0.16875 nS (Fig. 3.4A and D). Increasing g_{syn} has the practical effect of enhancing recurrent excitation, which causes more spikes in a burst. Synaptic facilitation, we hypothesize, comes into effect by accelerating the spikes and elevating the baseline membrane potentials such that the system follows the branch of stable limit cycles before the NS bifurcation. This hypothesis also agrees with the fact that during the early stage of bursting, the synaptic facilitation variable x increases significantly (0.35 – 0.8). When Na crosses the NS bifurcation, a torus (see Fig. 3.4A) is created, causing the spikes to decrease in amplitude while increasing in frequency during the burst.

Furthermore, when we keep increasing g_{syn} until it exceeds 0.3375 nS, a PD bifurcation is formed (Fig. 3.4A and E). In the context of bursts when g_{syn} = 0.3375 nS, when Na passes the PD bifurcation, synaptic depression depletes the readily releasable pool of synaptic vesicles, which exhausts the ability to engage in recurrent excitation, and the Na/K pump ATPase hyperpolarizes the system. Because the synaptic strength is higher for increasing values of g_{syn}, the SNL bifurcation point shifts to higher values of Na, farther away from the SN bifurcation (~5.05 mM), and this means that the system generates more spikes within a burst before burst termination. In Fig. 3.4A this point is illustrated by the V-shape of the diverging SN and SNL points along the ordinate axis.

As we described for g_{syn} = 0.6 nS and illustrated in Fig. 3.3, once in the quiescent phase, Na is pumped out by the ATPase Na/K pump. Na decrements cause the

trajectory to move leftward along the lower branch of stable nodes. Ultimately the state point passes once again the SN bifurcation, starting a new active phase.

3.3.2 Synaptic facilitation and depression both influence neuron interactions

To gain further understanding of how synaptic transmission influences burst-generating functions in this model, we simulate two neurons with different intrinsic properties, with neuron #1 more excitable than neuron #2. We impose a synaptic connection from neuron #1 to neuron #2 (but no reciprocal synapse from #2 to #1) and inject inward current pulses of 10 ms for two different time durations (50 ms and 150 ms) into neuron #1 (Fig. 3.5).

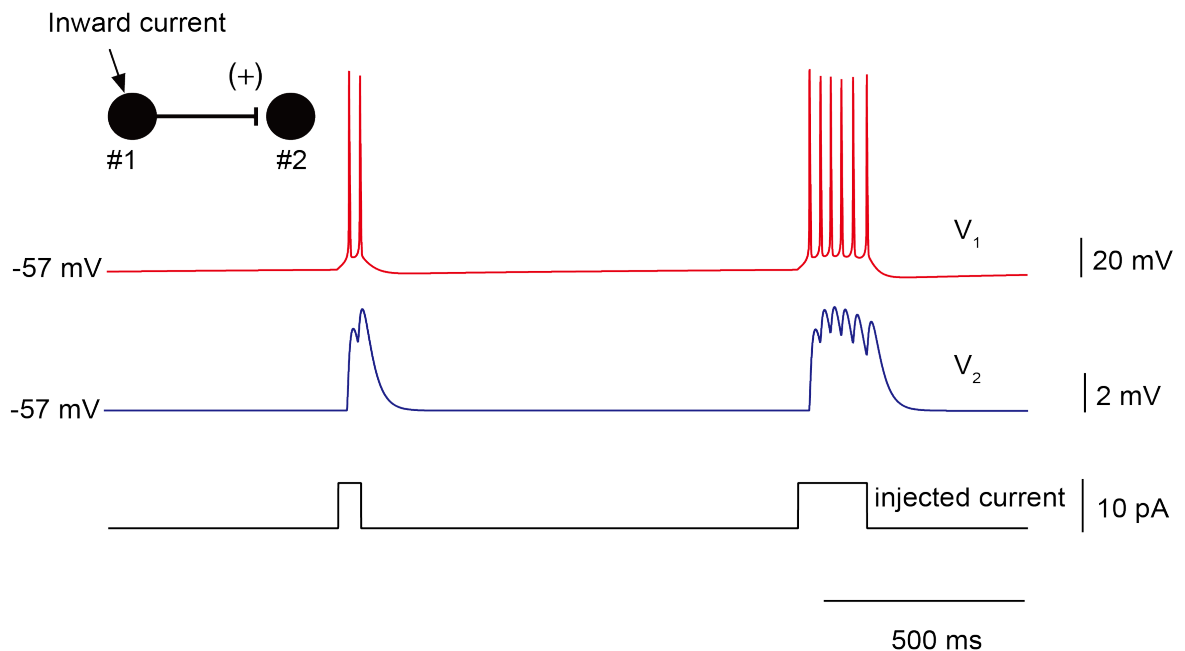**Figure 3.5**. Current clamp simulation to two synaptically coupled neurons. Neuron #1 projects synaptic connection to neuron #2 (schematic shown in upper left). A single current pulse is firstly injected to neuron #1 for 50 ms. A 150-ms current pulse with the same amplitude is implemented later in the simulation (bottom trace). Membrane potentials of both neurons are illustrated (red trace: neuron #1, blue trace: neuron #2).

In the presynaptic neuron (#1), a 50-ms depolarizing current pulse induces two spikes by depolarizing the membrane potential above spike threshold. The postsynaptic neuron, which receives synaptic drive from neuron #1, generates excitatory postsynaptic potentials (EPSP) with accumulating amplitudes when neuron #1 spikes, although the EPSPs are insufficient to evoke an action potential in neuron #2.

By comparison, when a 150-ms depolarizing current pulse is delivered to neuron #1 it evokes five spikes. These spikes drive summating EPSPs in neuron #2. However, since the number of docking sites in the RRP is limited by $y_{dock_{max}}$, there is less synaptic drive evoked by each successive spike and the amplitude of the EPSPs gradually decreases after the peak value; these decreasing EPSPs are the manifestation of synaptic depression. These results indicate that synaptic excitation will facilitate and (briefly) enhance the drive from the presynaptic to the postsynaptic neuron, but the ultimately the synaptic gating variable r and the fraction of synaptic vesicles in the RRP y_{dock} both decrease, indicating that the synaptic strength wanes after repetitive activation of the synapse.

3.3.3 Two neuron group-pacemaker simulation

Maintaining the intrinsic cellular properties from the current-clamp simulation (Fig. 3.5), we couple the two neurons to each other and perform numerical simulations to study the effect of reciprocal (rather than unidirectional) synaptic coupling. A synaptic connection from neuron #1 (which is tonically active [0.4 Hz] when isolated) excites neuron #2 (Fig. 3.6B), which in turn excites neuron #1 and the ensuing positive feedback cycle results in a burst. During a complete burst cycle,

the synaptic facilitation variable x in the presynaptic neuron increases exponentially at burst initiation and synaptic vesicles in the RRP begin to release neurotransmitter to facilitate the process of synaptic transmission in the postsynaptic neuron. However, since the available docking sites in the RRP are restricted by $y_{dock_{max}}$, during the burst, only this limited number of docked synaptic vesicles can be released, resulting in the decreasing of y_{dock} during the burst. During this process, the peak value of glutamate gating variable r begins to decrease concomitantly, hindering further synaptic drive and thus setting the stage for burst termination.
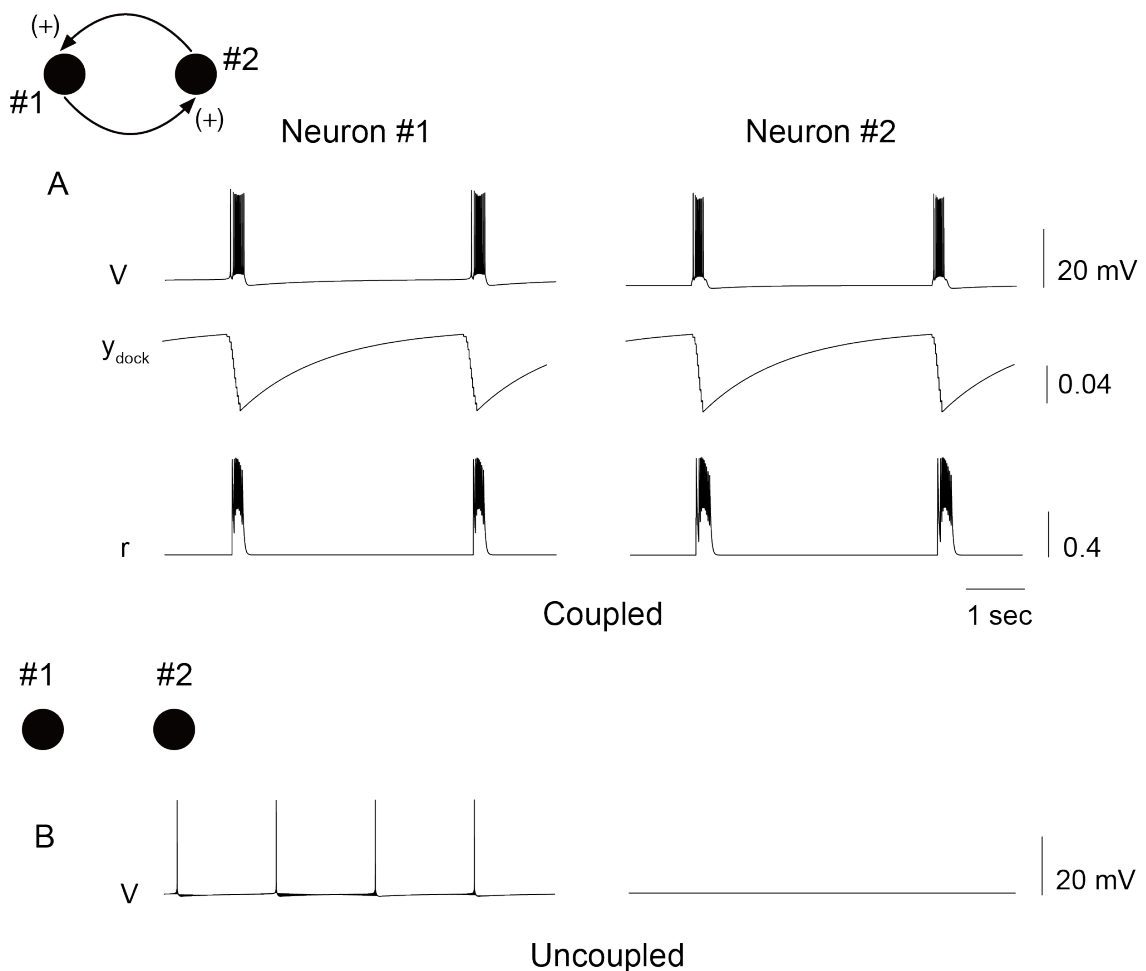
Figure 3.6. Two-neuron coupling simulation. Schematic diagram shows that synaptic connections are implemented between the two neurons. Coupled (**A**) scenario shows membrane potential (*V*), the fraction of readily releasable synaptic vesicles (y_{dock}) and glutamate gating variable (*r*). Uncoupled (**B**) scenario shows membrane potential (*V*).

In parallel, the electrogenic outward current due to the Na/K ATPase pump increases as the result of high level of Na^+ in the burst phase. During the inter-burst interval, membrane potentials in both neurons would return to resting state and synaptic vesicles also recovered into the RP, making the subsequent burst possible.

3.3.4 Ca2+ subsystem and a possible mechanism for generating 'sighs'

Aside from eupnea and gasping, sighs are also a normal component of mammalian respiratory behavior. Sighs are spontaneously generated in the respiratory central pattern generator, i.e., the preBötzinger complex (preBötC). A sigh is defined as a low-frequency (0.01 - 0.015 Hz) bi-phasic breathing activity, in which a burst with a larger amplitude is imposed during a typical eupnea-like inspiratory burst (Cherniack et al., 1981; Orem and Trotter, 1993; Takeda and Matsumoto, 1997; Lieske et al., 2000; Chapuis et al., 2014). Moreover, sighs have been observed in *in vitro* experiments using slice preparations containing the preBötC (Lieske et al., 2000; Ruangkittisakul et al., 2008; Tryba et al., 2008; Li et al., 2016). The particularly trenchant recent study by Li *et al.* indicates that the sigh-generating ability may reside in a subset of ~200 preBötC neurons that express receptors for bombesin-like peptide transmitters, but it is possible that all preBötC neurons would participate during the sigh events triggered by this subset of ~200. This suggests that sigh-generating mechanisms may be latent

during normal eupnea like breathing and yet become periodically recruited for sighs.

In our modeling study, we also attempt to incorporate sigh generation as a feature of the new preBötC interneuron model. As recapped above, a latent sigh-generating mechanism may reside in each rhythmogenic preBötC neuron such that sighs would emerge due to a slow oscillation within the context of the already-oscillatory network that generates eupneic inspiratory rhythm. Previous studies have shown that Ca^{2+} activity may contribute to sigh generation but not be critical for eupnea-like burst initiation (Lieske et al., 2000; Lieske and Ramirez, 2006; Tryba et al., 2008; Beltran-Parrazal et al., 2012). According to this hypothesis, we added the following equations of Ca^2 dynamics to our model, describing in detail the endoplasmic reticulum (ER) activity as well as the Ca^{2+}-induced-Ca^{2+}-release (CICR) process, as a slow oscillator that only bursts every 40-60 sec without perturbing the eupnea-like bursts

$$V_{serca} = V_{m2} \cdot (Ca^2 / (Ca^2 + k_2^2)), \ V_{plc} = V_p \cdot (Ca^2 / (Ca^2 + k_2^2)),$$

$$V_{CICR} = 4 \cdot V_{m3} \cdot \left(\frac{(k_{CaA} \cdot Ca)^N}{(Ca^N + k_{CaA}^N)(Ca^N + k_{CaI}^N)} \right) \cdot \left(\frac{ip^M}{ip^M + k_{ip3}^M} \right) \cdot (Ca_{ER} - Ca)$$

and two ODEs for the IP_3 concentration and ER Ca^{2+} concentration

$$\frac{dip}{dt} = V_{plc}(Ca) - k_{deg} \cdot ip, \ \frac{dCa_{ER}}{dt} = V_{serca}(Ca) - V_{CICR}(Ca, ip, Ca_{ER}) - k_f \cdot (Ca_{ER} - Ca).$$ We modify the ODE of Ca^{2+} concentration in the original model to reflect the effects from these changes (Lavrentovich and Hemkin, 2008):

$$\frac{dCa}{dt} = -\alpha_{Ca} \cdot I_{Ca}(V, m_{Ca}, h_{Ca}, Ca) + (V_{CICR}(Ca, ip, Ca_{ER}) - V_{serca}(Ca) + k_f \cdot (Ca_{ER} - Ca)) - Ca / \tau_{Ca}$$

Of these equations, V_{serca} describes the sarco(endo)plasmic Ca^{2+} ATPase

(SERCA) pump that mediates Ca^{2+} entering ER from cytosol with V_{m2} being the

maximum flux of Ca^{2+} from the pump (Schatzmann, 1989; Falcke, 2004). V_{plc}

describes phospholipase C (PLC) activity in the same manner as V_{serca}. V_{CICR}

describes the IP$_3$ receptor-mediated influx of Ca^{2+} from the ER to the cytosol with

V_{m3} being the maximum flux, k_{CaA} and k_{CaI} the activiting and inhibiting affinities,

and N the Hill coefficient (Höfer, 1999; Tu et al., 2005a, 2005b). In the newly

added ODEs, k_{deg} is the degradation rate of IP$_3$ and k_f models the leakage rate

of Ca^{2+} within the exchange between ER and cytosol (Houart, 1999; Höfer et al.,

2002). Associated parameters take the following values (Lavrentovich and

Hemkin, 2008):

$V_{m2} = 15\ \mu M/s, V_{m3} = 40\ s^{-1}, V_p = 0.05\ \mu M/s, k_2 = 0.1\ \mu M, k_{CaA} = 0.15\ \mu M,$

$k_{CaI} = 0.15\ \mu M, k_{ip3} = 0.1\ \mu M,\ k_p = 0.3\ \mu M, k_{deg} = 0.08\ s^{-1}, k_f = 0.5\ s^{-1},$

$N = 2.02, M = 2.2.$

Then we run a 100-sec simulation on a self-coupled model neuron to test the

eupnea sigh alternation while monitoring the membrane potential, I_{CAN} and

cytosol Ca^{2+} (Fig. 3.7).

During the 100-sec simulation, two sigh-like bursts occur and the interval

between is 40 sec. When we prolong the duration of the simulation to 400 sec,

this period for sigh-like bursts varies little. We find that cytosolic Ca^{2+}

accumulates during a total of approximately 10 eupnea-like bursts before

increasing significantly to activate I_{CAN} to initiate a sigh-like burst. In contrast,

blocking the voltage dependent I_{Ca} or the ER pathway abolishes sigh-like bursts

without affecting eupnea-like bursts, suggesting that ER activity and periodic I_{CAN} activation is essential in sigh generation.
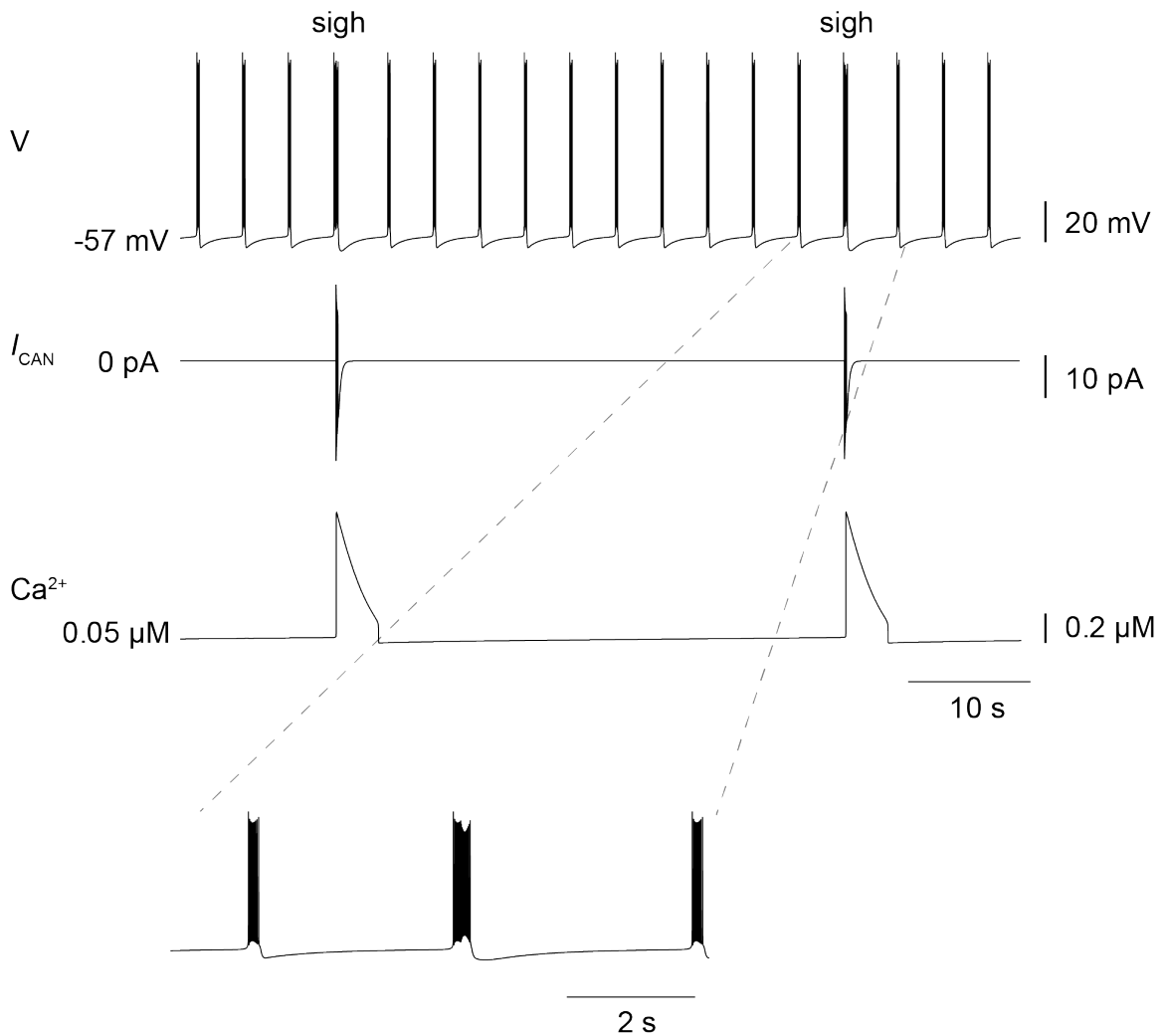
Figure 3.7. Self-coupled neuron simulation including a Ca^{2+} subsystem. Membrane potential is shown with two sigh-like bursts indicated. The traces of I_{CAN} and Ca^{2+} are also illustrated where the bursts occur simultaneously with the sigh-like bursts in the membrane potential trace. A 10-sec part of the membrane potential trace shown at higher sweeping speed to illustrate eupnea inspiratory and sigh-like bursts.

Furthermore, when zooming in on a single sigh-like burst, our model performance is consistent with the experimental finding that a sigh, by its nature, is a bursting phase with larger amplitude imposed on a typical eupnea-like burst

(Lieske et al., 2000; Ruangkittisakul et al., 2008; Chapuis et al., 2014; Li et al., 2016); therefore the duration for a sigh-like burst (550 ms) is approximately 2.5 times of a eupnea-like burst (210 ms). Moreover, due to the long duration of sigh-like bursts, Na^+ influx is larger than that during an eupnea-like burst, leading to a stronger activation of the ATPase Na/K pump and resulting in a longer inter-burst interval after a sigh-like burst.

3.4 DISCUSSION

After reviewing the evolution of models of respiratory rhythm generation over the past few decades, and assessing their strengths and weakness, we have constructed a group-pacemaker model that is generally consistent with all existing data about the cellular and ionic mechanisms of rhythm generation. When self-coupled, our model can generate robust eupnea-like inspiratory bursts via a biophysically realistic synapse-driven recurrent excitation followed by burst termination due to synaptic depression and Na/K ATPase pump.

In the original Rubin-Hayes model, the starting point for our model, the burst initiation and termination mechanisms were linked to synapse-driven Ca^{2+} accumulation and consequent I_{CAN} activation. By contrast, in the present study, synaptic facilitation governs burst continuation, while synaptic depression begins burst termination and I_{CAN} only serves as a "safety factor" that enhances the robustness of inspiratory bursts instead of an obligatory burst-generating inward current. Moreover, instead of two distinct channels for transient and persistent Na^+ current, we utilize a unified Na^+ channel combining both transient and persistent components, which acts as the main charge carrier for the action

111

potentials. We also maintain the Na/K ATPase pump current as a hyperpolarizing mechanism that mediates burst termination and influences the inter-burst interval by means of its slow deactivation as Na^+ is cleared from the cytosol. Recognizing *Na* as a slow variable in the system, which, when fixed at different values allowed us to study transitions of the system between an oscillatory and a quiescent state, i.e., we treated it as a bifurcation parameter. By varying g_{syn} to manipulate the synaptic strength, we determined the dynamics in our system such that burst initiates at a SN bifurcation and ends near a SNL (for $g_{syn} \neq 0$, the system crosses the unstable manifold of the saddle point while $Na < Na_{SNL}$), but in the intervening parts of the burst phase passes through a NS and a PD bifurcation for increasing values of g_{syn}. These NS and PD bifurcations have not heretofore been associated with oscillatory bursting neuron models and represent a novel intellectual contribution of this oeuvre (Bertram et al., 1995; Izhikevich and Hoppensteadt, 2004; Guckenheimer et al., 2005).

We then performed a current clamp simulation to study the EPSPs in the postsynaptic neuron. We observed that EPSPs could be facilitated during repetitive synaptic activation, but that facilitation was short-lived (~50 ms) and rather than growing in amplitude and summation, instead we found that the amplitude EPSPs decreased in the process of continuous synaptic transmission as a result of synaptic depression.

By synaptically coupling two neurons to one another, robust and synchronized eupnea-like bursts were possible in the minimal network. Furthermore, when we inserted the Ca^{2+} subsystem including the ER activity and CICR process, a slow

oscillatory mechanism heavily relying on I_{CAN} activation was achieved in the model such that the self-coupled model neuron could generate low-frequency biphasic sigh-like bursts without affecting typical eupnea-like bursts.

In summary, the cellular model proposed in the present study, to a large extent, captures the biophysical realism of neurons in the rhythmogenic kernel. This synapse-driven group pacemaker model, when coupled, generates robust eupnea-like inspiratory bursts. The mechanism underlying sighs has not been determined experimentally. Whether a subpopulation of sigh-only neurons exists or every rhythmogenic neuron possesses the ability to generate sighs, our Ca^{2+} subsystem would allow us to model either option by including (or not) a slow oscillator including an ER and the CICR mechanisms in all consituent preBötC interneurons. Due to the abstract nature of mathematical models, ours does not fully capture every aspect of rhythmogenic preBötC neurons, but rather encapsulates advantages from a number of previously established models, including the I_{CAN} and I_{pump} from the Rubin-Hayes model, the I_{Ca} from the Jasinski model, the unified I_{Na} from the Ptak study and the synaptic dynamic from the Guerrier model (Ptak et al., 2005; Rubin et al., 2009; Jasinski et al., 2013; Guerrier et al., 2015).

3.4.1 Further investigations of the nonlinear dynamics of model bursting

Aside from its performance as a specifically respiratory model of the neurons in the preBötC, the cellular model in the present study shows a rich dynamic structure from the perspective of general bursting mechanisms.

In the context of the burst classification scheme introduced by Rinzel (Rinzel, 1987) and further articulated by Bertram *et al.* (1995), our system does not exactly fit the description of any of the three canonical types of bursting oscillators, although there are some similarities that we discuss below.

Type I bursting, often called *square-wave* bursting, has a SN burst initiation and a homoclinic SNL-like burst termination with a hysteresis loop of bi-stability, which have also been found in our system. However, type I bursting requires that the frequency of spiking decrease monotonically through the burst whereas in our system the spike rate and amplitude are modulated at burst onset and then further affected by the NS and PD bifurcations, resulting in the spiking frequency accelerating momentarily before slowing down. Our system has more state variables than the lower dimensional Chay-Cook model used in Bertram's classification scheme (Bertram et al., 1995), so the dynamics in our model have the potential to be more complex than the canonical type I system Bertram et al. analyzed.

For type II bursting system, two slow variables are required for the occurrence of oscillation regardless of spiking in the fast subsystem, and the bursting phase begins and ends at SNIC, causing a "parabolic bursting" in which the spiking frequency increases and then decreases during the bursting phase. However, our system could not oscillate without spikes. Even though the bursting in our system appears to also show a qualitatively similar bursting in terms of spike frequency, when synaptic transmission is strong enough to evoke a burst, the bursting phase starts off a SN bifurcation and terminates near a SNL instead of

SNIC. The only time our model exihibits a SNIC is during the g_{syn} = 0 nS regime, and that gives rise to tonic spiking, not bursting.

Our system is certainly not a type III bursting system since the branch of stable nodes traversed during the quiescent phase is the same branch of nodes born at the Hopf bifurcation, and in type III system this means that the quiescent state has a voltage value well depolarized to rest and in fact close to, or slightly exceeding, the spike threshold. In our system, in contrast, the lower bound of the limit cycle resides at voltages that exceed the branch of stable nodes by 10 - 15 mV. Furthermore, bursts terminate during type III bursting via a saddle-node of limit cycles bifurcation (also known as a saddle-node of periodics [SNP]) instead of near a homoclinic SNL bifurcation. Finally, type III bursting systems are typically characterized by intra-burst spike frequencies that remain unchanged during a burst and depend on the imaginary eigenvalues of the Hopf bifurcation, regardless of the existence of homoclinic orbits; whereas our system shows clear modulation of spike frequency during the burst due to the presence of a homoclinic orbit at burst termination.

In short, our system resembles type I bursting such that the burst in both systems begins via a SN bifurcation and terminates near a SNL but the dynamics of our system is more complicated that the spiking frequency is modulated during the burst and a NS as well as a PD bifurcation occur in the process.

In the absence of synaptic transmission, our system could only generate tonic spikes, which begin at a degenerate SNIC bifurcation and end when the trajectory is at its minimum in voltage, crosses the unstable manifold, which is

separatrix associated with a saddle point. But when taking g_{syn} into consideration, the synaptic current is responsible for the number of spikes in a burst. As g_{syn} increases, more intra-burst spikes occur per burst cycle.

The explanation for the NS bifurcation and the occurrence of PD bifurcation when further increasing g_{syn} are not fully understood. The NS bifurcation, also known in general as the secondary Hopf bifurcation or Hopf bifurcation for maps, is the birth of a torus from a limit cycle, i.e., a second limit cycle periodically modulates the pre-existing limit cycle, which changes its stability (Kuznetsov and Sacker, 2008). This bifurcation structure has been reported in discrete systems such as predator-prey and population of genetics models (Dénes, 2007; Hone et al., 2010). Also the occurrence of torus bifurcation was reported in neuronal bursting models such that torus bifurcation with a rapid amplitude increase was responsible for the transition from spiking to bursting (Burke et al., 2012). However our present identification of an NS bifurcation in a realistic biophysical cellular model is a novel discovery. Using *Na* as the bifurcation parameter, we only located an oscillatory regime within a realistic parameter range of [4.8 mM, 6 mM], which only allowed us to determine the terminating points for the oscillation without numerically identifying the location underlying the birth of the stable limit cycle (Figs. 3.3 and 3.4). However, when continuing our computations beyond this parameter range, i.e., to *Na* concentrations far outside physiologically realistic values, we located a subcritical Hopf bifurcation occurring at *Na* = 30 mM, and the NS bifurcation appears to originate from a saddle-node of limit cycles (or SNP) formed from an unstable branch of limit cycles originating from this Hopf

bifurcation at high *Na*. Due to the numerical restriction of our simulations, we were unable to further analyze the influence of this Hopf bifurcation and the saddle-node of limit cycles to the dynamical structures that govern the bursting mechanism.

From a purely dynamical point of view, there are many distinct bifurcation structures underlying bursting models (Izhikevich, 2000). But it is difficult to assign each bifurcation to a specific biophysical feature of a cellular model. In our case, the synaptic dynamics is modeled in detail using equations representing synaptic vesicles in different pools. Synaptic facilitation and depression are also shown in numerical simulations. However, we have yet to numerically identify the roles of such properties in terms of how they affect the dynamical structures, for example, the relationship between the maximum number of docking cites in RRP $y_{dock_{max}}$ and the onset of PD bifurcation, or the influence of the time constant for y_{dock} to the occurrence of the NS bifurcation. Moreover, the birth of the NS bifurcation has not been numerically identified. During the bifurcation analysis in this study, we provide a qualitative description of the origin and effect of the NS bifurcation that since the system continues to spike after the NS bifurcation with lower amplitude and higher frequency, a weakly stable torus is created, hinting a supercritical NS bifurcation (Kuznetsov, 1998; Izhikevich, 2000). But we could not numerically specify the torus generated by the NS bifurcation to categorize it as supercritical or subcritical.

In our future efforts, we aim to non-dimensionalize our system using a fast time scale to simplify the equations and adopt the singular perturbation method to

conduct the fast-slow system analysis (Matkowsky and Reiss, 1977; Fenichel, 1979; Vo et al., 2010). Hence we could achieve a singularly perturbed system containing slow variables of our choice (i.e., *Na*), fast variable (V) and a perturbation parameter that evolves with a slow dimensionless timescale. In this approximated system, we could save a large amount of computational expense in exchange for a detailed bifurcation diagram with smaller time step. Meanwhile, we plan to adopt the software VFGEN (Vector Field File Generator, http://www.warrenweckesser.net/vfgen/index.html) to import our bifurcation analysis files onto other simulation platforms such as MATCONT (http://www.matcont.ugent.be/) or AUTO (http://indy.cs.concordia.ca/auto) with the purpose of illustrating the bifurcation structures with better resolution and identifying the location and stability of the torus created by the NS bifurcation. We believe that further exploration of the dynamical structure of our model would deepen our understanding of how ionic mechanisms interact with synaptic dynamics in the model in order to determine the proper parameter regime for bursting and how the various bifurcation structure and quiescence/spiking transitions correspond to the functionality of the different components in the model.

3.4.2 Improving the rhythmogenic preBötC network model
The cellular model in the present study includes a biophysically realistic synaptic current, which includes synaptic facilitation and depression as well as a glutamate gating variable. Therefore, a model preBötC network (with a realistic number of constituent neurons, not simply self-coupled or reciprocally coupled

pairs) using this model would allow us to simulate real experiments, whose purpose would be to study the initiation and termination of bursts, as well as other properties of the real preBötC.

In determining the boundary condition of how many neurons have to be activated to evoke a network-wide burst, simultaneously stimulating 4-9 preBötC neurons, endogenous-like bursts would be induced with a delay of 255 ms on average (Kam et al., 2013b). In the model network consisting of 330 Rubin-Hayes type neurons, we achieved the effect of stimulation by elevating the synaptic gating variable, which is an abstraction of synaptic dynamics (Song et al., 2015). However, for the new cellular model, we could stimulate the cell in a more realistic way by directly elevating the glutamate gating variable. The results of these simulations would provide a boundary condition of the number of neurons that have to be activated before the occurrence of a network-wide burst in our model network. Our estimate, divided by the experimental number (i.e., 4-9, described above), would provide us with a ratio, which would assist us in predicting the actual size of the rhythmogenic network. These criteria obtained from the holographic photostimulation experiments (Kam et al., 2013a) may also help us set a realistic value for synaptic coupling probability as well as g_{syn}.

In another study, short-term synaptic depression was studied. A refractory period was defined as the minimum duration after an endogenous inspiratory burst necessary to evoke a subsequent inspiratory burst. It was discovered that a refractory period ~2 sec existed by applying laser pulses to the preBötC neurons expressing channelrhodopsin at increasing intervals after endogenous inspiratory

bursts (Kottick and Del Negro, 2015). A network model using the new cellular

model would allow us to numerically simulate the experiment. By systematically

manipulating the duration of the stimulation or the maximum number of docking

sites within the RRP as an indicator of the strength of synaptic depression, we

could numerically compute the relationship between the refractory period and the

bursting duration. This exploration would allow us to determine a more

biophysically realistic parameter regime underlying the dynamics of the major

synaptic state variables in our system including x, y_{free} and y_{dock}.

On the other hand, even though we are interested in studying the rhythmogenic

preBötC as a neuronal network, to study the intrinsic mechanisms and

interactions among neurons requires a thorough examination of the constituent

neuron regarding its cellular and synaptic properties. Therefore in the present

study, we construct a cellular model and only study the minimal network

configuration for this model by either autapse or reciprocal coupling. We have not

implemented the model on a network scale where hundreds of neurons, with

intrinsic heterogeneity and specific topologies for connectivity, are simulated.

In the past, we adopted the Rubin-Hayes model to establish a model preBötC

with a random network of a fixed connection rate and connected it with a model

premotor population to study the robustness of network functionality (Wang et al.,

2014; Song et al., 2015, 2016). Those simulations were done to compare to

experimental benchmarks in which we used an ultra-fast pulsed laser to

cumulatively kill neurons within the preBötC while monitoring breathing-related

motor output from an *in vitro* slice model of breathing (Wang et al., 2014). Our

model rhythmogenic circuitry could qualitatively replicate the laser ablation experiments in which the rhythmic amplitude declined precipitously after less than 15 neuron deletions and the respiratory rhythm terminated after an average of 39 neuron deletions. In the meantime, there have also been some disparities between numerical simulation and experiments. In the circumstance of preBötC neuronal deletions, the numerical simulation suggested that cumulative removal of 12% of the rhythmogenic neurons would cease further rhythm generation, the number of which was approximately 6% lower than that in the experiments (Wang et al., 2014), suggesting the realistic rhythmogenic preBötC network is more robust than our model network. Hence, for the next stage of network modeling, we plan to adopt the next generation cellular model proposed in this study and construct a more realistic model preBötC network with detailed connectivity schemes instead of random connections with a fixed probability. For instance, we could rewire the synaptic connections among the neurons based on a randomly connected network according to their different intrinsic properties such as leakage conductance and initial conditions in a way to make the network more robust and efficient in synaptic transmission in order to achieve synchronization in the event of network-wide bursting. For a model network as such, its functionality would be more robust in terms of clustering or synaptic transmission. The network, then, would endure a larger number of neuron deletions before the rhythm termination. Therefore, to construct a network model using this new cellular model and an improved topological connection strategy would strengthen our understanding of the laser ablation experiments and

provide a computational insight of how rhythmogenic neurons are interconnected within preBötC.

BIBLIOGRAPHY

Achard S, Salvador R, Whitcher B, Suckling J, Bullmore E (2006) A Resilient, Low-Frequency, Small-World Human Brain Functional Network with Highly Connected Association Cortical Hubs. J Neurosci 26:63–72.

Alzheimer C, Schwindt PC, Crill WE (1993) Modal gating of Na+ channels as a mechanism of persistent Na+ current in pyramidal neurons from rat and cat sensorimotor cortex. J Neurosci Off J Soc Neurosci 13:660–673.

Barabási A-L, Albert R (1999) Emergence of Scaling in Random Networks. Science 286:509–512.

Bassett DS, Bullmore E (2006) Small-World Brain Networks. The Neuroscientist 12:512–523.

Beltran-Parrazal L, Fernandez-Ruiz J, Toledo R, Manzo J, Morgado-Valle C (2012) Inhibition of endoplasmic reticulum Ca^{2+} ATPase in preBötzinger complex of neonatal rat does not affect respiratory rhythm generation. Neuroscience 224:116–124.

Ben-Mabrouk F, Amos LB, Tryba AK (2012) Metabotropic glutamate receptors (mGluR5) activate transient receptor potential canonical channels to improve the regularity of the respiratory rhythm generated by the pre-Bötzinger complex in mice. Eur J Neurosci 35:1725–1737.

Bennett PB, Yazawa K, Makita N, George AL (1995) Molecular mechanism for an inherited cardiac arrhythmia. Nature 376:683–685.

Bertram R, Butte MJ, Kiemel T, Sherman A (1995) Topological and phenomenological classification of bursting oscillations. Bull Math Biol 57:413–439.

Bouvier J, Thoby-Brisson M, Renier N, Dubreuil V, Ericson J, Champagnat J, Pierani A, Chédotal A, Fortin G (2010) Hindbrain interneurons and axon guidance signaling critical for breathing. Nat Neurosci 13:1066–1074.

Burke J, Desroches M, Barry AM, Kaper TJ, Kramer MA (2012) A showcase of torus canards in neuronal bursters. J Math Neurosci 2:3.

Butera RJ, Rinzel J, Smith JC (1999) Models of respiratory rhythm generation in the pre-Bötzinger complex. I. Bursting pacemaker neurons. J Neurophysiol 82:382–397.

Carroll MS, Ramirez J-M (2013) Cycle-by-cycle assembly of respiratory network activity is dynamic and stochastic. J Neurophysiol 109:296–305.

Carroll MS, Viemari J-C, Ramirez J-M (2013) Patterns of inspiratory phase-dependent activity in the in vitro respiratory network. J Neurophysiol 109:285–295.

Chamberlin NL, Eikermann M, Fassbender P, White DP, Malhotra A (2007) Genioglossus premotoneurons and the negative pressure reflex in rats. J Physiol 579:515–526.

Chapuis C, Autran S, Fortin G, Simmers J, Thoby-Brisson M (2014) Emergence of sigh rhythmogenesis in the embryonic mouse: Sigh in mouse embryo. J Physiol 592:2169–2181.

Cherniack NS, von Euler C, Głogowska M, Homma I (1981) Characteristics and rate of occurrence of spontaneous and provoked augmented breaths. Acta Physiol Scand 111:349–360.

Cowan W, Fawcett J, O'Leary D, Stanfield B (1984) Regressive events in neurogenesis. Science 225:1258–1265.

Crowder EA, Saha MS, Pace RW, Zhang H, Prestwich GD, Del Negro CA (2007) Phosphatidylinositol 4,5-bisphosphate regulates inspiratory burst activity in the neonatal mouse preBötzinger complex. J Physiol 582:1047–1058.

Del Negro CA, Hayes JA, Rekling JC (2011) Dendritic calcium activity precedes inspiratory bursts in preBotzinger complex neurons. J Neurosci 31:1017–1022.

Del Negro CA, Kam K, Hayes JA, Feldman JL (2009) Asymmetric control of inspiratory and expiratory phases by excitability in the respiratory network of neonatal mice in vitro. J Physiol 587:1217–1231.

Del Negro CA, Koshiya N, Butera RJ Jr, Smith JC (2002a) Persistent sodium current, membrane properties and bursting behavior of pre-bötzinger complex inspiratory neurons in vitro. J Neurophysiol 88:2242–2250.

Del Negro CA, Morgado-Valle C, Feldman JL (2002b) Respiratory rhythm: an emergent network property? Neuron 34:821–830.

Del Negro CA, Morgado-Valle C, Hayes JA, Mackay DD, Pace RW, Crowder EA, Feldman JL (2005) Sodium and calcium current-mediated pacemaker neurons and respiratory rhythm generation. J Neurosci 25:446–453.

Dénes A (2007) Neimark-Sacker bifurcation in a discrete dynamical model of population genetics. In, pp 1–10. Bolyai Institute, SZTE.

Diestel R (2010) Graph theory, 4th ed. Heidelberg ; New York: Springer.

Dobbins EG, Feldman JL (1994) Brainstem network controlling descending drive

to phrenic motoneurons in rat. J Comp Neurol 347:64–86.

Doble A (1996) The pharmacology and mechanism of action of riluzole. Neurology 47:S233–S241.

Dunmyre JR, Del Negro CA, Rubin JE (2011) Interactions of persistent sodium and calcium-activated nonspecific cationic currents yield dynamically distinct bursting regimes in a model of respiratory neurons. J Comput Neurosci 31:305–328.

Falcke M (2004) Reading the patterns in living cells —the physics of ca2+ signaling. Adv Phys 53:255–440.

Feldman JL, Cleland CL (1982) Possible roles of pacemaker neurons in mammlian respiratory rhythmogenesis. Cellular Pacemakers. New York: Wiley.

Feldman JL, Del Negro CA (2006) Looking for inspiration: new perspectives on respiratory rhythm. Nat Rev Neurosci 7:232–242.

Feldman JL, Del Negro CA, Gray PA (2013) Understanding the Rhythm of Breathing: So Near, Yet So Far. Annu Rev Physiol 75:423–452.

Feldman JL, Smith JC (1989) Cellular mechanisms underlying modulation of breathing pattern in mammals. Ann N Y Acad Sci 563:114–130.

Fenichel N (1979) Geometric singular perturbation theory for ordinary differential equations. J Differ Equ 31:53–98.

Flavell SW (2006) Activity-Dependent Regulation of MEF2 Transcription Factors Suppresses Excitatory Synapse Number. Science 311:1008–1012.

Fregosi RF, Bailey EF, Fuller DD (2011) Respiratory muscles and motoneurons. Respir Physiol Neurobiol 179:1–2.

Funk GD, Greer JJ (2013) The rhythmic, transverse medullary slice preparation in respiratory neurobiology: contributions and caveats. Respir Physiol Neurobiol 186:236–253.

Funk GD, Smith JC, Feldman JL (1993) Generation and transmission of respiratory oscillations in medullary slices: role of excitatory amino acids. J Neurophysiol 70:1497–1515.

Ge Q, Feldman JL (1998) AMPA receptor activation and phosphatase inhibition affect neonatal rat respiratory rhythm generation. J Physiol 509 (Pt 1):255–266.

Gilbert EN (1959) Random Graphs. Ann Math Stat 30:1141–1144.

Gray PA, Hayes JA, Ling GY, Llona I, Tupal S, Picardo MCD, Ross SE, Hirata T, Corbin JG, Eugenín J, Del Negro CA (2010) Developmental origin of preBötzinger complex respiratory neurons. J Neurosci 30:14883–14895.

Gray PA, Janczewski WA, Mellen N, McCrimmon DR, Feldman JL (2001) Normal breathing requires preB?tzinger complex neurokinin-1 receptor-expressing neurons. Nat Neurosci 4:927–930.

Greer JJ, Smith JC, Feldman JL (1991) Role of excitatory amino acids in the generation and transmission of respiratory drive in neonatal rat. J Physiol 437:727–749.

Grillner S (2006) Biological pattern generation: the cellular and computational logic of networks in motion. Neuron 52:751–766.

Grillner S, Jessell TM (2009) Measured motion: searching for simplicity in spinal locomotor networks. Curr Opin Neurobiol 19:572-586

Guckenheimer J, Tien JH, Willms AR (2005) Bifurcations in the fast dynamics of neurons: implications for bursting. In: Bursting, pp 89-122. World Scientific

Guerrier C, Hayes JA, Fortin G, Holcman D (2015) Robust network oscillations during mammalian respiratory rhythm generation driven by synaptic dynamics. Proc Natl Acad Sci U S A 112:9728–9733.

Guinamard R, Simard C, Del Negro C (2013) Flufenamic acid as an ion channel modulator. Pharmacol Ther 138:272–284.

Hayes JA, Wang X, Del Negro CA (2012) Cumulative lesioning of respiratory interneurons disrupts and precludes motor rhythms in vitro. Proc Natl Acad Sci U S A 109:8286–8291.

Höfer T (1999) Model of Intercellular Calcium Oscillations in Hepatocytes: Synchronization of Heterogeneous Cells. Biophys J 77:1244–1256.

Höfer T, Venance L, Giaume C (2002) Control and plasticity of intercellular calcium waves in astrocytes: a modeling approach. J Neurosci Off J Soc Neurosci 22:4850–4859.

Hone ANW, Irle MV, Thurura GW (2010) On the Neimark-Sacker bifurcation in a discrete predator-prey system. J Biol Dyn 4:594–606.

Houart G (1999) Bursting, Chaos and Birhythmicity Originating from Self-modulation of the Inositol 1,4,5-trisphosphate Signal in a Model for Intracellular Ca2+Oscillations. Bull Math Biol 61:507–530.

Humphries M., Gurney K, Prescott T. (2006) The brainstem reticular formation is a small-world, not scale-free, network. Proc R Soc B Biol Sci 273:503–

511.

Izhikevich EM (2000) Neural Excitability, spiking and bursting. Int J Bifurc Chaos
10:1171–1266.

Izhikevich EM, Hoppensteadt F (2004) Classification of bursting mappings. Int J
Bifurc Chaos 14:3847–3854.

Jasinski PE, Molkov YI, Shevtsova NA, Smith JC, Rybak IA (2013) Sodium and
calcium mechanisms of rhythmic bursting in excitatory neural networks of
the pre-B?tzinger complex: a computational modelling study. Eur J
Neurosci 37:212–230.

Johnson SM, Smith JC, Funk GD, Feldman JL (1994) Pacemaker behavior of
respiratory neurons in medullary slices from neonatal rat. J Neurophysiol
72:2598–2608.

Kam K, Worrell JW, Ventalon C, Emiliani V, Feldman JL (2013a) Emergence of
Population Bursts from Simultaneous Activation of Small Subsets of
preBötzinger Complex Inspiratory Neurons. J Neurosci 33:3332–3338.

Kam K, Worrell JW, Janczewski WA, Cui Y, Feldman JL (2013b) Distinct
inspiratory rhythm and pattern generating mechanisms in the preBötzinger
complex. J Neurosci 33:9235–9245.

Kobayashi K, Lemke RP, Greer JJ (2001) Ultrasound measurements of fetal
breathing movements in the rat. J Appl Physiol Bethesda Md 1985
91:316–320.

Koizumi H, Smith JC (2008) Persistent Na+ and K+-dominated leak currents
contribute to respiratory rhythm generation in the pre-Bötzinger complex in
vitro. J Neurosci 28:1773–1785.

Koizumi H, Wilson CG, Wong S, Yamanishi T, Koshiya N, Smith JC (2008)
Functional Imaging, Spatial Reconstruction, and Biophysical Analysis of a
Respiratory Motor Circuit Isolated In Vitro. J Neurosci 28:2353–2365.

Koshiya N, Smith JC (1999) Neuronal pacemaker for breathing visualized in vitro.
Nature 400:360–363.

Kottick A, Del Negro CA (2015) Synaptic Depression Influences Inspiratory-
Expiratory Phase Transition in Dbx1 Interneurons of the preBotzinger
Complex in Neonatal Mice. J Neurosci 35:11606–11611.

Krey RA, Goodreau AM, Arnold TB, Del Negro CA (2010) Outward Currents
Contributing to Inspiratory Burst Termination in preB?tzinger Complex
Neurons of Neonatal Mice Studied in Vitro. Front Neural Circuits 4:124.

Kuznetsov Y (1998) Elements of applied bifurcation theory, 2nd ed. New York: Springer.

Kuznetsov Y, Sacker R (2008) Neimark-Sacker bifurcation. Scholarpedia 3:1845.

Lavrentovich M, Hemkin S (2008) A mathematical model of spontaneous calcium(II) oscillations in astrocytes. J Theor Biol 251:553–560.

Lieske SP, Ramirez J-M (2006) Pattern-specific synaptic mechanisms in a multifunctional network. I. Effects of alterations in synapse strength. J Neurophysiol 95:1323–1333.

Lieske SP, Thoby-Brisson M, Telgkamp P, Ramirez JM (2000) Reconfiguration of the neural network controlling multiple breathing patterns: eupnea, sighs and gasps [see comment]. Nat Neurosci 3:600–607.

Li P, Janczewski WA, Yackle K, Kam K, Pagliardini S, Krasnow MA, Feldman JL (2016) The peptidergic control circuit for sighing. Nature 530:293–297.

Li Y-X, Rinzel J (1994) Equations for InsP3 Receptor-mediated [Ca2+]i Oscillations Derived from a Detailed Kinetic Model: A Hodgkin-Huxley Like Formalism. J Theor Biol 166:461–473.

Matkowsky BJ, Reiss EL (1977) Singular Perturbations of Bifurcations. SIAM J Appl Math 33:230–255.

McKay LC, Janczewski WA, Feldman JL (2005) Sleep-disordered breathing after targeted ablation of preBötzinger complex neurons. Nat Neurosci 8:1142.

Mironov SL (2008) Metabotropic glutamate receptors activate dendritic calcium waves and TRPM channels which drive rhythmic respiratory patterns in mice. J Physiol 586:2277–2291.

Mironov SL (2013) Calmodulin and calmodulin kinase II mediate emergent bursting activity in the brainstem respiratory network (preBötzinger complex). J Physiol 591:1613–1630.

Mironov SL, Skorova EY (2011) Stimulation of bursting in pre-Bötzinger neurons by Epac through calcium release and modulation of TRPM4 and K-ATP channels. J Neurochem 117:295–308.

Moore JD, Deschênes M, Furuta T, Huber D, Smear MC, Demers M, Kleinfeld D (2013) Hierarchy of orofacial rhythms revealed through whisking and breathing. Nature 497:205–210.

Newman MEJ (2005) A measure of betweenness centrality based on random walks. Soc Netw 27:39–54.

Newman MEJ (2010) Networks: an introduction. Oxford ; New York: Oxford University Press.

Newman MEJ, Strogatz SH, Watts DJ (2001) Random graphs with arbitrary degree distributions and their applications. Phys Rev E 64:026118.

O'Donovan MJ (1999) The origin of spontaneous activity in developing networks of the vertebrate nervous system. Curr Opin Neurobiol 9:94–104.

Ono T, Ishiwata Y, Inaba N, Kuroda T, Nakamura Y (1994) Hypoglossal premotor neurons with rhythmical inspiratory-related activity in the cat: localization and projection to the phrenic nucleus. Exp Brain Res 98:1–12.

Orem J, Trotter RH (1993) Medullary respiratory neuronal activity during augmented breaths in intact unanesthetized cats. J Appl Physiol Bethesda Md 1985 74:761–769.

Pace RW, Del Negro CA (2008) AMPA and metabotropic glutamate receptors cooperatively generate inspiratory-like depolarization in mouse respiratory neurons in vitro. Eur J Neurosci 28:2434–2442.

Pace RW, Mackay DD, Feldman JL, Del Negro CA (2007a) Inspiratory bursts in the preBötzinger complex depend on a calcium-activated non-specific cation current linked to glutamate receptors in neonatal mice. J Physiol 582:113–125.

Pace RW, Mackay DD, Feldman JL, Del Negro CA (2007b) Role of persistent sodium current in mouse preBötzinger Complex neurons and respiratory rhythm generation: Role of I_{NaP} in active preBötzinger Complex neurons. J Physiol 580:485–496.

Peever JH, Shen L, Duffin J (2002) Respiratory pre-motor control of hypoglossal motoneurons in the rat. Neuroscience 110:711–722.

Peña F, Parkis MA, Tryba AK, Ramirez J-M (2004) Differential contribution of pacemaker properties to the generation of respiratory rhythms during normoxia and hypoxia. Neuron 43:105–117.

Picardo MCD, Weragalaarachchi KTH, Akins VT, Del Negro CA (2013) Physiological and morphological properties of Dbx1-derived respiratory neurons in the pre-Botzinger complex of neonatal mice. J Physiol 591:2687–2703.

Ptak K, Zummo GG, Alheid GF, Tkatch T, Surmeier DJ, McCrimmon DR (2005) Sodium currents in medullary neurons isolated from the pre-Bötzinger complex region. J Neurosci 25:5159–5170.

Purvis LK, Smith JC, Koizumi H, Butera RJ (2007) Intrinsic bursters increase the

robustness of rhythm generation in an excitatory network. J Neurophysiol 97:1515–1526.

Rekling JC, Champagnat J, Denavit-Saubié M (1996) Electroresponsive properties and membrane potential trajectories of three types of inspiratory neurons in the newborn mouse brain stem in vitro. J Neurophysiol 75:795–810.

Rekling JC, Feldman JL (1998) PreBötzinger complex and pacemaker neurons: hypothesized site and kernel for respiratory rhythm generation. Annu Rev Physiol 60:385–405.

Rekling JC, Shao XM, Feldman JL (2000) Electrical coupling and excitatory synaptic transmission between rhythmogenic respiratory neurons in the preBötzinger complex. J Neurosci 20:RC113.

Revill AL, Vann NC, Akins VT, Kottick A, Gray PA, Del Negro CA, Funk GD (2015) Dbx1 precursor cells are a source of inspiratory XII premotoneurons. eLife 4:e12301.

Rinzel J (1987) A Formal Classification of Bursting Mechanisms in Excitable Systems. In: Mathematical Topics in Population Biology, Morphogenesis and Neurosciences (Teramoto E, Yumaguti M, eds), pp 267–281. Berlin, Heidelberg: Springer Berlin Heidelberg.

Rinzel J, Ermentrout GB (1998) Analysis of neural excitability and oscillations. In: Methods in neuronal modeling, 2nd ed. (Koch C, Segev I, eds), pp 251–291. MIT Press.

Ruangkittisakul A, Kottick A, Picardo MCD, Ballanyi K, Del Negro CA (2014) Identification of the pre-Botzinger complex inspiratory center in calibrated "sandwich" slices from newborn mice with fluorescent Dbx1 interneurons. Physiol Rep 2:e12111.

Ruangkittisakul A, Schwarzacher SW, Secchia L, Ma Y, Bobocea N, Poon BY, Funk GD, Ballanyi K (2008) Generation of eupnea and sighs by a spatiochemically organized inspiratory network. J Neurosci Off J Soc Neurosci 28:2447–2458.

Rubin JE, Hayes JA, Mendenhall JL, Del Negro CA (2009) Calcium-activated nonspecific cation current and synaptic depression promote network-dependent burst oscillations. Proc Natl Acad Sci U S A 106:2939–2944.

Sabidussi G (1966) The centrality of a graph. Psychometrika 31:581–603.

Schatzmann HJ (1989) The Calcium Pump of the Surface Membrane and of the Sarcoplasmic Reticulum. Annu Rev Physiol 51:473–485.

Scheffer M, Bascompte J, Brock WA, Brovkin V, Carpenter SR, Dakos V, Held H, van Nes EH, Rietkerk M, Sugihara G (2009) Early-warning signals for critical transitions. Nature 461:53–59.

Schwab DJ, Bruinsma RF, Levine AJ (2010) Rhythmogenic neuronal networks, pacemakers, and k-cores. Phys Rev E 82:051911.

Smith JC, Ellenberger HH, Ballanyi K, Richter DW, Feldman JL (1991) Pre-Botzinger complex: a brainstem region that may generate respiratory rhythm in mammals. Science 254:726–729.

Smith JC, Greer JJ, Liu GS, Feldman JL (1990) Neural mechanisms generating respiratory pattern in mammalian brain stem-spinal cord in vitro. I. Spatiotemporal patterns of motor and medullary neuron activity. J Neurophysiol 64:1149–1169.

Song H, Hayes JA, Vann NC, Drew LaMar M, Del Negro CA (2015) Mechanisms Leading to Rhythm Cessation in the Respiratory PreBotzinger Complex Due to Piecewise Cumulative Neuronal Deletions. eNeuro 2 Available at: http://eneuro.sfn.org/cgi/doi/10.1523/ENEURO.0031-15.2015 [Accessed September 18, 2015].

Song H, Hayes JA, Vann NC, Wang X, LaMar MD, Del Negro CA (2016) Functional Interactions between Mammalian Respiratory Rhythmogenic and Premotor Circuitry. J Neurosci 36:7223–7233.

Stanek E, Cheng S, Takatoh J, Han B-X, Wang F (2014) Monosynaptic premotor circuit tracing reveals neural substrates for oro-motor coordination. eLife 3:e02511.

Strogatz SH (2001) Nonlinear dynamics and chaos: with applications to physics, biology, chemistry, and engineering, 2. print. Cambridge, Mass: Perseus Books.

Suzue T (1984) Respiratory rhythm generation in the in vitro brain stem-spinal cord preparation of the neonatal rat. J Physiol 354:173–183.

Taddese A, Bean BP (2002) Subthreshold Sodium Current from Rapidly Inactivating Sodium Channels Drives Spontaneous Firing of Tuberomammillary Neurons. Neuron 33:587–600.

Takeda M, Matsumoto S (1997) Discharge patterns of dorsal and ventral respiratory group neurons during spontaneous augmented breaths observed in pentobarbital anesthetized rats. Brain Res 749:95–100.

Thoby-Brisson M, Ramirez JM (2001) Identification of two types of inspiratory pacemaker neurons in the isolated respiratory neural network of mice. J Neurophysiol 86:104–112.

Thoby-Brisson M, Telgkamp P, Ramirez JM (2000) The role of the hyperpolarization-activated current in modulating rhythmic activity in the isolated respiratory network of mice. J Neurosci Off J Soc Neurosci 20:2994–3005.

Toporikova N, Butera RJ (2011) Two types of independent bursting mechanisms in inspiratory neurons: an integrative model. J Comput Neurosci 30:515–528.

Toporikova N, Chevalier M, Thoby-Brisson M (2015) Sigh and Eupnea Rhythmogenesis Involve Distinct Interconnected Subpopulations: A Combined Computational and Experimental Study. eNeuro 2 Available at: http://eneuro.sfn.org/cgi/doi/10.1523/ENEURO.0074-14.2015 [Accessed July 5, 2016].

Tryba AK, Peña F, Lieske SP, Viemari J-C, Thoby-Brisson M, Ramirez J-M (2008) Differential modulation of neural network and pacemaker activity underlying eupnea and sigh-breathing activities. J Neurophysiol 99:2114–2125.

Tu H, Wang Z, Bezprozvanny I (2005a) Modulation of Mammalian Inositol 1,4,5-Trisphosphate Receptor Isoforms by Calcium: A Role of Calcium Sensor Region. Biophys J 88:1056–1069.

Tu H, Wang Z, Nosyreva E, De Smedt H, Bezprozvanny I (2005b) Functional Characterization of Mammalian Inositol 1,4,5-Trisphosphate Receptor Isoforms. Biophys J 88:1046–1055.

Urbani A, Belluzzi O (2000) Riluzole inhibits the persistent sodium current in mammalian CNS neurons. Eur J Neurosci 12:3567–3574.

Volgin DV, Rukhadze I, Kubin L (2008) Hypoglossal premotor neurons of the intermediate medullary reticular region express cholinergic markers. J Appl Physiol Bethesda Md 1985 105:1576–1584.

Von Euler C (1983) On the central pattern generator for the basic breathing rhythmicity. J Appl Physiol 55:1647–1659.

Vo T, Bertram R, Tabak J, Wechselberger M (2010) Mixed mode oscillations as a mechanism for pseudo-plateau bursting. J Comput Neurosci 28:443–458.

Wallén-Mackenzie A, Gezelius H, Thoby-Brisson M, Nygård A, Enjin A, Fujiyama F, Fortin G, Kullander K (2006) Vesicular glutamate transporter 2 is required for central respiratory rhythm generation but not for locomotor central pattern generation. J Neurosci 26:12294–12307.

Wang X, Hayes JA, Picardo MCD, Del Negro CA (2013) Automated cell-specific laser detection and ablation of neural circuits in neonatal brain tissue. J

Physiol 591:2393–2401.

Wang X, Hayes JA, Revill AL, Song H, Kottick A, Vann NC, LaMar MD, Picardo MCD, Akins VT, Funk GD, Del Negro CA (2014) Laser ablation of Dbx1 neurons in the pre-Bötzinger Complex stops inspiratory rhythm and impairs output in neonatal mice. eLife 3:e03427.

Watts DJ, Strogatz SH (1998) Collective dynamics of "small-world" networks. Nature 393:440–442.

Woch G, Ogawa H, Davies RO, Kubin L (2000) Behavior of hypoglossal inspiratory premotor neurons during the carbachol-induced, REM sleep-like suppression of upper airway motoneurons. Exp Brain Res 130:508–520.

Yogev S, Shen K (2014) Cellular and Molecular Mechanisms of Synaptic Specificity. Annu Rev Cell Dev Biol 30:417–437.

VITA

Hanbing Song was born on January 29th, 1989 in Tianjin, China. He received a Bachelor of Science major in Mathematics (Chern's Class) at Nankai University. Then he began his graduate study at Florida State University major in Applied and Computational Mathematics and received a Master of Science in 2012. He began his Ph.D study in the department of applied science at William & Mary in the fall of 2012, where he worked as a research assistant in Dr. Christopher Del Negro's lab. His research focused on mathematical modeling of mammalian respiratory rhythmogenic circuitry on both cellular and network levels. After graduation, Hanbing will begin working as a postdoc at Franklin and Marshall College in Lancaster Pennsylvania starting January 2017.